

Award Number: DAMD17-03-1-0384

TITLE: Seamless Integration of Detection and Therapy for Breast Cancer using Targeted Engineered Nanoparticles

PRINCIPAL INVESTIGATOR: Naomi J. Halas, Ph.D.

CONTRACTING ORGANIZATION: William Marsh Rice University
Houston, TX 7251-1892

REPORT DATE: June 2007

TYPE OF REPORT: Annual

PREPARED FOR: U.S. Army Medical Research and Materiel Command
Fort Detrick, Maryland 21702-5012

DISTRIBUTION STATEMENT: Approved for Public Release;
Distribution Unlimited

The views, opinions and/or findings contained in this report are those of the author(s) and should not be construed as an official Department of the Army position, policy or decision unless so designated by other documentation.

REPORT DOCUMENTATION PAGE

Form Approved
OMB No. 0704-0188

Public reporting burden for this collection of information is estimated to average 1 hour per response, including the time for reviewing instructions, searching existing data sources, gathering and maintaining the data needed, and completing and reviewing this collection of information. Send comments regarding this burden estimate or any other aspect of this collection of information, including suggestions for reducing this burden to Department of Defense, Washington Headquarters Services, Directorate for Information Operations and Reports (0704-0188), 1215 Jefferson Davis Highway, Suite 1204, Arlington, VA 22202-4302. Respondents should be aware that notwithstanding any other provision of law, no person shall be subject to any penalty for failing to comply with a collection of information if it does not display a currently valid OMB control number. **PLEASE DO NOT RETURN YOUR FORM TO THE ABOVE ADDRESS.**

1. REPORT DATE (DD-MM-YYYY) 01-06-2007		2. REPORT TYPE Annual		3. DATES COVERED (From - To) 15 May 2006 – 14 May 2007	
4. TITLE AND SUBTITLE Seamless Integration of Detection and Therapy for Breast Cancer using Targeted Engineered Nanoparticles				5a. CONTRACT NUMBER	
				5b. GRANT NUMBER DAMD17-03-1-0384	
				5c. PROGRAM ELEMENT NUMBER	
6. AUTHOR(S) Naomi J. Halas, Ph.D. E-Mail: halas@rice.edu				5d. PROJECT NUMBER	
				5e. TASK NUMBER	
				5f. WORK UNIT NUMBER	
7. PERFORMING ORGANIZATION NAME(S) AND ADDRESS(ES) William Marsh Rice University Houston, TX 7251-1892				8. PERFORMING ORGANIZATION REPORT NUMBER	
9. SPONSORING / MONITORING AGENCY NAME(S) AND ADDRESS(ES) U.S. Army Medical Research and Materiel Command Fort Detrick, Maryland 21702-5012				11. SPONSOR/MONITOR'S REPORT NUMBER(S)	
				12. DISTRIBUTION / AVAILABILITY STATEMENT Approved for Public Release; Distribution Unlimited	
13. SUPPLEMENTARY NOTES – Original contains colored plates: ALL DTIC reproductions will be in black and white.					
14. ABSTRACT This report summarizes the efforts of our team consisting of researchers from Rice University and M. D. Anderson Cancer Center, in the DoD funded CDMRP award towards the development of an integrated nano particle based imaging and therapy of breast cancer. We have made significant progress in our goals to demonstrate enhanced contrast in Optical Coherence Tomography (OCT) imaging tumors and photo thermal ablation using a single multifunctional particle. We have optimized the nanoshell that has a resonance in the near IR physiological water window, and can be used for both optical diagnostic imaging and photo thermal therapy. We have also explored other optical techniques for diagnosing malignant tumors from normal tissue.					
15. SUBJECT TERMS Nanoshells, Cancer Therapy, Cancer Imaging, Nanoparticles					
16. SECURITY CLASSIFICATION OF:			17. LIMITATION OF ABSTRACT	18. NUMBER OF PAGES	19a. NAME OF RESPONSIBLE PERSON USAMRMC
a. REPORT U	b. ABSTRACT U	c. THIS PAGE U			19b. TELEPHONE NUMBER (include area code)

Table of Contents

Introduction.....	4
Body	4
Key Research Accomplishments	6
Reportable Outcomes.....	6
Conclusions.....	12
References.....	13
Appendices.....	13
Supporting Data	14

Introduction

Gold nanoshells are a new class of nanoparticles with a highly tunable surface plasmon resonance. They consist of a spherical silica core covered with a thin shell of gold. The surface plasmon resonance of these nanoshells can be changed by changing the size of the core silica particles and the thickness of the gold shell. The Halas nanoengineering group at Rice University was the first to develop these particles¹ and demonstrate their application to photothermal ablation of tumors.²⁻⁴ The current DoD funded CDMRP award is for the development of nanoparticle based methods for detection, imaging and therapy of breast cancer. This report summarizes the efforts of our team consisting of researchers from Rice University and M. D. Anderson Cancer Center, in the DoD funded CDMRP award towards the development of an integrated nano particle based imaging and therapy of breast cancer.

We have made significant progress in our goals to demonstrate enhanced optical contrast in imaging tumors and photo thermal ablation using a single multifunctional particle. We have optimized the nanoshell that has a resonance in the near IR physiological water window, can be used for both optical diagnostic imaging and photo thermal therapy.

Other optical methods to distinguish between malignant tumors and normal tissue, such as reflectance spectroscopy and fiber probe base scattering measurements have been explored. Nanoshells can be used to improve the contrast in these techniques. Experimental demonstration of the signal enhancement has been demonstrated in tissue phantoms and in cancerous tissue samples.

Body

PROJECT 1: Bioconjugation-based Targeting of Nanoparticles for imaging and therapy:

Task 1: Identification of optimal ligand-receptor pair for vascular targeted therapy in breast cancer (months 1-36).

Accomplishment: Demonstrated in previous reports.

Task 2: Development of bioconjugate chemistry for binding targeting peptides and antibodies to nanoshells and nanoemitters (months 12-48).

Accomplishment: In previous reports we have outlined the development of immunonanoshells, nanoshells targeted with anti HER2 antibodies.²

PROJECT 2: Nanoparticle-based Image Enhancement:

Task 1: Investigation of the effectiveness of gold nanoshells and rare earth nanoemitters as image enhancers in tomographic infrared imaging, (months 1-24).

Accomplishments: We have performed Monte-Carlo simulations of nanoshells embedded in tissue models. This allows us to optimize the size and concentration of nanoshells required for optical imaging. The results of the Monte-Carlo simulations have also been verified

experimentally using a fixed fiber probe to measure the reflectance from a nanoshell solution.³

Task 2: Evaluation of the improvements in image contrast and resolution due to nanoshell-based and nanoemitter-based contrast enhancers, (months 12-36).

We have demonstrated dramatic improvement of optical contrast in imaging cancerous tissue using Optical Coherence Tomography (OCT). The enhancement has been demonstrated *in vivo* in mouse tumor models.⁴

We have also demonstrated greater enhancement of nanoshell induced reflectance signals from angled fiber probes as compared to conventional orthogonal fiber geometry. These greatly enhanced signals have been measured in both tissue phantoms (suspensions of silica spheres) and in cancerous cervical tissue samples.⁵

Task 3: Demonstration of feasibility of targeted nanoshell-based imaging and nanoemitter-based imaging in a mouse tumor model, (months 12-48).

Accomplishments: We have successfully demonstrated the use of a single nanoshell to first increase the optical contrast for OCT imaging and subsequent photothermal ablation of the tumors in mouse tumor models.

Nanoshells with a 119 nm silica core and approximately 12 nm gold shell were synthesized. Mie scattering theory predicts 67% of the extinction of these shells is due to absorption and 33 % is due to scattering at 800 nm.

Next the shells were passivated with thiolated poly ethylene (PEG) molecules. This provides steric stability and solubility while the nanoshells circulate and accumulate in the tumors due to the leaky neovasculature of the tumors. Figure 1 demonstrates the accumulation of the nanoshells in tumors after circulating for 20 hours. The images were collected after excising the tumors.

OCT images were collected after 20 hours, *in vivo* by placing the probe on shaved skin over the tumor site. Figure 2 shows the enhanced OCT signal from the tumor tissue embedded with nanoshells. This is compared to normal tissue with nanoshells and a control tumor tissue with a phosphate buffer injected instead of the nanoshell solution.

Next the animals were randomly divided into control, sham and treatment groups. Tumor size and survival was monitored over 7 weeks. Figure 3 shows the tumor size and survival for the various groups (white: with nanoshells and NIR laser treatment, grey: with phosphate buffer and NIR laser treatment, and black with no treatment)⁴

PROJECT 3: Molecular Fingerprinting

Task 1: Examination of the feasibility of noninvasive “molecular fingerprinting” in a tissue culture model, (months 1-24).

Accomplishments: We have also demonstrated the use of biologically active networks of Au nanoparticle-phage as optically active labels for non invasive detection using surface enhanced Raman spectroscopy (SERS),^{6,7} in previous reports.

Task 2: Investigation of spectroscopic detection of early lesions, (months 12-48).

Accomplishments: We have developed a nanoshell based nano pH sensor.⁸ Work is ongoing for testing the sensitivity of cellular pH as a marker for tumor malignancy.

PROJECT 4: Nanoshell-based Photothermal Cancer Therapy

Task 1: Evaluation of the therapeutic effect of targeted nanoshells in animal models of breast cancer, (months 1-36).

Accomplishment: As described in project 2 (task 3), the therapeutic effect of nanoshells in mouse models has been demonstrated. Work is ongoing on using targeted immunonanoshells (nanoshells with anti- HER2 antibodies conjugated to the surface of nanoshell) for therapeutic effect in mouse models.

Task 2: Development of a strategy for combined imaging and therapy, (months 12-48).

Accomplishments: As described in project 2 (task 3), we have developed techniques for improving circulation of nanoshells by attaching PEG to nanoshell surfaces.

Nanoshell induced image contrast enhancement for OCT,⁴ reflectance spectroscopy,³ and angled fiber probe scattering measurements⁵ have been demonstrated theoretically, in tissue phantoms, and in mouse tumors.

Combined OCT imaging and photothermal ablation using the same nanoshell has been demonstrated.⁴

Work is in progress to combine targeted immunonanoshells with the OCT imaging and photothermal therapy.

Key Research Accomplishments

- Successful *in-vivo* (in mouse tumor) demonstration of a single nanoshell that enhances the scattering signal for OCT imaging and is subsequently used for photothermal ablation of the tumor.
- Monte Carlo simulations used to optimize the size and concentration of nanoshells needed to enhance reflectance and scattering based optical imaging of tumors.
- Optical signal optimized in fiber probe based optical spectroscopy. Experimentally demonstrated enhanced optical signals in tissue phantoms and cancerous cervical tissue.

Reportable Outcomes

Published

Papers

1. A. M. Gobin, M. H. Lee, N. J. Halas, W. D. James, R. A. Drezek, and J. L. West, "Near-Infrared Resonant Nanoshells for Combined Optical Imaging and Photothermal Cancer Therapy," *Nano Lett.* (2007).

2. V. Nammalvar, A. Wang, and R. Drezek, "Enhanced gold nanoshell scattering contrast using angled fiber probes," *J. Nanophoton* **1**, 013510 (2007).
3. A. W. H. Lin, N. A. Lewinski, M.-H. Lee, and R. A. Drezek, "Reflectance spectroscopy of gold nanoshells: computational predictions and experimental measurements," *Journal of Nanoparticle Research* (2006).
4. K. Fu, J. Sun, A. Lin, H. Wang, N. Halas, and D. R., " Polarized Angular Dependent Light Scattering Properties of Bare and PEGylated Gold Nanoshells.," *Current Nanoscience* **3**, 167-170 (2007).
5. P. Fortina, L. J. Kricka, D. J. Graves, J. Park, T. Hyslop, F. Tam, N. Halas, S. Surrey, and S. A. Waldman, "Applications of nanoparticles to diagnostics and therapeutics in colorectal cancer," *TRENDS in Biotechnology* **25**(4), 145-152 (2007).
6. A. Hajitou, R. Rangel, M. Trepel, S. Soghomonyan, J. G. Gelovani, M. M. Alauddin, R. Pasqualini, and W. Arap, "Design and construction of targeted AAVP vectors for mammalian cell transduction.," *Nat. Protoc.* **3**, 523-531 (2007).
7. R. Rangel, Y. Sun, L. Guzman-Rojas, M. G. Ozawa, J. Sun, R. J. Giordano, C. S. Van Pelt, P. T. Tinkey, R. R. Behringer, R. L. Sidman, W. Arap, and R. Pasqualini, "Impaired angiogenesis in aminopeptidase N-null mice," *Proc Natl Acad Sci U S A* **104**, 4588-4593 (2007).

In Press

1. Lahdenranta J, Sidman RL, Pasqualini R, Arap W. Treatment of hypoxia-induced retinopathy with targeted proapoptotic peptidomimetic in a mouse model of disease. *FASEB J* (In press).
2. Bover LC, Cardó-Vila M, Sun J, Aggarwal B, Arap W, Pasqualini R. A previously unrecognized protein-protein interaction between TWEAK and CD163: potential biological implications. *J Immunol* (In press).

Invited Articles

1. Hajitou A, Pasqualini R, Arap W. Vascular targeting: Recent advances and therapeutic perspectives. *Trends Cardiovasc Med* 16:80-8, 2006.
2. Sergeeva A, Kolonin MG, Molldrem JJ, Pasqualini R, Arap W. Display technologies: application for the discovery of drug and gene delivery agents. *Adv Drug Deliv Rev* 58:1622-54, 2006.

3. Christianson DR, Ozawa MG, Arap W, Pasqualini R. Techniques to decipher molecular diversity by phage display. *Methods Mol Biol* 357:385-406, 2006.
4. Sato M , Pasqualini R, Arap W. *Oncology* (In press).

Conference Proceedings

Presentations

1. Lowery A., Gobin A.M., Day E., Shah K., Halas N., Drezek R., West J. “Antibody-Conjugated Metal Nanoshells for Tumor Specific Photothermal Therapy” (oral) Society for Biomaterials, Pittsburgh, PA, April 2006
2. A.M. Gobin, M. Lee, N. Halas, R. Drezek1 & J. West. Nanoshells for Integrated Cancer Imaging and Therapy. *Poster*, American Association of Cancer Research: Molecular Diagnostics in Cancer Therapeutic Development, Chicago, IL, September 12-15, 2006
3. Fu, K., Halas, N., West J, and Drezek, R. “A Scatter-Based Method for Quantifying Nanoparticle Binding to Targeted Cells” SPIE Photonics West. Oral presentation (2007).
4. Fu, K., Halas, N., West J, and Drezek, R. “A Scatter-Based Method for Quantifying Nanoparticle Binding to Surface Markers” RQI Annual Symposium (2006).

Poster Presentations

5. Lowery A., Gobin A.M., Halas N., West J. “Immunonanoshell laser-assisted therapy targets and ablates tumor cells” (poster) San Antonio Breast Cancer Symposium, San Antonio, TX, Dec. 2006
6. Lowery A., Gobin A.M., Halas N., West J. “Selective Photothermal Tumor Ablation using Immunonanoshells” (poster) Biomedical Engineering Society 2006, Chicago, IL, Oct. 2006
7. Lowery A., Gobin A.M., Halas N., West J. “Vascular targeting of nanoshells for photothermal cancer therapy” (poster) American Association of Cancer Research: Molecular Diagnostics in Cancer Therapeutic Development, Chicago, IL, Sept. 2006

Related Invited Talks

HALAS

1. “Taking the (Nano) device approach: applications of nanotechnology in the diagnosis and treatment of cancer and other diseases,” Gordon Research Conference in Molecular Therapeutics of Cancer, Oxford, UK, July 2006.

2. "Plasmonic Nanostructures: artificial molecules enabling nanoscale spectroscopies and nanophotonics-based biomedical applications," Gordon Research Conference in Plasmonics – Optics at the Nanoscale, Keene, NH, July 2006.
3. "Plasmonic Nanostructures: artificial molecules enabling nanoscale spectroscopies and nanoparticle-based biomedical applications", Invited talk, European Union Research Raining Network HYTEC, Annual Meeting, Heraklion, Crete, July 2006.
4. "Plasmonic Nanostructures: Artificial Molecules," Plenary Talk, SPIE (Society for Photo-optical Instrumentation Engineers) Annual Meeting, San Diego, CA, August 2006.
5. "An all-optical SERS-based pH nanosensor," SPIE (Society for Photo-optical Instrumentation Engineers) Annual Meeting, San Diego, CA, August 2006.
6. "Plasmonic Nanostructures: artificial molecules enabling nanoscale spectroscopies and nanoparticle-based biomedical applications", Nano 2006 Conference, San Sebastian, Spain, September 2006.
7. "Plasmonic Nanoparticles: Molecular Orbitals writ large", Chemistry Department Colloquium, Case Western Reserve University, Cleveland, OH, September 2006.
8. "Plasmonic Nanostructures: molecular orbitals writ large" and "Nanoengineered Plasmonic substrates for surface enhanced spectroscopies", Annual Nanowire Symposium, Division of Solid State Physics and the Nanometer Consortium, Lund University, Sweden, October 2006.
9. "When plasmons interact, worlds collide", Kirkpatrick Lecture, Illinois Institute of Technology, Chicago, IL, September 2006.
10. "Plasmon Hybridization: molecular orbitals writ large", Physical Chemistry Seminar, U. C. Berkeley, October 2006.
11. "A Nanoscale all-optical pH meter", IEEE-LEOS Annual Meeting, Montreal, Canada, November 2006.
12. "Plasmonics", Ecole Polytechnique de Montreal, Montreal, CA, November 2006.
13. "Taming surface enhanced spectroscopies with tailored plasmonic nanoparticle substrates", Chemistry Research Seminar, University of California, Santa Barbara October 2006.
14. "Plasmonic Nanoparticles: Molecular Orbitals writ large" ECE Departmental Seminar, Georgia Tech, Atlanta GA, November 2006.
15. "Plasmonic Nanoparticles: Molecular Orbitals writ large" Invited talk, Chemistry Department, Georgia Tech, Atlanta, GA, November 2006.

16. Invited talk, MRS Annual Meeting, November 2006.
17. “Plasmonic Nanostructures: Molecular Orbitals writ large” Invited talk, Nanoscience Speaker Series, University of Pittsburgh, December 2006.
18. “Plasmonics: Optics at the Nanoscale”, Invited talk, Argonne National Laboratory, December 2006.
19. “Plasmonic Design” Invited talk, Physics of Quantum Electronics Conference, Snowbird, UT, January 2007.
20. “Nanophotonics: the next Big Thing”, Invited talk, CINT Annual Workshop, Los Alamos National Laboratory/Sandia National Laboratory.
21. “Plasmonic Nanoparticles: Molecular Orbitals writ large” Annual Invited Lecturer, Institute for Materials Research, University of Connecticut, February 2007.
22. “Designing optical Nanotools for Biomedicine” Keynote Speaker, Peachey Conference, Purdue, University, Lafayette, IN, February 2007.
23. “Plasmonic Nanoparticles: Molecular Orbitals writ large” Invited talk, University of Utah, February 2007.
24. “Plasmonic coupling and nanophotonics” Invited speaker, ICAM Workshop, Santa Fe, NM March 2007.
25. “Designing optical Nanotools for Biomedicine” Plenary Speaker, IOP Annual Meeting in Nanoscale Physics and Technology, Southampton, UK, March 2007.
26. “Nanophotonics: from Plasmon Physics to Cancer Therapy” Invited talk, TAMEST meeting, Austin, TX, April 2007.
27. “Plasmonic Nanoparticles: Molecular Orbitals writ large” Invited talk, Physics Department, University of Pittsburgh, April 2007.
28. “Plasmonic Nanomaterials: Enabling Solutions in Pursuit of Challenges” Invited talk, Fundamentals of Nanoscience Conference, Snowbird, UT, April 2007.
29. “An Enabling Technology for Nanoscience and Defense Applications” Invited talk, “Nanotechnology for Defense Applications”, San Diego, April 2007.
30. “Plasmonic Nanoparticles: Molecular Orbitals writ large” Invited talk, University of California Davis, Applied Physics Department, April 2007.

31. "Plasmon-based Nanoparticle Probes for Multifunctional Diagnostics and Therapeutics"
Invited talk, Spring MRS meeting, San Francisco, CA, April 2007.
32. Invited talk, Spring MRS meeting, San Francisco, CA, April 2007.
33. "Using Nanotechnology to Harvest Light for Nanomedicine" WINS Lecturer, University
of Western Ontario, May 2007 (popular lecture).

PASQUALINI

34. Nanotechnology in Cancer Imaging. MRS Annual Meeting. Materials/Biology
Interface. Boston, MA. November 2007.
35. Nanotechnology-Enabled Optical Molecular Imaging of Cancer. Rice University
Workshop on Translational Optical Imaging. May 2007.
36. Nanotechnology for Point of Care Diagnostics. World Health Symposium. April 2007.
37. Optical Imaging for Minimally Invasive Medical Diagnosis. MD Anderson Cancer
Center Pediatrics Grand Rounds. April 2007.
38. Nanotechnology in Medical Imaging. MD Anderson Cancer Phase I Clinical Trial
Lecture Series. February 2007.
39. Towards Point-of-Care Optical Technologies for Early Cancer Detection. Department of
Electrical and Computer Engineering Corporate Affiliates Meeting. Rice University.
September 2006.
40. Activatable Nanoparticles for Cancer Imaging. Gordon Research Conference on Lasers
in Medicine and Surgery. July 2006.
41. Nanotechnology and Cancer. American Association for Cancer Research Annual
Meeting. Washington, DC. April 2006.
42. Optical Molecular Cancer Imaging. IEEE International Symposium on Biomedical
Imaging: Nano to Macro. Washington, DC. April 2006.
43. Speaker, 4th Annual Angiogenesis & Vascular Targeting Agents Drug Discovery &
Development World Summit, Boston, MA, 09/06
44. Speaker, Diagnosis and Therapeutic Discovery in Neuro-Oncology Conference, Houston,
TX, 10/06

45. Speaker, Clontech, Mountain View, CA, 10/06
46. Speaker, A.C. Camargo/Sister Institution, Extramural Program, Sao Paulo, Brazil, 10/06
47. Speaker, Biogen, Boston, MA, 11/06
48. Speaker, 18th EORTC-NCI-AACR Symposium, Prague, Czech Republic, 11/06
49. Speaker, 6th Edition of Amazon Project Conference on Cancer, Palermo, Italy, 11/06
50. Speaker, San Raffaele Hospital, Milan, Italy, 11/06
51. Speaker, Arap/Pasqualini Program Retreat, San Francisco, CA, 12/06
52. Speaker, University of Texas M. D. Anderson Cancer Center, Grand Rounds, Houston, TX, 01/07
53. Speaker, Nano Medicine Annual Symposium, Helsinki, Finland, 01/07
54. Speaker, International Symposium on Polymer Therapeutics (ISPT 07), Berlin, Germany, 02/07
55. Speaker, 2007 Advances in Oncology: Emerging Trends, Targets, and Approaches to Solid Tumors Symposium, Houston, TX, 3/07
56. Speaker, Memorial-Sloan Kettering Cancer Center, Molecular Pharmacology & Chemistry Seminar, New York, NY, 3/07
57. Speaker, Massachusetts General Hospital, Boston, MA, 04/07
58. Speaker, Stanford University, Palo Alto, CA, 4/07
59. Speaker, McGill Cancer Centre, Montreal, Canada, 4/07

Conclusions

This year the team from Rice University and M D Anderson has successfully demonstrated, and reached out beyond the key technologies outlined in our original proposal. We have optimized nanoshell sizes so that we can synthesize a single multifunctional nanoshell to combine optical diagnostic imaging with subsequent photothermal ablation of the tumor. We have demonstrated the above paradigm in vivo in a mouse tumor model. Mice receiving the nanoshell + near IR laser treatment showed a long term survival rate of 83 %.

Work is currently ongoing to develop other spectroscopic signatures of malignant tumors based on the surface enhanced Raman scattering from pH sensitive molecules conjugated to nanoshells.

References

1. S. J. Oldenburg, R. D. Averitt, and S. L. Westcott, "Nanoengineering of optical resonances," *Chem. Phys. Lett.* **288**, 243 (1998).
2. A. R. Lowery, A. M. Gobin, E. S. Day, N. J. Halas, and J. L. West, "Immunonanoshells for targeted photothermal ablation of tumor cells," *International Journal of Nanomedicine* **1**(2)(2006).
3. A. W. H. Lin, N. A. Lewinski, M.-H. Lee, and R. A. Drezek, "Reflectance spectroscopy of gold nanoshells: computational predictions and experimental measurements," *Journal of Nanoparticle Research* (2006).
4. A. M. Gobin, M. H. Lee, N. J. Halas, W. D. James, R. A. Drezek, and J. L. West, "Near-Infrared Resonant Nanoshells for Combined Optical Imaging and Photothermal Cancer Therapy," *Nano Lett.* (2007).
5. V. Nammalvar, A. Wang, and R. Drezek, "Enhanced gold nanoshell scattering contrast using angled fiber probes," *J. Nanophoton* **1**, 013510 (2007).
6. G. R. Souza, D. R. Christianson, F. I. Staquicini, M. G. Ozawa, E. Y. Snyder, R. L. Sidman, J. H. Miller, W. Arap, and R. Pasqualini, "Networks of gold nanoparticles and bacteriophage as biological sensors and cell-targeting agents," *Proc. Natl. Acad. Soc.* **103**(5), 1215–1220 (2006).
7. G. R. Souza, C. S. Levin, A. Hajitou, R. Pasqualini, W. Arap, and J. H. Miller, "In Vivo Detection of Gold-Imidazole Self-Assembly Complexes: NIR-SERS Signal Reporters," *Anal. Chem.* (2006).
8. S. W. Bishnoi, C. J. Rozell, C. S. Levin, M. K. Gheith, B. R. Johnson, D. H. Johnson, and N. J. Halas, "An all-optical nanoscale pH meter," *Nano Lett.* **6**(8), 1687-1692 (2006).

Appendices

1. A. M. Gobin, M. H. Lee, N. J. Halas, W. D. James, R. A. Drezek, and J. L. West, "Near-Infrared Resonant Nanoshells for Combined Optical Imaging and Photothermal Cancer Therapy," *Nano Lett.* (2007).
2. V. Nammalvar, A. Wang, and R. Drezek, "Enhanced gold nanoshell scattering contrast using angled fiber probes," *J. Nanophoton* **1**, 013510 (2007).
3. A. W. H. Lin, N. A. Lewinski, M.-H. Lee, and R. A. Drezek, "Reflectance spectroscopy of gold nanoshells: computational predictions and experimental measurements," *Journal of Nanoparticle Research* (2006).

4. P. Fortina, L. J. Kricka, D. J. Graves, J. Park, T. Hyslop, F. Tam, N. Halas, S. Surrey, and S. A. Waldman, "Applications of nanoparticles to diagnostics and therapeutics in colorectal cancer," *TRENDS in Biotechnology* **25**(4), 145-152 (2007).
5. A. Hajitou, R. Rangel, M. Trepel, S. Soghomonyan, J. G. Gelovani, M. M. Alauddin, R. Pasqualini, and W. Arap, "Design and construction of targeted AAVP vectors for mammalian cell transduction.," *Nat. Protoc.* **3**, 523-531 (2007).
6. R. Rangel, Y. Sun, L. Guzman-Rojas, M. G. Ozawa, J. Sun, R. J. Giordano, C. S. Van Pelt, P. T. Tinkey, R. R. Behringer, R. L. Sidman, W. Arap, and R. Pasqualini, "Impaired angiogenesis in aminopeptidase N-null mice," *Proc Natl Acad Sci U S A* **104**, 4588-4593 (2007).

Supporting Data

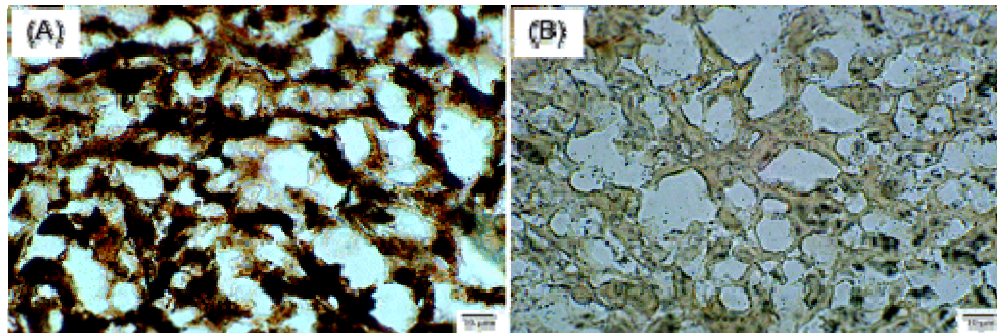


Figure 1: Silver enhancement staining of tissue shows heterogeneous staining of the tumor tissue from mice injected with nanoshells (A) indicating the presence of nanoshells. In contrast, there is little silver enhancement of sections taken from mice with PBS injection (B).

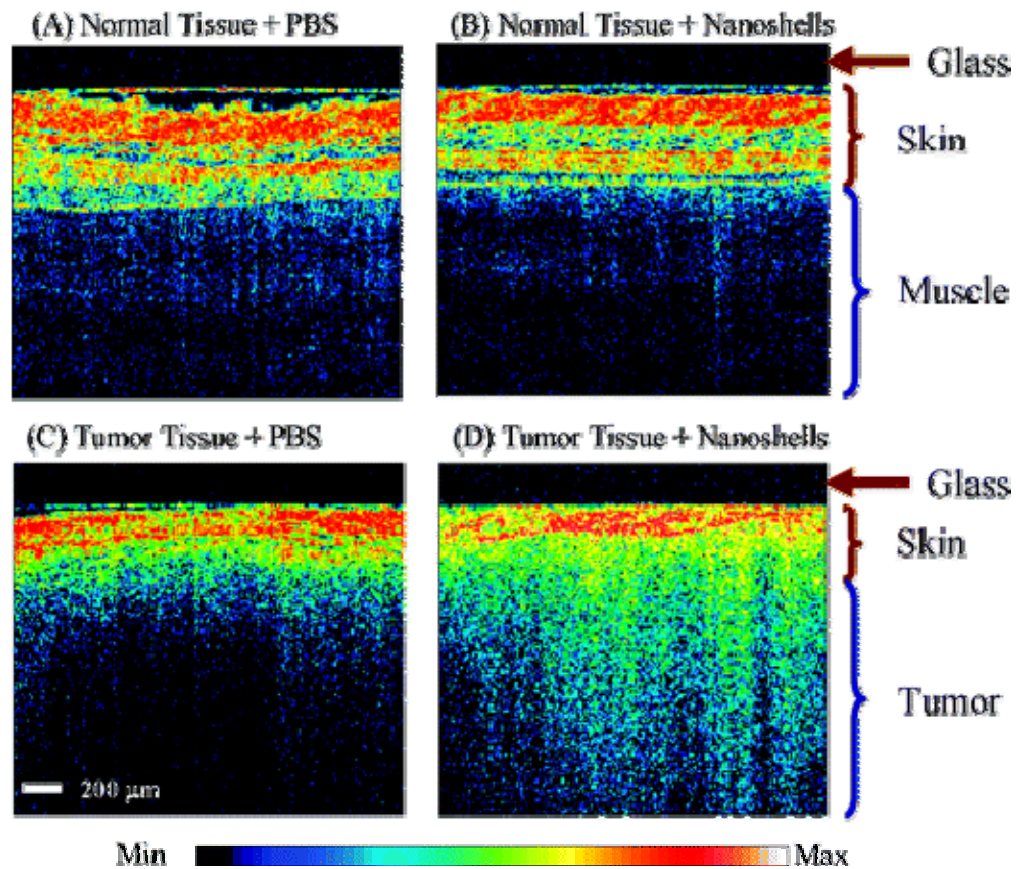


Figure 2: Representative OCT images from normal skin and muscle tissue areas of mice systemically injected with nanoshells (A) or with PBS (B). Representative OCT images from tumors of mice systemically injected with nanoshells (C) or with PBS (D). Analysis of all images shows a significant increase in contrast intensity after nanoshell injection in the tumors of mice treated with nanoshells while no increase in intensity is observed in the normal tissue. The glass of the probe is 200 μm thick and shows as a dark nonscattering layer.

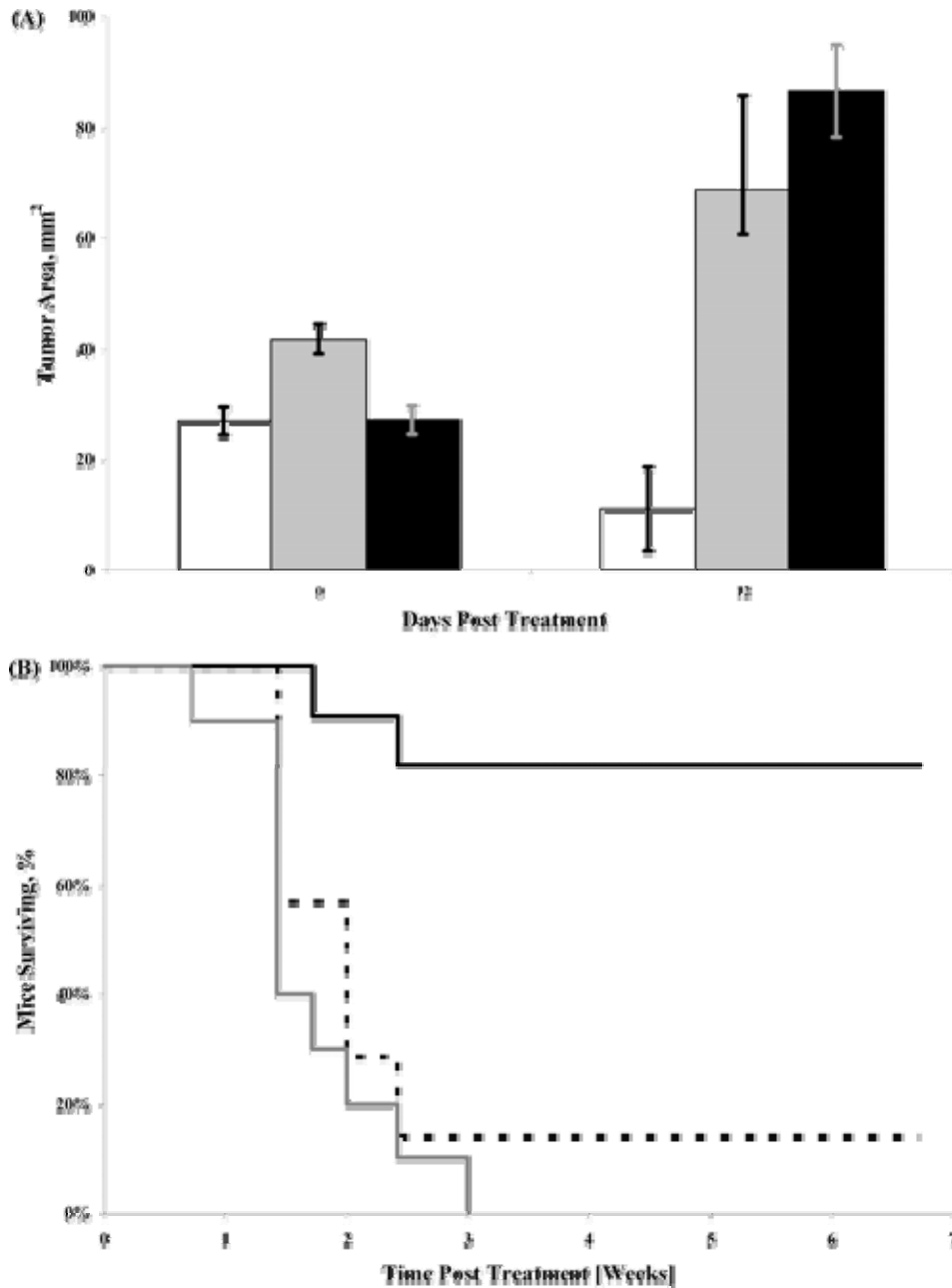


Figure 3: (A) Tumor size before irradiation and 12 days post-irradiation of mice treated with nanoshell + NIR laser irradiation (white bar); PBS sham + NIR laser treatment (gray bar) or untreated control (black bar); values are average \pm SEM. (B) Kaplan-Meier survival data for the treatment groups post irradiation; nanoshell + NIR laser irradiation (solid black line); PBS sham + NIR laser treatment (dashed black line) or untreated control (gray line); survival was followed for 7 weeks posttreatment. After 21 days, the nanoshell therapy group survival rate was significantly higher than either control group, $p < 0.001$.

Near-Infrared Resonant Nanoshells for Combined Optical Imaging and Photothermal Cancer Therapy

André M. Gobin,[†] Min Ho Lee,[†] Naomi J. Halas,[‡] William D James,[§] Rebekah A. Drezek,[†] and Jennifer L. West^{*†}

Department of Bioengineering, Rice University, Houston, Texas Zip ?????, Department of Electrical and Computer Engineering, Rice University, Houston, Texas Zip ?????, Center for Chemical Characterization and Analysis, Texas A&M University, City ???, State ??? Zip ?????

Received March 14, 2007; Revised Manuscript Received May 21, 2007

ABSTRACT

Metal nanoshells are core/shell nanoparticles that can be designed to either strongly absorb or scatter within the near-infrared (NIR) wavelength region (~650–950 nm). Nanoshells were designed that possess both absorption and scattering properties in the NIR to provide optical contrast for improved diagnostic imaging and, at higher light intensity, rapid heating for photothermal therapy. Using these in a mouse model, we have demonstrated dramatic contrast enhancement for optical coherence tomography (OCT) and effective photothermal ablation of tumors.

Much of the promise for nanotechnology in medicine has focused on the development of multifunctional agents for integrated diagnosis and therapy.^{1,2} Here we report on a successful in vivo demonstration of the use of near-infrared resonant nanoparticles, gold nanoshells, to first increase optical contrast in tumors for optical coherence tomography (OCT) imaging and second, to subsequently treat the tumors using nanoshell absorption of near-infrared (NIR) light for photothermal ablation using a single-nanoparticle formulation that has been designed to have both absorption and scattering in the NIR.

Nanoshells consist of a dielectric core nanoparticle surrounded by an ultrathin metal shell with tunable plasmon resonances. Nanoshells offer the ability to manipulate both the resonant wavelength and the relative scattering and absorption efficiencies through the size and composition of each layer of the nanoshell structure.^{3–5} Given these advantages, nanoshells can be used as contrast agents for enhanced OCT imaging,^{6,7} based on their backscattering properties, as well as cancer therapeutics,^{8,9} due to their absorbing properties. Through appropriate nanoparticle design for both strong absorption and scattering, both imaging and therapy should be improved with a single-particle formulation. For these studies, nanoshells were designed for absorption and scat-

tering in the near-infrared (NIR) region.^{4,10} This region is of significant biological importance, as it provides a region in the spectrum useful for both therapeutic and imaging applications in tissue because the components of tissue do not have significant absorption in this range of wavelengths.¹¹ Nanoshells are currently being investigated for use in the NIR region for a variety of applications, including diagnostic assays,¹² modulated drug delivery systems,¹³ and for laser tissue welding.¹⁴ We have previously demonstrated photothermal ablation and complete regression of tumors in mice, accomplished through intravenous injection and subsequent passive tumor accumulation, which was followed by external NIR treatment for several minutes.^{8,9} We recently reported the development of gold nanoshells suitable for therapy and imaging of cancer cells in in vitro studies.^{6,15} This early work imaged human breast cancer cells that had been treated with antibody-conjugated gold nanoshells under darkfield microscopy, followed by NIR laser, inducing cell ablation only within the laser spot. In the present study, we report on the use of nanoshells as contrast agents to enhance OCT imaging of tumors grown in vivo followed by therapeutic application of NIR light.

OCT is an imaging modality that provides cross-sectional subsurface imaging of biological tissue with micrometer-scale resolution. The principles of OCT have been described previously.^{16,17} OCT uses a short coherence length light source in a Michelson interferometer to enable high-resolution optical sectioning in tissue. In the system used in this study, low coherence light emitted from the source is

* Corresponding author. E-mail: jwest@rice.edu. Telephone: (713) 348-5955. Fax: (713) 348-5877. Rice University, MS 142, Department of Bioengineering, 6100 S. Main St., Houston, TX 77251.

[†] Department of Bioengineering, Rice University.

[‡] Department of Electrical and Computer Engineering, Rice University.

[§] Center for Chemical Characterization and Analysis, Texas A&M University.

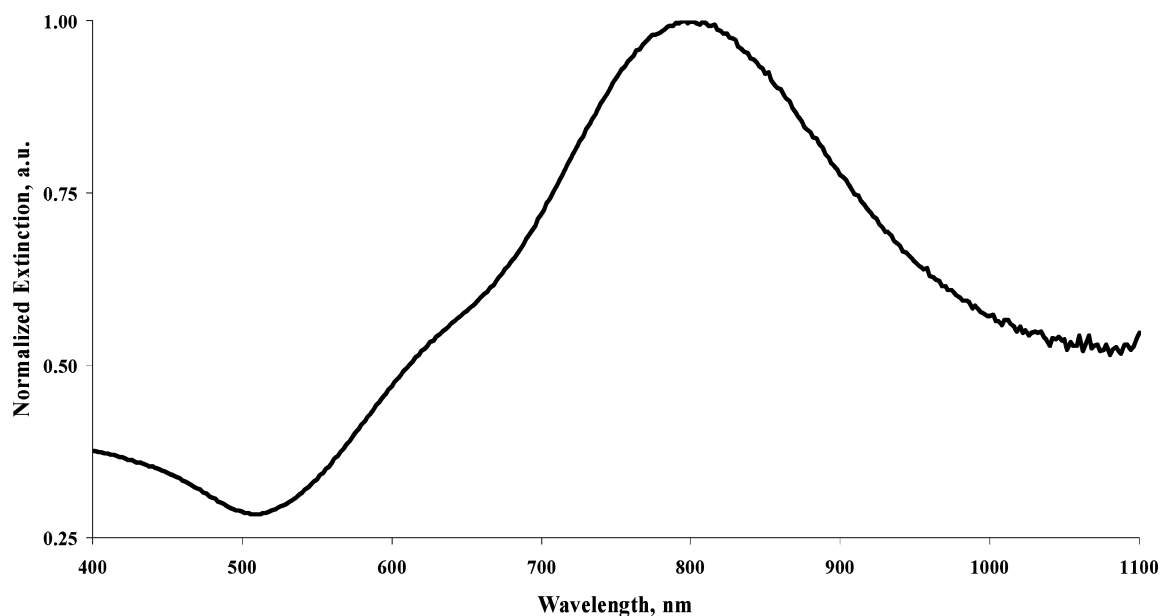


Figure 1. Extinction spectra of nanoshells used in this study. Nanoshells are 143 nm in diameter with a core of 119 nm and a shell thickness of 12 nm.

70 directed onto a beam splitter. One beam is sent toward a
71 reference mirror of known path length distance while the
72 other is directed toward the sample. The reflected waves from
73 both the reference mirror and sample are recombined at the
74 beam splitter and directed to a detector where interference
75 patterns are monitored as the reference mirror is moved. By
76 monitoring these patterns while scanning the reference
77 mirror, it is possible to map depth-resolved reflectivity of
78 the tissue. The diagnostic potential of OCT was demonstrated
79 by Matheny et al.¹⁸ and has been used for imaging cancers
80 of the gastrointestinal system,^{19–22} prostate,²³ and oral
81 mucosal²⁴ among others.

82 The use of contrast agents in OCT offers the promise of
83 enhanced diagnostic power, similar to results with contrast
84 agents in computed tomography (CT) and magnetic reso-
85 nance imaging (MRI). To increase contrast in OCT, imaging
86 agents including microbubbles²⁵ and microspheres with gold
87 nanoparticles have been employed.^{26,27} Optimal contrast
88 agents for OCT would both further enhance contrast in vivo
89 over the ~5% improvement obtained with microbubbles and
90 offer a smaller alternative to engineered microspheres (~2–
91 15 μm) to improve distribution into the microcirculation.
92 Because of their biocompatibility, tunable optical properties,
93 and small scale size, nanoshells are well suited to OCT,
94 providing easily detected backscattering of NIR light.
95 Furthermore, nanoshells have been shown to accumulate in
96 tumors due to the leakiness of tumor vasculature, allowing
97 efficient delivery of quantities suitable for both imaging and
98 therapy. For this reason, the current work combines the use
99 of OCT imaging with NIR treatment using an NIR absorbing
100 and scattering nanoshell in a murine in vivo model.

101 **Design of Dual Function Nanoshells.** Nanoshells were
102 made with cores that were 119 ± 11 nm in diameter. The
103 shell thickness was approximately 12 nm. The measured
104 extinction spectra of the nanoshells used in this study are
105 shown in Figure 1. Mie theory scattering calculations predict

that these particles have approximately 67% of the extinction 106
due to absorption and 33% due to scattering at 800 nm. 107

Nanoshells were prepared as previously described.^{4,5} 108
Briefly, silica cores were grown using the Stöber process, 109
the basic reduction of tetraethyl orthosilicate (Sigma-Aldrich, 110
Milwaukee, WI) in ethanol. The resultant silica nanoparticles 111
were examined under scanning electron microscopy (SEM; 112
Philips FEI XL30), and particles with a polydispersity of 113
less than 10% were used in subsequent steps. Reaction of 114
the silica core nanoparticles with (3-aminopropyl) triethoxy- 115
silane (APTES, Sigma-Aldrich) provided amine groups on 116
the surface of the core to allow for adsorption of gold colloid. 117
Gold colloid was prepared to a size of 2–4 nm in the method 118
of Duff et al. and aged 2–3 weeks at 4 °C.²⁸ The colloid 119
was then concentrated 20 \times through rotary evaporation and 120
mixed with the aminated silica particles, allowing small gold 121
colloid, attached to the larger silica nanoparticle surface, to 122
act as nucleation sites in the subsequent reduction step. This 123
final step, growing the gold shell, was accomplished by the 124
reduction of gold from chloroauric acid (HAuCl_4) in the 125
presence of formaldehyde. By this method, the reduction of 126
gold around the initial colloid sites allows gold islands to 127
develop and eventually coalesce to form a contiguous gold 128
shell. The extinction characteristics of the nanoshells were 129
determined using a UV–vis spectrophotometer (Carey 50 130
Varian, Walnut Creek, CA). Nanoshells were surface-coated 131
with poly(ethylene glycol) PEG to enhance circulation times 132
and reduce immune response. Pegylation was accomplished 133
by adding 20 μL of 5 μM PEG-SH, molecular weight 5 kDa 134
(Nektar, Huntsville, AL) to 1.5×10^{10} nanoshells/mL in DI 135
water for a minimum of 8 h. PEG-modified nanoshells were 136
sterilized by filtration using a 0.22 μm filter and subsequently 137
concentrated by centrifugation and re-diluted with sterile 138
phosphate buffered saline (PBS). 139

Nanoshells Provide Significant Increase in OCT Con- 140
trast. PEG-modified nanoshells were injected intravenously 141

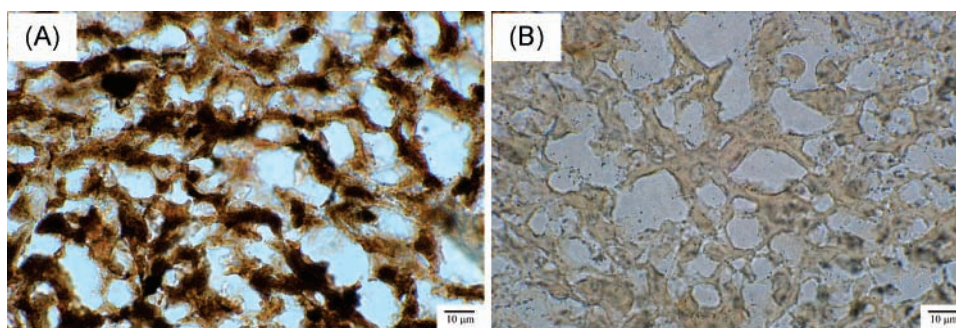


Figure 2. Silver enhancement staining of tissue shows heterogeneous staining of the tumor tissue from mice injected with nanoshells (A) indicating the presence of nanoshells. In contrast, there is little silver enhancement of sections taken from mice with PBS injection (B).

142 in tumor-bearing mice and allowed to passively accumulate
 143 in the tumor tissue due to the leakiness of the tumor
 144 vasculature. The significant accumulation of particles within
 145 the tumor tissue dramatically increased the NIR scattering
 146 within the tumor, enhancing the OCT contrast.

147 To grow tumors in mice, colon carcinoma cells were
 148 cultured and then injected subcutaneously in mice. Murine
 149 colon carcinoma cells (CT-26, ATCC, Manassas, VA) were
 150 grown at 37 °C in a 5% CO₂ environment in RPMI media
 151 supplemented with 4 mM l-glutamine, 1% penicillin, 1%
 152 streptomycin, and 10% fetal bovine serum (FBS). Cells were
 153 detached from culture with trypsin (0.05%) and EDTA
 154 (0.02%). Cells were re-suspended in sterile PBS for inoculation
 155 into BALBc mice (Charles River, Willington, MA).
 156 BALBc mice were used under an approved protocol of the
 157 Institutional Animal Care and Use Committee at Rice
 158 University. 150 000 CT-26 cells suspended in 25 µL of PBS
 159 were inoculated subcutaneously in the right flank of mice.
 160 Tumors were allowed to grow to a diameter of approximately
 161 5 mm (~10 days). At that point, 150 µL of PEG-modified
 162 nanoshells in PBS (1.5×10^{11} nanoshells/mL) were injected
 163 into the tail vein 20 h prior to imaging via OCT. Control
 164 animals received a PBS injection.

165 In one set of mice, tumors were excised at 20 h, and
 166 nanoshell levels in tumor and normal tissues were assessed.
 167 Two methods were used for this. First, excised tumors were
 168 cryosectioned and silver stained (Sigma Silver Enhancement
 169 system, Sigma, Milwaukee, WI); silver staining allows the
 170 nanoshells to act as nucleation sites for deposition of silver
 171 to grow large enough to allow for visualization under light
 172 microscopy. Other tissue samples were lyophilized for gold
 173 content determination using neutron activation analysis
 174 (NAA).²⁹ The blank and the tumor sample were irradiated
 175 along with precise calibration standards at the Texas A&M
 176 University's Nuclear Science Center 1 MW TRIGA research
 177 reactor for 14 h. The irradiation position used in this study
 178 has an average neutron flux of approximately $1 \times 10^{13} \text{ s}^{-1}$
 179 cm^{-2} . High-purity germanium detectors with nominal resolu-
 180 tions (fwhm) of 1.74 keV or better and efficiencies of 25–
 181 47% by industry standard relative measurement were used
 182 to quantify the 412 keV gamma line from ¹⁹⁸Au. The
 183 Canberra Industries OpenVMS alpha processor-based Genie-
 184 ESP software was used for acquisition and computation of
 185 gold concentrations.

186 Histological examination of tumors using silver staining
 187 confirmed the presence of nanoshells throughout the tumors.
 188 Figure 2 shows the silver staining of representative areas of
 189 tumors from mice treated with nanoshells (A) or with PBS
 190 (B). Additionally, NAA verified nanoshells present in the
 191 tumor shown in Figure 2A at 12.5 ppm, which is equivalent
 192 to approximately 3 million nanoshells per gram of tumor
 193 tissue, compared to 0 ppm for tumors of mice injected with
 194 just PBS 2B.

195 OCT images were collected for nanoshell-injected and
 196 control mice 20 h following injection (to allow time for
 197 passive accumulation of nanoshells) and analyzed to assess
 198 the increase in contrast provided by the nanoshells in tumor
 199 tissue compared to normal tissue. This study used a com-
 200 mercially available OCT imaging system (Niris Imaging
 201 System, Imalux, Cleveland, OH). The axial and transverse
 202 resolutions were measured to be approximately 10 and 15
 203 µm, respectively. OCT images of the tumor and normal tissue
 204 was taken after 20 h of circulation. The animals were not
 205 anesthetized during the injection or circulation period, only
 206 during imaging and treatment. The tumors were imaged using
 207 the Niris OCT imaging device by applying glycerol on the
 208 shaved tumor site for index matching and placing the probe
 209 in contact with the skin directly above the tumor. Images
 210 were captured at several locations on each tumor through
 211 the integrated computer and image analysis system. Normal
 212 tissue images were taken at a location at least 2 cm distant
 213 to the tumor on the same animal. Images were analyzed to
 214 first quantify the contrast levels using standard thresholding
 215 for image analysis, then intensity data were analyzed using
 216 an unpaired Student *t* test assuming equal variance with a
 217 confidence interval of 95%, $\alpha < 0.05$ of the two populations
 218 of images from PBS-treated and nanoshell-treated mice.
 219 Analysis of the tumor regression was performed using the
 220 average measurements of the tumor size of the surviving
 221 populations at the times shown and compared using an
 222 unpaired Student *t* test assuming equal variance with a
 223 confidence interval of 95%, $\alpha < 0.05$.

224 Figure 3 shows OCT imaging results obtained after PBS
 225 injection, panels A and C, and after nanoshell injections,
 226 panels B and D. The strata of the skin and underlying muscle
 227 can be seen in the OCT image of the normal tissue panel A
 228 and B. There is no enhancement in layers of normal tissue
 229 in mice treated with nanoshells compared with the PBS-

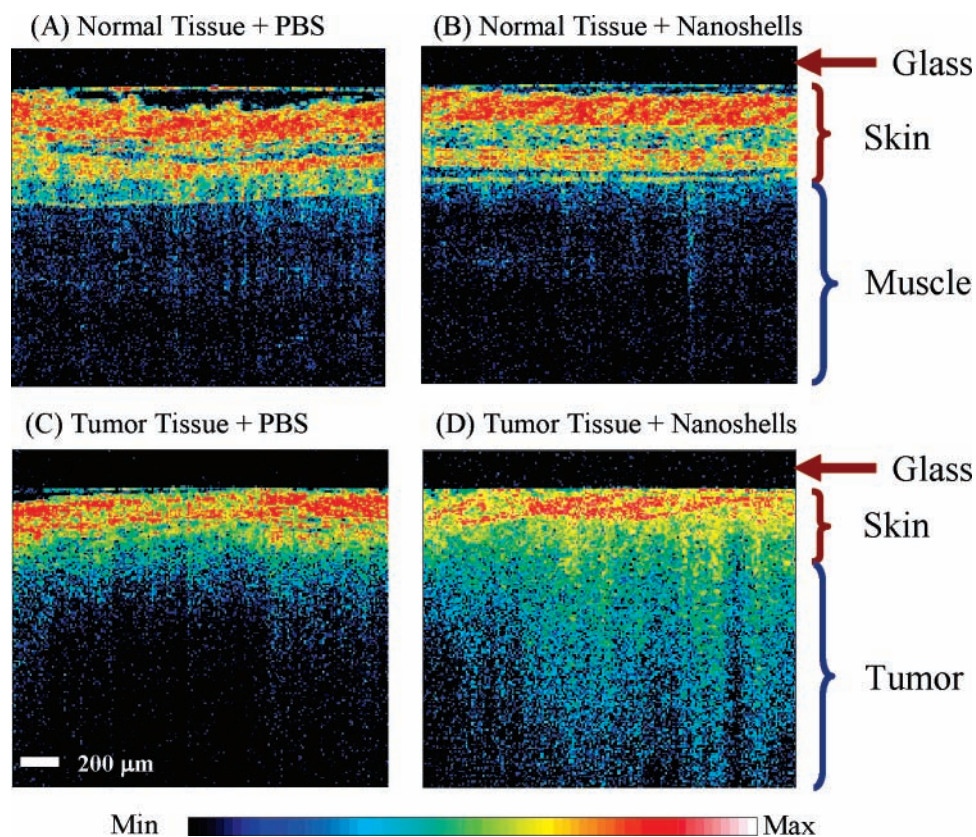


Figure 3. Representative OCT images from normal skin and muscle tissue areas of mice systemically injected with nanoshells (A) or with PBS (B). Representative OCT images from tumors of mice systemically injected with nanoshells (C) or with PBS (D). Analysis of all images shows a significant increase in contrast intensity after nanoshell injection in the tumors of mice treated with nanoshells while no increase in intensity is observed in the normal tissue. The glass of the probe is 200 μm thick and shows as a dark nonscattering layer.

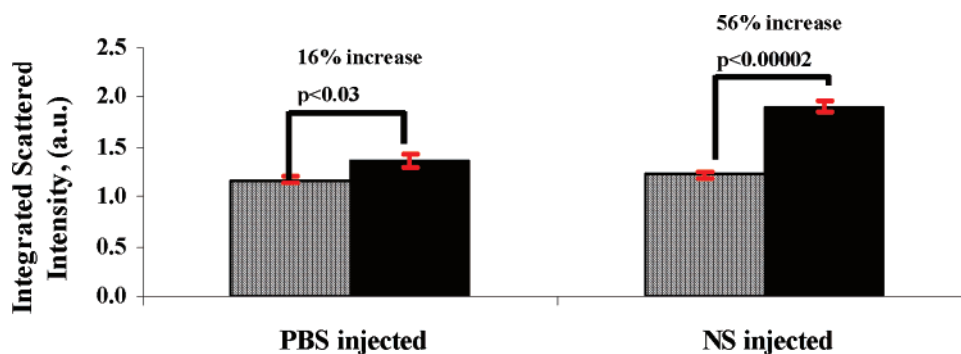


Figure 4. Quantification of OCT images shows a significant increase in intensity of images of tumors from mice with systemic nanoshell injection. Normal muscle tissue is shown in the blue bar while tumor tissue is shown in the black bar. Values are average \pm SEM; p values are shown.

230 injected mouse because nanoshells do not extravasate ap-
 231 preciablely into normal tissues.

232 The enhanced brightness of the image in panel D relative
 233 to panel C of Figure 3, where nanoshells have accumulated
 234 in the tumor, indicates that gold nanoshells can provide
 235 substantial contrast in OCT imaging. Figure 3D also shows
 236 that the borders of tumors (on the left) can more easily be
 237 discerned in the OCT images of nanoshell-treated mice
 238 compared to those mice that had only PBS injection (Figure
 239 3C). Figure 4 shows the quantification of the image intensity
 240 of OCT images of normal tissue ($n = 3$) and tumor tissue (n
 241 $= 6$) with PBS injections and nanoshell injections. Images
 242 were analyzed to first quantify the contrast and then analyzed

243 using a Student's t test of the two populations of images
 244 from PBS-treated and nanoshell-treated mice. The data show
 245 a significant increase in the optical contrast of tumor
 246 compared to normal tissue when nanoshells are used, $p <$
 247 0.00002 . No statistical difference is observed in the intensity
 248 of the optical contrast of images of normal tissue whether
 249 nanoshells are used or PBS.

250 **Nanoshells Also Allow Photothermal Ablation of Tu-**
 251 **mers with Increased Survival.** As described above, tumor-
 252 bearing mice received either nanoshell or PBS injections.
 253 Animals were randomly assigned to control and treatment
 254 groups. Animals were randomly divided into three groups:
 255 treatment (nanoshell + laser); sham (PBS + laser), and

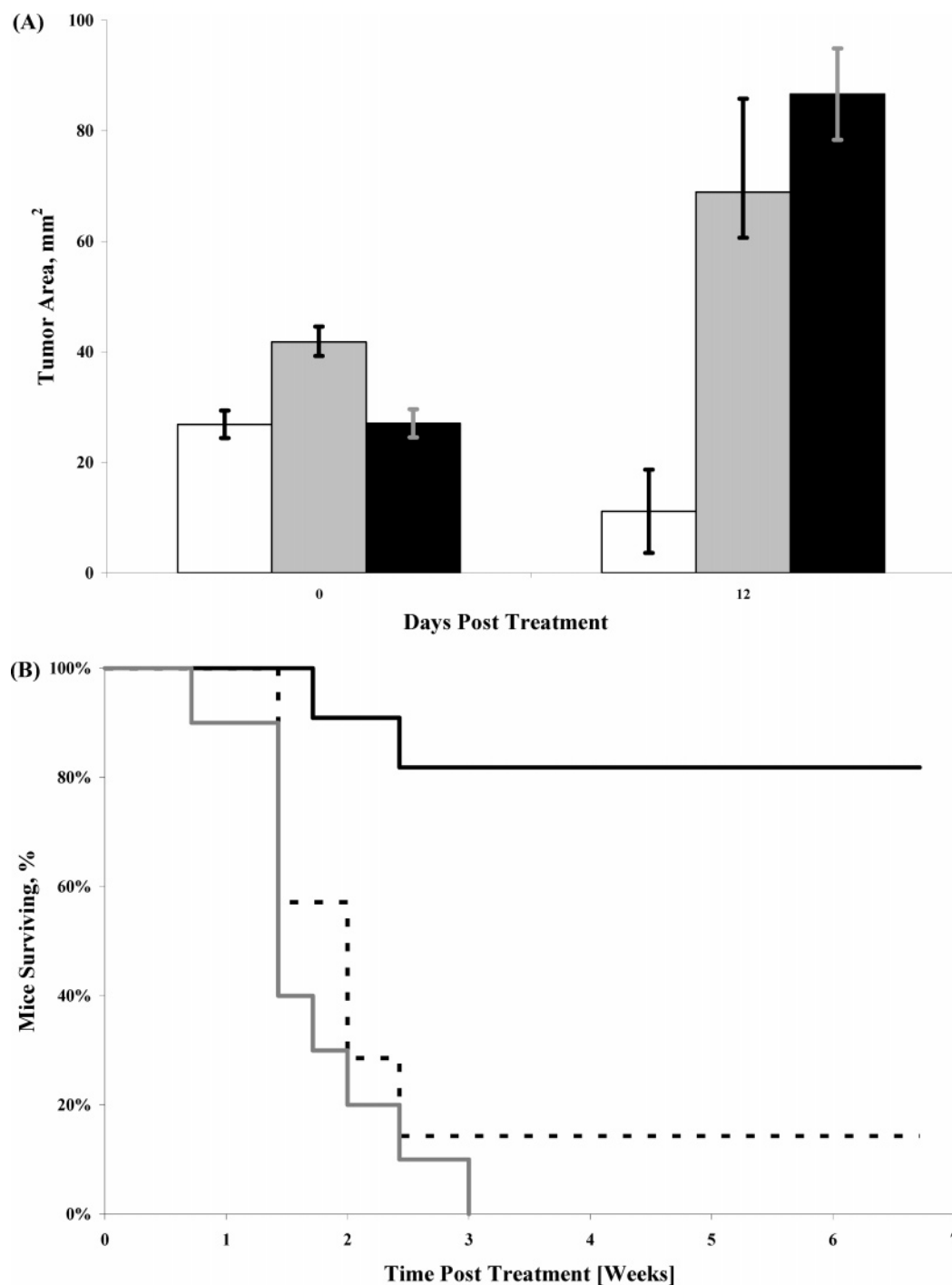


Figure 5. (A) Tumor size before irradiation and 12 days post-irradiation of mice treated with nanoshell + NIR laser irradiation (white bar); PBS sham + NIR laser treatment (gray bar) or untreated control (black bar); values are average \pm SEM. (B) Kaplan–Meier survival data for the treatment groups post irradiation; nanoshell + NIR laser irradiation (solid black line); PBS sham + NIR laser treatment (dashed black line) or untreated control (gray line); survival was followed for 7 weeks posttreatment. After 21 days, the nanoshell therapy group survival rate was significantly higher than either control group, $p < 0.001$.

256 control (untreated). Following OCT imaging as described
 257 above, animals in the treatment and sham groups had their
 258 tumors irradiated with a NIR laser. In vivo irradiation was
 259 accomplished using an Integrated Fiber Array Packet, FAP-I
 260 System, with a wavelength of 808 nm (Coherent, Santa Clara,
 261 CA) at a power density of 4 W/cm² and a spot size of 5 mm
 262 diameter for 3 min. Tumor size and animal survival was
 263 monitored for 7 weeks after imaging and treatment. Survival

data analysis was performed using the standard Kaplan–
 Meier analysis using MedCalc software.

Figure 5A shows the tumor sizes on the day of treatment
 and 12 days after treatment; tumors on all but two nanoshell-
 treated mice had completely regressed. Figure 5B shows the
 survival of the mice during the entire study period. Kaplan–
 Meier statistical analysis shows a median survival of 14 days
 for the PBS + laser group and 10 days for the untreated

272 control group. By day 21, the survival of the nanoshell +
 273 laser group was significantly greater than either the control
 274 or sham groups, $p < 0.001$, and this then continued for the
 275 duration of the study. Median survival time could not be
 276 calculated for this group, as the long-term survival was 83%.

277 We have reported the successful in vivo demonstration of
 278 a single nanoparticle that enhances the scattering signal for
 279 OCT imaging while retaining its properties to affect photo-
 280 thermal ablation of the tumor. Our findings suggest that
 281 engineered nanoparticles, such as nanoshells with tunable
 282 optical properties, can indeed play a vital role in a number
 283 of emerging in vivo molecular imaging modalities and allow
 284 integration of diagnostic and therapeutic technologies.

285 **Acknowledgment.** This work was funded by the DOD
 286 CDMRP in Breast Cancer DMI-0319965 and by the NSF
 287 NSEC Center for Biological and Environmental Nanotech-
 288 nology (CBEN) EEC-0647452, NIH 5R01CA109385.

289 References

- 290 (1) Sullivan, D. C.; Ferrari, M. *Mol. Imaging* **2004**, *3*, 364–369.
 291 (2) Ferrari, M. *Nat. Rev. Cancer* **2005**, *5*, 161–171.
 292 (3) Averitt, R.; Westcott, S.; Halas, N. *J. Opt. Soc. Am. B* **1999**, *6*, 1824–
 293 1832.
 294 (4) Oldenburg, S. J.; Averitt, R. D.; Westcott, S. L.; Halas, N. J. *Ch.*
 295 *Phys. Lett.* **1998**, *288*, 243–247.
 296 (5) Oldenburg, S. J.; Jackson, J. B.; Westcott, S. L.; Halas, N. J. *Appl.*
 297 *Phys. Lett.* **1999**, *75*, 2897–2899.
 298 (6) Loo, C.; Lowery, A.; Halas, N.; West, J.; Drezek, R. *Nano Lett.* **2005**,
 299 *5*, 709–711.
 300 (7) Loo, C. H.; Lin, A.; Hirsch, L.; Lee, M.; Barton, J. K.; Halas, N. J.;
 301 West, J. L. *Technol. Cancer Res. Treat.* **2004**, *3*, 33–40.
 302 (8) Hirsch, L. R.; Stafford, R. J.; Bankson, J. A.; Sershen, S. R.; Rivera,
 303 B.; Price, R. E.; Hazle, J. D.; Halas, N. J.; West, J. L. *Proc. Natl.*
 304 *Acad. Sci. U.S.A.* **2003**, *100*, 13549–13554.
 305 (9) O’Neal, D. P.; Hirsch, L. R.; Halas, N. J.; Payne, J. D.; West, J. L.
 306 *Cancer Lett.* **2004**, *209*, 171–176.
 307 (10) Averitt, R. D.; Westcott, S. L.; Halas, N. J. *J. Opt. Soc. Am. B* **1999**,
 308 *16*, 1824–1832.
 (11) Weissleder, R. *Nat. Biotechnol.* **2001**, *19*, 316–317. 309
 (12) Hirsch, L. R.; Jackson, J. B.; Lee, A.; Halas, N. J.; West, J. L. *Anal.* 310
Chem. **2003**, *75*, 2377–2381. 311
 (13) Sershen, S. R.; Westcott, S. L.; Halas, N. J.; West, J. L. *J. Biomed.* 312
Mater. Res. A **2000**, *51*, 293–298. 313
 (14) Gobin, A.; O’Neal, D.; Watkins, D.; Halas, N.; Drezek, R.; West, J. 314
Lasers Surg. Med. **2005**, *37*, 123–129. 315
 (15) Loo, C.; Hirsch, L.; Lee, M.-H.; Chang, E.; West, J.; Halas, N.; 316
 Drezek, R. *Opt. Lett.* **2005**, *30*, 1012–1014. 317
 (16) Fujimoto, J. G.; Brezinsky, M. E.; Tearney, G. J.; Boppart, S. A.; 318
 Bouma, B.; Hee, M. R.; Southern, J. F.; Swanson, E. A. *Nat. Med.* 319
1995, *1*, 970–972. 320
 (17) Huang, D.; Swanson, E. A.; Lin, C. P.; Schuman, J. S.; Stinson, W. 321
 G.; Chang, W.; Hee, M. R.; Flotte, T.; Gregory, K.; Puliafito, C. A. 322
Science **1991**, *254*, 1178–1181. 323
 (18) Matheny, E. S.; Hanna, N. M.; Jung, W. G.; Chen, Z.; Wilder-Smith, 324
 P.; Mina-Araghi, R.; Brenner, M. *J. Biomed. Opt.* **2004**, *9*, 978– 325
 981. 326
 (19) Li, X. D.; Boppart, S. A.; Dam, J. V.; Mashimo, H.; Mutinga, M.; 327
 Drexler, W.; Klein, M.; Pitris, C.; Krinsky, M. L.; Brezinski, M. E.; 328
 Fujimoto, J. G. *Endoscopy* **2000**, *32*, 921–930. 329
 (20) Izatt, J. A.; Kulkarni, M. D.; Wang, H.-W.; Kobayashi, K.; Sivak, 330
 M. V. *IEEE J. Sel. Top. Quantum Electron.* **1996**, *4*, 1017–1028. 331
 (21) Tearney, G. J.; Brezinski, M. E.; Southern, J. F.; Bouma, B. E.; 332
 Boppart, S. A.; Fujimoto, J. G. *Am. J. Gastroenterol.* **1997**, *92*, 1800– 333
 1804. 334
 (22) Kobayashi, K.; Izaat, J.; Kulkarni, M.; Willis, J.; Sivak, M. 335
Gastrointest. Endosc. **1998**, *47*, 515–523. 336
 (23) D’Amico, A. V.; Weinstein, M.; Li, X.; Richie, J. P.; Fujimoto, J. 337
 G. *Urology* **2000**, *55*, 783–787. 338
 (24) Sergeev, A. M.; Gelikonov, V. M.; Gelikonov, G. V.; Feldchtein, F. 339
 I.; Kuranov, R. V.; Gladkova, N. D. *Opt. Exp.* **1997**, *1*, 432–440. 340
 (25) Barton, J. K.; Hoying, J. B.; Sullivan, C. J. *Acad. Radiol.* **2002**, *9*, 341
 S52–S55. 342
 (26) Lee, T. M.; Oldenburg, A. L.; Sitafalwalla, S.; Marks, D. L.; Luo, 343
 W. *Opt. Lett.* **2003**, *28*, 1546–1548. 344
 (27) Oldenburg, A. L.; Hansen, M. N.; Zweifel, D. A.; Wei, A.; Boppart, 345
 S. A. *Opt. Exp.* **2006**, *14*, 6724–6738. 346
 (28) Duff, D. G.; Baiker, A.; Edwards, P. P. *Langmuir* **1993**, *9*, 2301– 347
 2309. 348
 (29) James, W. D.; Hirsch, L. R.; West, J. L.; O’Neal, P. D.; Payne, J. D. 349
J. Radioanal. Nucl. Chem. **2006**, *271*, 455–459. 350
 NL070610Y 351

Enhanced gold nanoshell scattering contrast using angled fiber probes

Vengadesan Nammalvar*, Adrien Wang*, Rebekah Drezek

Department of Bioengineering
Rice University, 6100 Main St., MS-142, Houston, TX 77005
drezek@rice.edu

*Shared principal authorship

Abstract. Gold nanoshells are positioned to become a scattering-based contrast agent to improve the reflectance signals of nanoshell-targeted tissue. However, our study shows that a greater enhancement of nanoshell-induced reflectance signals can now be achieved when angularly oblique fiber geometries are used in place of the conventional orthogonal fiber geometry. This important finding was confirmed by conducting two experiments. First, diffuse reflectance spectra were collected from nanoshell-infused polystyrene phantoms at 0, 10, 20, 30 and 40 degree collection angles. At the 40 deg. fiber angle, the nanoshell-induced reflectance contrast, with respect to the native polystyrene phantom, is significantly increased. Based on these results, a reflectance study was then conducted for human cervical tissue treated with gold nanoshells at the 0 and 40 degree collection angles. Again, at the 40 deg. fiber angle, the signal level of the nanoshell-induced contrast in tissue is determined as statistically significant. Taken together, these results demonstrate that the use of the angularly oblique fiber geometry does significantly improve reflectance contrast.

Keywords: nanoshells, fiber probes, reflectance spectroscopy, scattering contrast.

1 INTRODUCTION

Of all gynecologic diseases in the United States, uterine-cervical cancer leads in mortality rate. Hence, early detection of cervical epithelial abnormalities is believed to be the best strategy in reducing this alarming statistic. However, many currently available screening techniques for epithelial cancers do not provide adequate sensitivity and specificity at the earliest stages of diagnosis and treatment. Thus, a more sensitive and quantitative diagnostic technique is required in order to identify diseased tissue at the early malignant stages.

A promising candidate, which meets these requirements, is reflectance spectroscopy because it has been shown that this method can characterize morphological changes in diseased tissue at various organ sites [1,2]. Since nearly 85% of all cancers originate in epithelia, specific probing of epithelia may help extract diagnostically useful information from this thin tissue. To accomplish this, recent studies have demonstrated that fiber geometry directly affects the spatial distribution of the detected reflectance and consequently changes the probing depths in tissue [3-8]. This then results in refining the selection and separation of epithelia from surrounding biological materials, which will, in turn, improve the accuracy of disease diagnosis for epithelial cancers.

Spatially-resolved reflectance spectroscopy has shown promising results in overcoming the spatial limitations associated with conventional reflectance-based techniques when implemented in turbid biological media. Indeed, optical contrast agents attract considerable attention in biophotonics because of their potential for detecting pathogenesis at molecular levels. For example, gold nanoshells can be labeled with particular antibodies that specifically conjugate to targeted proteins preferentially expressed by malignant cancer cells [9-11]. Consequently, a significant accumulation of nanoshells around cells, or in tissue, due

to this selective binding, can indicate the presence of malignancies which otherwise would remain undetected by traditional white light endoscopy. In addition to their utility as a contrast agent, gold nanoshells may also be used in photo-thermal therapy [12,13]. This procedure takes advantage of the ability of nanoshells to absorb NIR radiation and thus cause cancer cells to be thermally ablated by intense, albeit locally confined, heat. This procedure is highly selective and specific and results in minimal damage to the surrounding healthy tissue [12-14].

By varying their core/shell ratio and overall size, nanoshells can be produced with strong scattering or absorption efficiencies. Therefore, nanoshells can be used for either scattering-based contrast enhancements in imaging applications [12] or photo-thermal tissue ablation in therapeutic procedures [13,14]. Unfortunately, the scattering and absorptive properties of nanoshells are size-dependent, making it rather difficult to maximize one aspect of the nanoshells' optical characteristics without sacrificing the other. However, the use of an angularly-oblique fiber probe can overcome this complication. Specifically, the geometry of such probes results in more efficient detection of back-scattered photons and, thus, more efficiently detects the back-scattered reflectance from nanoshells. The consequence of using such fiber geometry is that nanoshell signals can be significantly increased to exceed those levels currently detectable with conventional orthogonal fiber probes.

2 METHODS AND MATERIALS

2.1 Nanoshell preparation

The gold nanoshells used in this study have two core sizes: 86 and 200 nm in diameter. The silica cores are synthesized using the Stöber method [15], with which tetraethylorthosilicate is synthesized into spherical colloids in ethanol. These Stöber spheres are then functionalized with aminopropyltriethoxysilane, resulting in silica cores with attached amine groups. Then, gold colloids (1-3 nm in diameter) adsorb to the amine group and provide nucleation for further reduction of gold [16]. The reduction of additional gold colloids onto the seeded cores results in a complete coalescence of gold shell. Prior to reflectance experiments, nanoshell surfaces are modified with thiolated polyethylene glycol to provide steric stabilization.

In all, four sizes of nanoshells are used for the phantom study. Beginning with the smallest, these nanoshells have core/shell diameters of 86/104, 86/124, 200/228 and 200/262 nm, as empirically determined by SEM measurements. Among the four types of nanoshells, the 86/104 nm nanoshells are particularly strong in their absorption efficiency, while the 200/268 nm nanoshells are, predominantly, strong in scattering efficiency. The other two sizes (86/124 and 200/228 nm) have similar levels of scattering and absorption efficiency at the targeted spectral wavelengths of this study (400 – 1000 nm).

For the tissue study, nanoshells with the core/shell diameters of 86/114 nm are used because they are produced after the completion of the phantom study. It should be noted that reproducing any one specific size of nanoshells is extremely difficult. Therefore, although it is certainly ideal to employ the same sizes of nanoshells for both the phantom and tissue experiments, the use of the 86/114 nm nanoshells for the latter is a reasonable compromise.

2.2 Polystyrene microsphere phantoms with gold nanoshells

Polystyrene phantoms are used to mimic the optical properties of human cervical tissue. These tissue phantoms have a depth of 25 mm, which is sufficient to represent an optically semi-infinite tissue, and a diameter of 22 mm, which is wide enough to encompass all optical paths collectible by our particular fiber geometry.

Mono-dispersed polystyrene microspheres are the sources of scattering for the phantoms. A mixture of polystyrene microspheres (5.43 μm in diameter) in water is used in

this study to provide scattering properties similar to those of human cervical tissue. India ink is added to the phantoms to provide adequate levels of absorption coefficients. The optical properties of human cervical tissue are based on the values reported by Collier [17], Drezek [18], and Chang [19] et al. that were previously adopted by Zhu [20], Skala [3] and Wang [5,7,8] et al. in their respective studies on epithelial tissue. The scattering coefficients (μ_s) and anisotropies (g) of the phantoms are calculated in accordance with Mie theory, and the absorption coefficients are experimentally determined. The values for the scattering (μ_s) and absorption (μ_a) coefficients of the polystyrene phantoms can be found in Fig. 1.

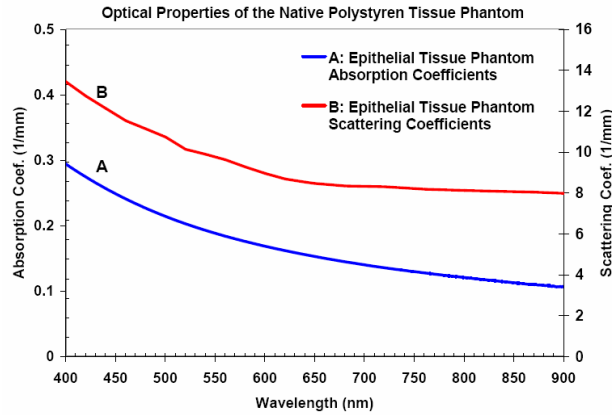


Fig. 1. The scattering and absorption coefficients of the native polystyrene phantom (5.43 μm) before addition of nanoshells.

To assess changes in reflectance signal after nanoshell addition, the four sizes of gold nanoshells, as noted above, are then mixed with the tissue phantoms. No more than 300 μL of nanoshell-suspensions are added to the phantoms, which have the original volume of 9.5 mL. The perturbation on the overall phantom volumes due to the added nanoshell suspensions is no more than 3%, thus eliminating the concern of significant dilution of the native phantom properties. By estimation using Mie theory, there are roughly 3×10^{10} nanoshells per cm^3 inside the phantoms.

2.3 Tissue preparation

Eight malignant and eight normal cervical tissue samples are infused with gold nanoshells. After removal from the freezer, the frozen tissue samples are placed and maintained on a cold plate for the duration of the experiment. The cold plate stabilizes at approximately 6 deg. Celsius and therefore retards the rate of structural degradation in tissue due to thawing. Consequently, the tissue sample properties remain reasonably constant during the experiment (approximately 1 hour from the time of tissue retrieval from the freezer). As noted above, we use only the 86/114 nm nanoshells for the tissue study. Two hundred μL of nanoshell fluid ($5 \times 10^{10}/\text{mL}$) are directly injected into the cervical tissue samples via 25 gauge needles. The needles penetrate no more than 1 mm into the tissue. Fifteen minutes after the injection, the tissue samples are rinsed with buffered saline to remove loose nanoshells on or above the tissue, and the reflectance is measured.

It should be noted that, due to phenomenon such as loss of nexus [21] and increased extra-cellular space [22, 23], the physical structures of dysplastic tissue is more porous than those of normal tissue. As a consequence, abnormal tissue is receptive to nanoshell injection.

In contrast, it is much more difficult to pierce normal tissue, which has strong structural resilience against the introduction of foreign objects or elements. While we did successfully pierce the normal tissue, nanoshell retention in this tissue is less than optimal. By our visual observations, the abnormal tissue seems to absorb more nanoshell fluid than the normal tissue; therefore, we believe that the increased permeability of particles in dysplastic tissue would facilitate nanoshell redistribution and retention. On the other hand, a large portion of the injected nanoshell fluid leaked out of the normal tissue because the space between tissue fibers was insufficient to accommodate the entire 200 μ L of nanoshell fluid.

Since the normal and abnormal tissues retain unequal amounts of nanoshells, quantitative comparisons between the two are slightly less straightforward. Nonetheless, epidermal injection of nanoshells in tissue, in our opinion, is still valid since the unequal nanoshell retentions directly result from the tissues' natural physical properties. Thus, similar observations would appear in all tissue studies, both *in vitro* and *in vivo*. Significantly, we believe that the preferential retention of nanoshells is a natural attribute of the dysplastic tissue. This creates conditions which, in fact, improve the ability of nanoshells to preferentially target diseased tissue. This study focuses on enhancing the capabilities of nanoshell-induced signals in tissue, regardless of the tissue types. Since we are primarily interested in comparing spectra obtained from the same tissue at different fiber angles, the amount of nanoshells retained by either tissue type is, from our perspective, not the focus of this study.

2.4 Fiber geometry

The configuration of the source and collection fibers is controlled with a fiber stage that independently adjusts the fiber obliquity with respect to the normal and malignant tissues. Throughout this study, we maintain the source fiber at the orthogonal orientation and only investigate the angles of the collection fiber in relation to the target surface. Tissue phantom reflectance is sampled at 0, 10, 20, 30 and 40 degrees; based on the phantom study, tissue reflectance is sampled at two collection angles, 0 and 40 degrees, measured out of the plane of tissue surface. The operational uncertainty of the fiber angles is smaller than 0.5° in magnitude. The source and collection fibers, of which the core diameter and nominal numerical aperture are 200 μ m and 0.22, are connected to a broadband light source and spectrophotometer, respectively. The distance between the source and collection fibers, measured from their respective geometric center, is 300 μ m. All reflectance measurements are referenced to a 99% reflectance standard when the fibers are at 0 degree. Since reflectance intensities collected at the 40 deg. angle are in multiples of those collected at the 0 deg. angle, the reflectance reading for the 40 deg. fibers may exceed 100%.

3 RESULTS

3.1 Nanoshells in tissue phantoms

Figures 2A and B show the reflectance spectra obtained from the 86/104 and 86/124 nm nanoshell-phantoms and native polystyrene phantom at 0 and 40 deg. fiber angles, respectively. At the 0 degree, both nanoshell-infused polystyrene phantoms, in fact, have lower reflectance than the native polystyrene (non-nanoshell) phantom at wavelengths smaller than 700 nm. At longer wavelengths, where the nanoshell scattering efficiency surpasses that of the polystyrene microspheres, we begin to observe noticeable nanoshell signals, and the reflectance levels are enhanced due to the nanoshell infusions. However, when the fiber angle increases to 40 degrees, we observe significant increases of reflectance from the nanoshell-phantoms relative to those of the native polystyrene phantom. Similar trends are seen for the

200/228 and 200/268 nm nanoshell-phantoms with respect to the native polystyrene phantoms, as shown in Fig. 3A and B.

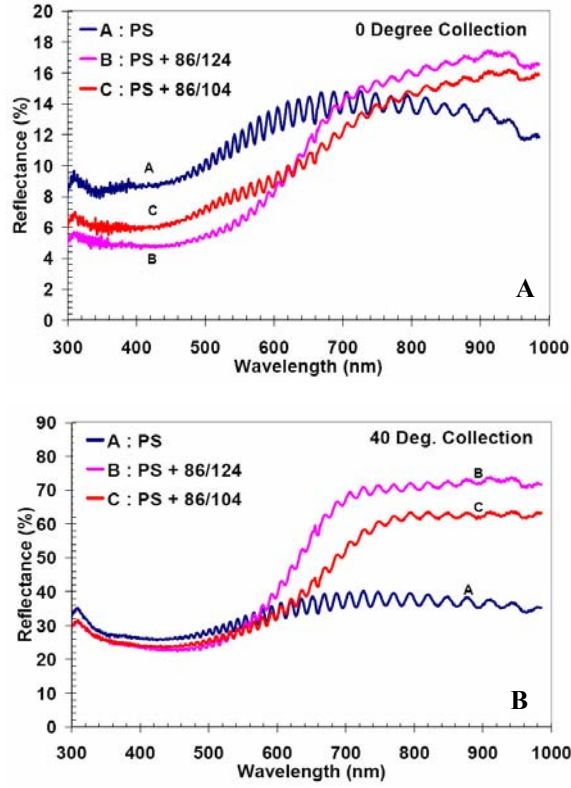


Fig. 2. Reflectance spectra of native polystyrene phantom and nanoshell-infused (86/104 and 86/124 nm) phantoms at (A) 0 deg. and (B) 40 deg. collection fiber angles.

In order to quantitatively assess the contributions of nanoshell reflectance relative to those of the polystyrene beads, we calculate the integrated reflectance intensity of the phantoms across the wavelength spectrum (400 – 1000 nm). The term “area under curve” or AUC is used to denote this metric. We then define the contrast supplied by the nanoshells in the phantoms as a ratio between the AUC of the nanoshell-infused phantoms and the AUC of the native polystyrene phantom. The mathematical formulation of the nanoshells’ contrast in the phantoms is expressed in Eq. (1).

$$\text{Contrast}(\text{Nanoshell} + \text{PS Phantom}) \equiv \frac{\text{AUC}(\text{Nanoshell} + \text{PS Phantom})}{\text{AUC}(\text{PS Phantom})} \quad (1)$$

This ratio thus serves as a quantitative measurement of the nanoshells’ contribution to the detected reflectance as an exogenous contrast agent in the tissue phantoms. As shown in Fig. 4A and B, invariably stronger reflectance contrasts are detected from the nanoshell-infused phantoms at higher angles than those detected at lesser angles. More significantly, with the orthogonal fiber geometry (0 deg.), three of the four nanoshell-infused phantoms produce lower reflectance intensities than the native polystyrene phantom, indicating that the absorptive effect due to nanoshells may, in fact, supersede the scattering increase and

consequently results in lower reflectance signals. Effectively, their AUC ratios are smaller than 1, which equivalently signifies a negative contrast that actually diminishes the reflectance signal from the phantoms. Since our premise of using exogenous contrast agent is to increase the reflected signal, the instances of diminished reflectance from the nanoshell-infused phantoms are undesirable.

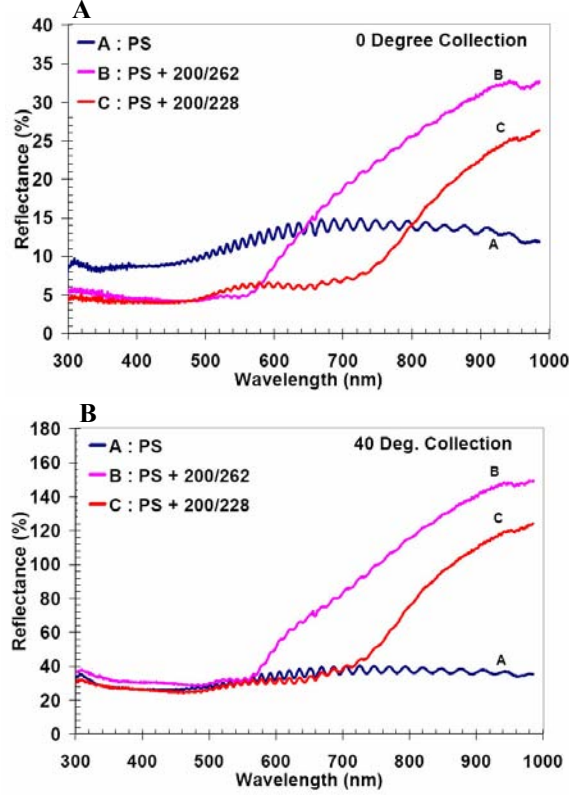


Fig. 3. Reflectance spectra of native polystyrene phantom and nanoshell-infused (200/228 and 200/262 nm) phantoms at (A) 0 deg. and (B) 40 deg. collection fiber angles.

Table 1 lists the contrast levels induced by nanoshells when the nanoshell-phantoms are measured at both 0 and 40 deg. fiber angles. The level of contrast increase is defined as the difference of the contrast ratios, as defined in Eq. (1), between the nanoshell-infused and native polystyrene phantoms. The explicit formulation of this metric is shown in Eq. (2).

$$\begin{aligned}
 \text{Contrast Increase} &\equiv \frac{AUC(\text{Nanoshell} + \text{PS Phantom})}{AUC(\text{PS Phantom})} - \frac{AUC(\text{PS Phantom})}{AUC(\text{PS Phantom})} \\
 &= \frac{AUC(\text{Nanoshell} + \text{PS Phantom})}{AUC(\text{PS Phantom})} - 1
 \end{aligned} \tag{2}$$

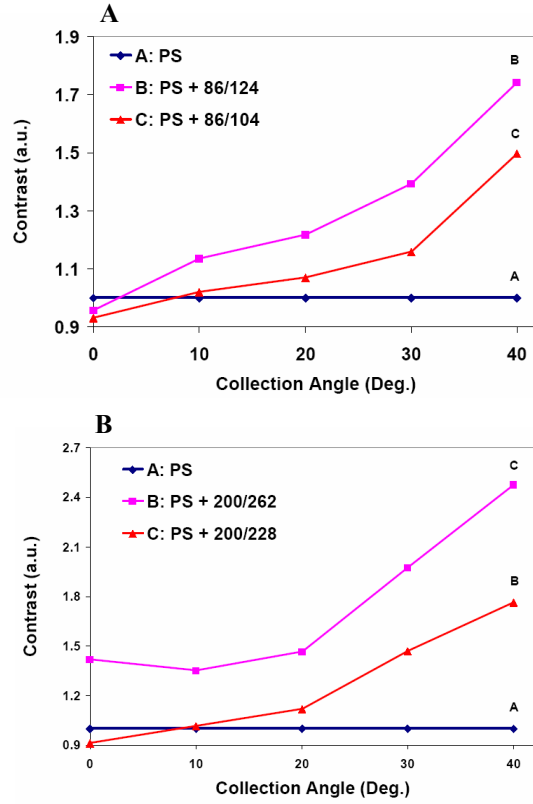


Fig. 4. Nanoshell-induced contrast with respect to the native polystyrene phantom of (A) 86/104 and 86/124 and (B) 200/228 and 200/262 nm sizes of gold nanoshells.

Table 1. Nanoshells-induced contrast with respect to the native PS phantom at 0 and 40 deg. collection fiber angles.

Fiber Angles	<i>Types of Nanoshells in PS Phantoms</i>			
	<i>86/124 nm</i>	<i>86/104 nm</i>	<i>200/262 nm</i>	<i>200/228 nm</i>
0 Deg.	-4.36%	-6.86%	41.72%	-8.95%
40 Deg.	74.07%	49.54%	147.4%	76.34%

Among the four different sizes of nanoshells (86/104, 86/124, 200/228 and 200/262 nm) infused in the polystyrene phantoms, we obtain a consistent trend which indicates that nanoshell-induced reflectance contrasts, when sampled at the 40 deg. angle, are considerably higher than those sampled at the orthogonal fiber geometry. This, in turn, leads us to conclude that nanoshell-induced scattering signals can be better detected at higher fiber angles, and the expected contrast enhancement is, consequently, more significant. In contrast, at the 0 deg. fiber angle, 3 out of the 4 nanoshell-infused phantoms exhibit negative contrasts with respect to the native polystyrene phantom.

3.2 Nanoshells in cervical tissue

Figures 5A and B contain the reflectance spectra measured from the human cervical tissues both before and after the injection of nanoshells. Figure 5A contains the data collected from the normal cervical tissues, and Fig. 5B contains the abnormal tissue data. The standard deviations of the measurements are displayed at the 750 nm wavelength, where the peak of nanoshell reflectance is located. With the 0 deg. fiber geometry, the resultant reflectance spectra of the tissue after nanoshell injection virtually overlap those measured before the nanoshell introduction in tissue, and consequently little evidence of nanoshell scattering is present in the reflectance spectra for either tissue type. On the other hand, significant nanoshell-induced contrast is present in the tissue spectra when the 40 deg. fibers are used.

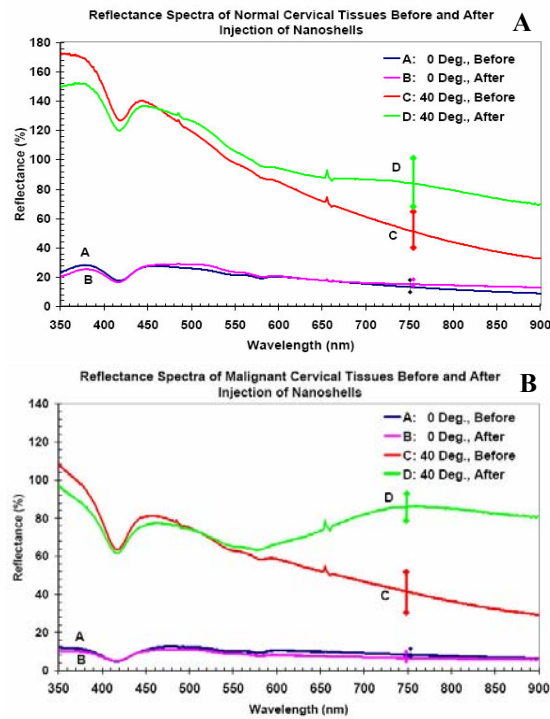


Fig. 5. Reflectance spectra measured from the (A) normal and (B) abnormal human cervical tissues both before and after the injection of nanoshells.

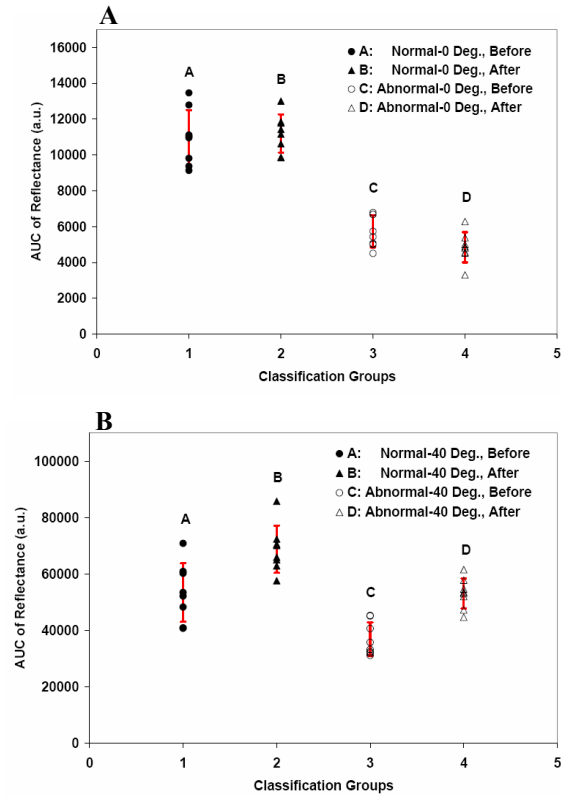


Fig. 6. AUC distributions of the classification groups (normal and abnormal tissues before and after nanoshell application) when measured at (A) the 0 deg. and (B) 40 deg. fiber angle.

Table 2. Significance levels (p-values) of Wilcox rank-sum test (two-tailed) between the tissue samples before and after application of gold nanoshells at 0 and 40 deg. collection fiber angles.

Group Discrimination: Before v. After Nanoshell Application	Fiber Angles	
	0 Deg.	40 Deg.
Normal Tissues	0.430	0.013
Abnormal Tissues	0.066	0.001

In the abnormal cervical tissue, the nanoshell signals are especially strong and definitive. In order to quantify the level of significance of nanoshell-induced contrast, we calculated the integrated intensity of the spectra, or AUC, of the tissue samples before and after the injection of nanoshells for both normal and malignant tissues. The AUC values of the individual tissue samples are shown in Fig. 6A and B. Figure 6A, which represents the AUC distributions of the tissue spectra when the 0 deg. fibers are used, indicates a limited intensity difference caused by the application of nanoshells in tissue. In contrast, Fig. 6B shows that significant intensity differences are observable, particularly for the abnormal tissues, when the 40 deg. fibers are used. Further, based on the AUC value, we calculated the statistical significance of nanoshell-induced contrast among the tissue samples by using Wilcoxon rank-sum test (two-tailed). The Wilcoxon test is a non-parametric test, which is appropriate for the small number of samples used in this study, for which a normal distribution can not be assumed. The results of the Wilcoxon rank-sum test are shown in Table 2, and, based on these data, we observe that the level of nanoshell-induced contrast is significantly stronger when tissue-nanoshell reflectance is collected at the 40 deg. fiber angle than instances where the 0 deg. angle is used. However, more interestingly, the nanoshell-induced contrast in the abnormal tissue (p -value = 0.001) is more significant than that in the normal tissue (p -value = 0.013), even when the 40 deg. fiber angle is used for both tissue types. The stronger significance of nanoshell-induced contrast in the abnormal tissue is most likely the consequence of the preferential retention of nanoshell fluids following the epidermal injection, as previously discussed in the penultimate paragraph of section 2.3.

4 DISCUSSION

4.1 The phantom study

Our initial hypothesis speculates that nanoshell signals can be better collected with oblique fiber geometry than with the conventionally utilized orthogonal fibers. This hypothesis originates from the anisotropic behavior of nanoshell scattering. To explain, the nanoscopic dimensions of nanoshells induce particularly strong back-scattering, while most tissues and cellular elements are predominantly forward scattering. This makes nanoshells a strong candidate for use as a scattering-based contrast agent. However, this enhanced back-scattering may not necessarily translate to increased reflectance measurements when the geometry of the detector is not correspondingly optimized for back-scattered signals from shallow depths of tissue. Specifically, because the 0 deg. fiber geometry is primarily sensitive to deeper tissue depths, the superficially scattered light by nanoshells is unlikely to be detected by the same fiber geometry. The contribution of nanoshell-induced contrast is consequently diminished. The oblique fiber geometry [3-8], on the other hand, is particularly sensitive to superficially scattered light in tissue and is, therefore, more likely to enhance the nanoshell signals, consequently producing greater contrast in tissue reflectance.

The phantom study is an appropriate model by which to confirm the validity of our hypothesis. Accordingly, the data shown in section 3.1 do substantially confirm our hypothesis because the results demonstrate that the nanoshell-infused phantoms do exhibit stronger reflectance than the native polystyrene phantoms when the 40 deg. fibers are used in place of the conventional orthogonal fibers. Interestingly, due to the absorptive properties of nanoshells, the added nanoshells actually result in less reflectance signal and an equivalence of “negative” contrast, when the orthogonal fiber geometry used. This is undesirable for applications of scattering-based imaging or spectroscopy that demand exogenous contrast agents to augment the reflected signal levels beyond those of native cellular or tissue materials. However, by using an epithelial-simulating polystyrene phantom, we have successfully demonstrated that, with gradual increase of the collection angle, the contrast between the nanoshell-infused and native polystyrene phantoms consistently increases, as noted above. More importantly, by applying the 40 deg. fibers, we are able to use the 86/104

nm nanoshells, which are conventionally regarded as strongly absorbing nanoshells and thus not suitable for imaging applications, to produce at least 50% more reflectance than the native polystyrene phantoms.

4.2 The tissue study

Reflectance measurements are taken from the normal and malignant cervical tissues before and after application of nanoshells. Based on the data shown in section 3.2, we are able to achieve consistent results, which confirm the enhanced nanoshell contrast in tissue. From the results shown in Fig. 5A and B, it is clear that nanoshell-induced contrast is much more conspicuous when the collection fiber is oriented at 40 degrees. On the other hand, little differentiation can be made between the naked and nanoshell-infused tissue when the orthogonal fiber geometry is used, which limits the potential of using nanoshells as effective scattering-based tumor markers when the fiber geometry is not optimized. In particular, the spectral characteristics of the nanoshells are best manifested in the reflectance spectra of the abnormal tissue. This is true because nanoshells can preferentially accumulate in abnormal tissue due to its porous and permeable structure, as previously discussed in the penultimate paragraph in section 2.3. In addition, the preferential accumulation of nanoshells in tissue can be further amplified when nanoshells are labeled with antibodies that specifically conjugate to malignant cells. Because of this selective binding, nanoshell-specific spectral signals can indicate the presence of pathogenesis which otherwise would remain undetected by traditional white light endoscopy. However, in order to determine the level of nanoshell accumulation in tissue and successfully implement this strategy, two requirements must be met: (1) the excitation of strong nanoshell signals from the nanoshell-rich tissue regions and, more importantly, (2) significant differentiation based on the reflected signals (in the context of this work, the reflectance levels, or AUC). However, based on the result given in section 3.2, virtually no spectral or intensity difference is seen after the nanoshell injection in tissue when the 0 deg. fiber is the selected fiber geometry for reflectance measurement.

Comparing the normal and malignant tissue, it is also clear that the malignant tissue, as expected, favorably retains the injected nanoshells and, therefore, exhibits greater nanoshell-induced reflectance contrast than the normal tissue. It is also encouraging to observe significant nanoshell-induced contrast in the abnormal tissue samples, although we did not administer antibody conjugation in this study. As discussed in section 2.3, the preferential retention of nanoshells in abnormal tissue is most likely attributed to the increased permeability of the malignant tissue, a phenomenon which should be consistent for all *in vitro* and *in vivo* studies. Thus, we expect even greater improvement of nanoshell-induced contrast when specific antibodies are conjugated onto the nanoshell surface. As noted above, antibody targeting is not used in this study. Nevertheless, we can still identify the pathological status of the tissue samples (normal v. malignant) based on the nanoshell-induced signals present in the overall reflectance spectra, as shown in Fig. 6A and B. In the malignant tissue, the nanoshell-induced contrast is considerably stronger than that for the normal tissue. The affirming observations that nanoshells are an effective source of exogenous scattering contrast can be seen from the AUC results shown in Table 2 and Fig. 6A and B. These data, based on the statistical discrimination of the Wilcoxon rank-sum test, also confirm that the use of nanoshells results in more significant reflectance contrast in the malignant tissue than in the normal tissue, as demonstrated by their respective AUC values. Most importantly, we consistently observed increased nanoshell-induced contrast for both tissue types when the 40 deg. fiber is used in place of the 0 deg. fiber. This strongly suggests the possibility of enhancing nanoshell signals in tissue environments by using obliquely oriented fiber geometry.

5 CONCLUSION

We have found that the detection capability of nanoshell-induced scattering contrast, in both tissue phantoms and human cervical tissues, increases as the obliquity of collection fibers increases. More specifically, by using an oblique collection fiber at the 40 deg. angle, the nanoshell-induced signals in both tissue phantoms and cervical tissues are significantly higher and discernable than those detected with the conventional orthogonal fiber geometry. In the phantom study, we have also demonstrated that the 86/104 nm nanoshells, which are conventionally regarded as absorbing nanoshells, can be used in applications that demand high scattering contrast. With the 86/104 nm nanoshells, we were able to produce at least 50% more reflectance than the native polystyrene phantom by using the 40 deg. fibers, indicating the possibility of using predominantly absorbing nanoshells for scattering-based contrast enhancement.

For the tissue study, the same conclusion is drawn: that the use of a higher fiber angle (40 deg.) considerably increases nanoshell-induced contrast. Based on the results of this *in vitro* experimentation, we have established a pilot study that addresses the possibility of combining nanoshells and angularly-variable fiber geometries to increase the level of nanoshell-induced contrast in tissue reflectance, which may consequently result in more accurate diagnoses of tissue pathologies, particularly cancer. This study, then, lays a substantial foundation upon which to build future efforts focusing on the development of specialized nanoshells for tissue imaging and reflectance enhancement. Such efforts include the use of antibody conjugation to specifically target tissue dysplasia, the use of larger sizes of tissue and nanoshell samples, and the design of fiber geometry with respect to specific types of nano-particles and *in vivo* experimentation.

Acknowledgements

Thanks to David Martin for his editorial advice and comments and CHTN for tissue supply. This work is made possible through the contributions of the Beckman Foundation, CBEN, CDMRP, DOD, Hammill Innovation Fund, NIH 5R01CA109385 with Jennifer Barton, and Welch Foundation.

References

- [1] I. Bigio and J. R. Mourant, "Ultraviolet and visible spectroscopies for tissue diagnostics: fluorescence spectroscopy and elastic-scattering spectroscopy," *Phys. Med. Biol.* **42**, 803–814 (1997) [doi:10.1088/0031-9155/42/5/005].
- [2] K. Sokolov, R. Drezek, K. Gossage, and R. Richards-Kortum, "Reflectance spectroscopy with polarized light: is it sensitive to cellular and nuclear morphology," *Opt. Exp.* **5**(13), 302-17 (1999).
- [3] M. Skala, G. Palmer, C. Zhu, Q. Liu, K. Vrotsos, C. Marshek-Stone, A. Gendron-Fitzpatrick, and N. Ramanujam, "Investigation of fiber-optic probe designs for optical spectroscopic diagnosis of epithelial pre-cancers," *Lasers Surg. Med.* **34**, 25–38 (2004) [doi:10.1002/lsm.10239].
- [4] L. Nieman, A. Myakov, J. Aaron, and K. Sokolov, "Optical sectioning using a fiber probe with an angled illumination-collection geometry: evaluation in engineered tissue phantoms," *Appl. Opt.* **43**(6), 1308-19 (2004) [doi:10.1364/AO.43.001308].
- [5] A. Wang, J. Bender, J. Pfefer, U. Utzinger, and R. A. Drezek, "Depth-sensitive reflectance measurements using obliquely oriented fiber probes," *J. Biomed. Opt.* **10**(4), 044017 (2005) [doi:10.1117/1.1989335].

- [6] D. Arifler, R. Schwarz, S. Chang, and R. Richards-Kortum, "Reflectance spectroscopy for diagnosis of epithelial precancer: model-based analysis of fiber-optic probe designs to resolve spectral information from epithelium and stroma," *Appl. Opt.* **44**(20), 4291-305 (2005) [doi:10.1364/AO.44.004291].
- [7] A. Wang, V. Nammalvar, R. Drezek, "Targeting spectral signatures of progressively dysplastic stratified epithelia using angularly-variable fiber geometry in reflectance Monte Carlo simulations," *J. Biomed. Opt.*, Under Review (2007).
- [8] A. Wang, V. Nammalvar, R. Drezek, "Experimental evaluation of angularly-variable fiber geometry for targeting depth-resolved reflectance from layered epithelial tissue phantoms," *J. Biomed. Opt.*, Under Review (2007).
- [9] C. Loo, A. Lowery, N. Halas, J. West & R. Drezek, "Immunotargeted nanoshells for integrated cancer imaging and therapy," *Nano. Lett.* **5**(4), 709–711 (2005) [doi:10.1021/nl050127s].
- [10] C. Loo, L. Hirsch, M. Lee, E. Chang, J. West, N. Halas & R. Drezek, "Gold nanoshell bioconjugates for molecular imaging in living cells," *Opt. Lett.* **30**(9), 1012–1014 (2004) [doi:10.1364/OL.30.001012].
- [11] M. H. Lee, V. Nammalvar, A. Gobin, J. Barton and J. West, "Nanoshells as contrast agents for scatter-based optical imaging," *Biomedical Imaging: Macro to Nano, 2006. 3rd IEEE International Symposium.*, 371-374 (2006) [doi: 10.1109/ISBI.2006.1624930].
- [12] L. R. Hirsch, R. J. Stafford, J. A. Bankson, S. R. Serchen, B. Rivera, R. E. Price, J. D. Hazle, N. J. Halas, J. L. West, "Nanoshell-mediated near-infrared thermal therapy of tumors under magnetic resonance guidance," *PNAS.* **100** (11), 13549. (2003) [doi:10.1073/pnas.2232479100].
- [13] D.P O'Neal, L.R Hirsch, N.J Halas, J.L West "Nanoshell-assisted photothermal ablation of colon carcinoma-derived tumors in mice." *Cancer Lett.* **209**, 171-6 (2004).
- [14] A. Gobin, D. O'Neal, N. Halas, R. Drezek, and J. West, "Near infrared laser tissue welding using nanoshells as an exogenous absorber," *Lasers in Surg. and Med.* **37**, 123-129 (2005) [doi:10.1002/lsm.20206].
- [15] W. Stober, A. Fink and E. Bohn "Controlled growth of nanodisperse silica spheres in the micron size range," *J. Colloid Interface Sci.* **26**, 62-69 (1968) [doi:10.1016/0021-9797(68)90272-5].
- [16] D. G. Duff, A. Baiker, "A new hydrosol of gold clusters,. 1. formation and particle size variation," *Langmuir* **9**, 2301 (1993) [doi:10.1021/la00033a010].
- [17] T. Collier, P. Shen, B. de Pradier, K. B. Sung, R. Richards-Kortum, "Near real time confocal microscopy of amelanotic tissue: dynamics of aceto-whitening enable nuclear segmentation," *Opt. Exp.* **6**(2), 40-48 (2000).
- [18] R. Drezek, R. Richards-Kortum, M. Brewer, M. Feld, C. Pitris, A. Ferenczy, M. Faupel, and M. Follen, "Optical imaging of the cervix," *Second Intl. Conf. Cervical Cancer*, 2015–2027 (2003).
- [19] S. Chang, D. Arifler, R. Drezek, M. Follen, and R. Richards-Kortum, "Analytical model to describe fluorescence spectra of normal and preneoplastic epithelial tissue: comparison with Monte Carlo simulations and clinical measurements," *J. Biomed. Opt.* **9**(3), 511–522 (2004) [doi:10.1117/1.1695559].
- [20] C. Zhu, Q. Liu, and N. Ramanujam, "Effect of fiber optic probe geometry on depth-resolved fluorescence measurements from epithelial tissues: a Monte Carlo simulation," *J. Biomed. Opt.* **8**(2), 237–247 (2003) [doi:10.1117/1.1559058].
- [21] N. McNutt, R. Hershberg, R. Weinstein, "Further observations on the occurrence of nexuses in benign and malignant human cervical epithelium," *J. Cell Biology* **51**, 805-825 (1971) [doi:10.1083/jcb.51.3.805].
- [22] J. Sugar, "An electron microscopic study of early invasive growth in human skin tumors and laryngeal carcinoma," *Eur. J. Cancer* **4**, 33-38 (1968) [doi:10.1016/0014-2964(68)90067-4].

- [23] F. White, K. Gohari, "Alterations in the volume of the intracellular space between epithelial-cells of the hamster cheek-pouch," *J. Oral Pathol. Med.* **13**, 244-54 (1984) [doi:10.1111/j.1600-0714.1984.tb01422.x].

Reflectance spectroscopy of gold nanoshells: computational predictions and experimental measurements

Alex W. H. Lin, Nastassja A. Lewinski, Min-Ho Lee and Rebekah A. Drezek*

Department of Bioengineering, Rice University, MS-142, P.O. Box 1892, Houston, TX, 77251-1892, USA;

**Author for correspondence (Tel.: +1-713-348-3011; Fax: +1-713-348-5877; E-mail: drezek@rice.edu)*

Received 27 February 2006; accepted in revised form 14 June 2006

Key words: nanoshells, nanoparticles, Monte Carlo, contrast agents, reflectance, spectroscopy, modeling and simulation

Abstract

Gold nanoshells are concentric spherical constructs that possess highly desirable optical responses in the near infrared. Gold nanoshells consist of a thin outer gold shell and a silica core and can be used for both diagnostic and therapeutic purposes by tuning the optical response through changing the core-shell ratio as well as the overall size. Although optical properties of gold nanoshells have already been well documented, the reflectance characteristics are not well understood and have not yet been elucidated by experimental measurements. Yet, in order to use gold nanoshells as an optical contrast agent for scattering-based optical methods such as reflectance spectroscopy, it is critical to characterize the reflectance behavior. With this in mind, we used a fiber-optic-based spectrometer to measure diffuse reflectance of gold nanoshell suspensions from 500 nm to 900 nm. Experimental results show that gold nanoshells cause a significant increase in the measured reflectance. Spectral features associated with scattering from large angles ($\sim 180^\circ$) were observed at low nanoshell concentrations. Monte Carlo modeling of gold nanoshells reflectance demonstrated the efficacy of using such methods to predict diffuse reflectance. Our studies suggest that gold nanoshells are an excellent candidate as optical contrast agents and that Monte Carlo methods are a useful tool for optimizing nanoshells best suited for scattering-based optical methods.

Abbreviations: NIR: near infrared; OCT: optical coherence tomography; CCD: charge-coupled device; POI: point of photon insertion; LAS: large angle scattering

Introduction

Presently, diagnostic procedures to detect the presence of cancerous tissue often include painful biopsies, time-consuming histopathological analysis, and conventional imaging techniques that use potentially harmful ionizing radiation. However, utilizing advanced optical technologies, such as those proposed within the scope of this paper, within the spectrum of cancer diagnostics can prove beneficial in several important ways. First, small and subtle changes in optical properties

associated with early cancers are difficult to discern from normal tissue (Drezek et al., 2003), using either the current conventional or optical technologies. Second, advances in optical technologies for cancer diagnostics also promise to improve sensitivity, specificity, and cost effectiveness, as well as bring higher resolution and non-invasive imaging and assessment of tissue over current approaches.

Specifically, scattering-based optical techniques, such as polarized scattering spectroscopy (Sokolov et al., 2004) and optical coherence tomography

(OCT) (Matheny et al., 2004), utilize intrinsic changes, including increased nuclear size and changes in refractive index, to differentiate normal from diseased tissue. These methods have shown considerable promise in overcoming limitations associated with current optical techniques. However, these changes, and many other valuable molecular indicators of early cancers, may not, at the same time, generate obvious intrinsic optical contrast. For this reason, optical contrast agents that can, in fact, enhance the subtle differences between normal and diseased tissue by targeting specific biomolecular markers of interest are most desirable for the early detection of cancer.

Various chemical and particle-based techniques have been investigated for use as contrast agents for optical technologies (Brigger et al. 2002; Licha, 2002; West & Halas, 2003). However, as optical diagnosis of cancer is still a developing field, the use of such agents is not routine. Particle-based technologies have generated much interest for enhancing contrast for optical imaging (Sokolov et al., 2003; Loo et al., 2004a, b) and microscopy (Loo et al., 2004a, b; Wang et al., 2004) due to their unique optical capabilities and ease of adding surface modifications. However, with the advancement in nanotechnology, interest is rapidly growing in developing nanoparticle-based contrast agents to probe for and target molecular signatures of interest. This exciting nexus of nano-bio-opto technologies aims to improve detecting, monitoring and sensing of biomolecules that can potentially achieve earlier and greater accuracy in cancer detection. Molecular-specific contrast agents achieve specific targeting through antibody binding of tumor cell surface molecules or tumor-specific peptides. Antibody targeting has been used extensively to achieve cell-selective targeting by therapeutic and diagnostic agents, and it is especially useful for targeting biomarkers of cancers (Chen et al., 2005; Michalet et al., 2005). To illustrate, Chen et al. (2005) showed OCT image enhancement using gold nanocages and have also targeted breast cancer cells through the process of bioconjugation. Levy et al. (2002) used targeted silica, encapsulating magnetic nanoparticles and fluorescent dyes, to enhance optical imaging and, therefore, the detection and therapy of oral cancer cells. In addition, nanoparticles, such as semiconductor quantum dots, also have highly modifiable surfaces and show similar potential for use as

target-specific probes (Akerman et al., 2002; Wang et al., 2004). Chang et al. (2005), for example, showed the utility of using protease-activated quantum dots to potentially improve bioimaging of protease activity.

In this paper, though, we consider the use of metal nanoshells as an exogenous contrast agent. Metal nanoshells consist of a dielectric core, typically silica, covered with a thin outer metallic shell, usually gold. Gold nanoshells exhibit enhanced scattering and absorption behavior due to the strong plasmon resonance of the metallic-dielectric concentric spherical configuration (Oldenburg et al., 1998). In particular, the optical behavior of gold nanoshells in the near infrared (NIR) wavelengths shows scattering and/or absorption cross sections several times the particle geometric cross section (Oldenburg et al., 1999). This is not seen with comparable particles such as gold colloidal nanoparticles, which show weak optical activity in the NIR spectrum region (Kreibig & Vollmer, 1995). By varying the relative core size and shell thickness, the peak resonance of the gold nanoshells can be systematically varied across a broad range of the optical spectrum that spans the visible and the near infrared spectral regions. In Figure 1, Mie extinction plots are shown with a 50 nm radius silica core and an increasing core radius-to-shell thickness ratio that shifts the peak resonance into the NIR. Gold nanoshells can also be tuned to preferentially absorb or scatter at the same peak optical resonance (Loo et al., 2004a, b). Under current laboratory methods, it is possible to fabricate gold nanoshells of varying sizes with experimental observations of optical attenuation closely matching Mie theory. The fabrication method utilizes a combination of molecular self-assembly and colloid chemistry in aqueous solution.

The strong optical responses of gold nanoshells in the NIR are especially useful for biophotonic applications where medium optical transmissivity peaks. Gold nanoshell surfaces are virtually chemically identical to gold colloid used in numerous bioconjugate applications (Faulk & Taylor, 1971). By functionalizing gold nanoshell surfaces with target-specific antibodies, Loo et al. (2004a, b) showed that visualization of HER2-positive breast cancer cells under brightfield and darkfield microscopy could be enhanced using HER2-targeting gold nanoshells. The targeted cancer cells can then be selectively destroyed via

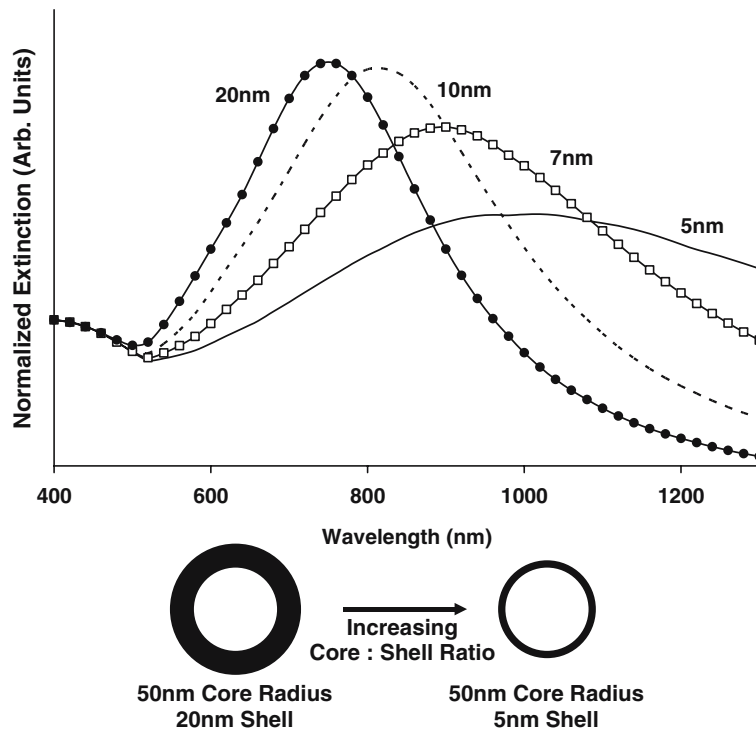


Figure 1. By increasing the core radius-to-shell thickness ratio, the peak extinction resonance can be shifted well into the NIR. Peak resonance shifts to longer wavelengths for gold nanoshells with a core (silica) radius of 50 nm and a decreasing gold shell thickness.

photothermal destruction (Loo et al., 2005). Although gold nanoshells have already shown considerable success in both cancer imaging and therapy, the reported optical properties of nanoshells thus far show only properties in transmission, and experimental measurements have not yet been reported for reflectance. Characterizing nanoshell reflectance is, therefore, a crucial step in understanding how gold nanoshells affect tissue reflectance for scattering-based optical methods. This will, in turn, help in further elucidating the efficacy of gold nanoshells as an optical contrast agent.

Using experimental and computational tools, we evaluated diffuse reflectance behavior of gold nanoshells suspended in water. We first used analytical electromagnetic methods to calculate optical properties of various nanoshells with a variety of scattering and absorbing capabilities. Subsequently, we measured diffuse reflectance of gold nanoshell suspensions of varying concentrations using a fixed geometry fiber-probe-based spectrometer. To investigate the efficacy of using

computational methods to predict reflectance from nanoparticle suspensions, Monte Carlo methods were used to model diffuse reflectance from computer models based on these same gold nanoshell suspensions. It should be further noted that Monte Carlo methods have been widely used to simulate photon propagation through a turbid medium, such as biological tissue (Wang et al., 1995). As such, the use of these methods can also assist in evaluating predictions of macroscopic reflectance behavior of nanoparticles, such as gold nanoshells, in a turbid medium.

Based on our studies, we show that the measured diffuse reflectance from gold nanoshell suspensions can be efficiently modeled with Monte Carlo methods. In general, reflectance is greater with high scattering, low absorption and low anisotropy of nanoshells (greater probability of scattering backwards). Due to the fixed fiber-probe geometry, spectral features related to scattering from large angles ($\sim 180^\circ$) become more noticeable at lower nanoshell concentrations. As a result, scattering from large angles results in higher

measured reflectance and may be a useful feature for detecting the presence of nanoshells at low concentrations. However, at the same time, the accuracy of computational predictions may be limited. The Monte Carlo models cannot account for the rise in detection of photons that are singly scattered at large angles ($\sim 180^\circ$), as the assumption that gold nanoshells gives rise to a homogeneous change in optical properties of the medium, may not be accurate at low concentrations of nanoshells.

Methods

Gold nanoshells have been shown by various investigators to possess unique properties for use as an optical contrast agent and also as a therapeutic agent for cancer diagnosis and treatment (Loo et al., 2005). To non-invasively detect early cancers, using gold nanoshells as a scattering-based optical contrast agent, there is a need to understand how gold nanoshells affect diffuse reflectance.

Optical properties of gold nanoshells

The optical response of gold nanoshells can be described by using computed solutions of Mie theory for concentric spherical shells at the boundaries between different mediums: the gold shell, the silica core, and the embedding medium (Oldenburg et al., 1999). To investigate how optical properties of gold nanoshells affect diffuse reflectance, theoretical optical properties of gold nanoshells were first calculated with excitation wavelengths from 500 nm to 900 nm in water ($n = 1.33$). Using Mie scattering solutions at 180° (opposite direction to the excitation wave direction), the scattering efficiencies were calculated to examine the effect of scattering from large angles on reflectance. To avoid confusion, in this paper, theoretical scattering efficiency from 180° will subsequently be called the Q_{180} scattering efficiency. From Mie Theory, the Q_{180} efficiency is given as

$$Q_{180} = \frac{4}{k^2 r^2} |S_{11}(180^\circ)| \quad (1)$$

where $k = \frac{2\pi n}{\lambda}$, $r = \text{radius}$

The term $S_{11}(180^\circ)$ is the Mie angular scattering component in the direction opposite of the excitation plane wave (van der Hulst, 1981; Bohren and Huffman, 1983). Gold nanoshells of approximately R71/84 (representing a core radius of 71 nm and total radius of 84 nm), R104/127 and R154/178, all showing different optical properties, were selected and used for the Monte Carlo studies and fabricated for spectroscopic measurements.

Gold nanoshell fabrication

Gold nanoshells of a wide range of sizes can, with adequate predictability and reproducibility, be fabricated using current laboratory protocols. First, the silica cores were made by reducing tetraethylorthosilicate (Sigma-Aldrich) in ethanol as outlined by Stober et al. (1968). The average size of the silica core nanoparticles were then determined by scanning electron microscopy, SEM (Philips FEI XL30). The surface of the Stober particles were then functionalized with amine groups using 3-aminopropylethoxysilane (Sigma-Aldrich). To form the outer gold shell, the aminated silica particles were added to concentrated, aged (2 weeks at $\sim 4^\circ\text{C}$) gold colloid that was grown using the method outlined by Duff & Baker (1993). The gold colloid adsorbs onto the aminated surface and forms nucleation sites for the further reduction of gold onto the Stober nanoparticle surface. The gold shell was then grown by reacting HAuCl_4 (Sigma-Aldrich) with the gold-seeded aminated particles in the presence of formaldehyde. The absorbance characteristics of the nanoshells were monitored using a UV-Vis spectrophotometer. The average size and distribution of the gold nanoshells were then measured using the SEM and the standard deviations of the nanoshell sizes were determined to be approximately 5%. The sizes of the nanoshells were then reconfirmed by comparing the UV-VIS measurements and the theoretical Mie extinction at the average size. Gold nanoshells of average sizes approximately R71/84 (representing a core radius of 71 nm and an overall radius of 84 nm), R104/127 and R154/178 were fabricated to encompass a variety of different optical properties. Figure 2 shows a SEM micrograph of the R154/178 gold nanoshell, one of the nanoshells fabricated for the spectroscopy studies. The gold nanoshell suspensions were concentrated to a

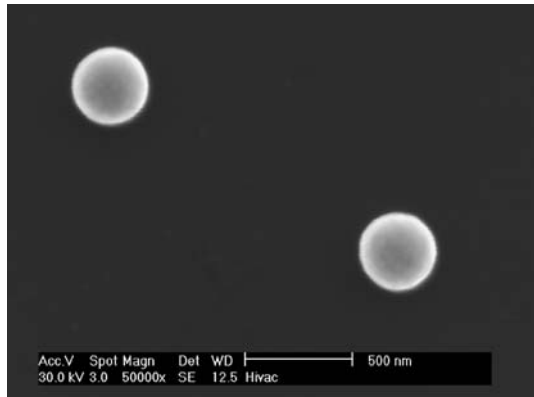


Figure 2. Scanning electron microscope (SEM) image of the R154/178 (representing a core radius of 154 nm and overall radius of 178 nm) nanoshell. The scale bar represents 500 μm .

volume fraction of approximately 0.0002 for spectroscopic measurements.

Diffuse reflectance spectroscopy

Diffuse reflectance measurements of nanoshell suspensions were performed using a fiber-optic-based Ocean Optics HR2000 spectrometer (Ocean Optics, Inc., Dunedin, FL). The instrument consists of a tungsten-halogen broadband light source (DH2000, Ocean Optics, Inc.) and a spectrometer (HR2000, Ocean Optics, Inc.) with a 2048 element charge-coupled device (CCD) (UV2/OFLV-5, Ocean Optics, Inc.). The spectrometer has a slit width of 5 μm with the optical resolution of approximately 0.66 nm. The instrument was set up to collect diffuse reflectance of nanoshell suspensions from 500 nm to 900 nm through a fiber optic reflection probe. The illumination and collection is coupled through a fiber probe consisting of six illumination fibers around one read fiber (R400-ANGLE, Ocean Optics, Inc.). Each fiber is 400 μm in diameter with a numerical aperture of 0.22, and the probe end employs a 30° glass window to eliminate specular reflectance. The charge-coupled device in the spectrometer detects reflected light and presents the intensity as a function of wavelength. A diffuse reflection standard (WS-1, Ocean Optics, Inc.) submerged in water was used as the 100% reflectance reference. The angled probe was placed approximately 0.3 cm above the surface of the reference and the detected reflectance was referenced as 100% reflectance with an

integration time of 700 ms. This process ensures maximum detection of reflected photons without detector saturation. A darkened cuvette with water was used as the base reference (0% reflectance) with the probe immersed and illumination turned on. Suspensions of gold nanoshells were measured with a starting volume fraction (V_f) of ~ 0.0002 and subsequently diluted by 5 \times , 25 \times , and 100 \times . Each suspension was measured using a darkened cuvette with the probe immersed in the nanoshell suspension and the percent diffuse reflectance recorded with an integration time of 700 ms.

Monte Carlo modeling

Photon propagation through a turbid medium, such as biological tissue, can be efficiently modeled using Monte Carlo methods. The method allows investigators to accurately predict how light interacts with tissue without the use of actual biological tissue. Monte Carlo modeling of photon transport by Wang et al. (1995), a computational tool written in Standard C (MCML), has been widely used to simulate the random walk of photons through multilayered turbid media. Scattering and absorption events of photons propagating through a turbid medium can be accurately modeled using this method. Then, as optical parameters, such as scattering and absorption coefficients of the model, are changed, the propagation behavior changes accordingly. In our study, diffuse reflectance from a suspension of nanoshells in water was modeled as a homogenous medium. Following the method shown by Lin et al. (2005), the scattering and absorption cross sections (C) of gold nanoshells can be related to the scattering (μ_{sca}) and absorption coefficients (μ_{abs}) by

$$\mu_{\text{sca,abs}} = N \times C \quad (2)$$

where N is the number of particles per unit volume. The scattering and absorption coefficients can then be used in the Monte Carlo simulations. To simulate the diffuse reflectance from gold nanoshell suspensions, the embedding medium index of refraction was set at $n = 1.33$ (water) and $n = 1.5$ (glass) for the source medium. To efficiently model and study the diffuse reflectance measured from the experimental measurements, we employed the use of a simplified Monte Carlo model to simulate diffuse reflectance from a gold

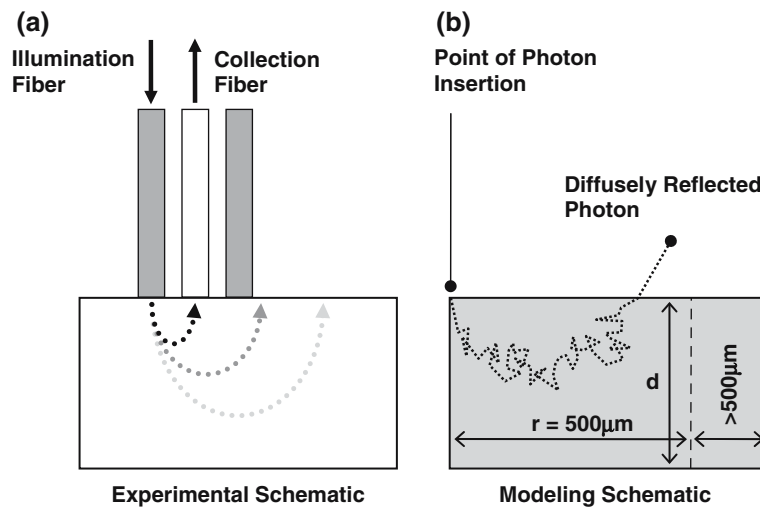


Figure 3. Schematic shows the (a) experimental setup and (b) the simplified model used in the Monte Carlo studies. Schematic (a) shows the use of the 6-illumination around 1-collection fiber optic probe. Gold nanoshell suspensions were modeled as a homogenous bulk semi-infinite layer ($d = 1.0 \times 10^8$ cm) at the point where photons are introduced (POI) into the model at $0 \mu\text{m}$ shown in (b). The distribution of photon reflectance was analyzed up to $r = 500 \mu\text{m}$, and all the photons that were remitted at radii $> 500 \mu\text{m}$ were tallied. The total diffuse reflectance, regardless of the distribution, was used in comparison to the experimental results.

nanoshell suspension. Figure 3 shows the experimental (Figure 3(a)) and modeling (Figure 3(b)) schematic, where the collection geometry of the fiber optic probe used in the experimental measurements was simplified and the modeled diffuse reflectance is collected regardless of where the photon is remitted. The modeled diffuse reflectance will be compared to the experimental measurements, followed by an analysis of the radial distribution of the modeled photon reflectance. The scattering and absorption coefficients of the gold nanoshells at the average size of R71/84, R104/127 and R154/178 were calculated with volume fractions of 0.0002 ($1\times$), 4×10^{-5} ($5\times$), 8×10^{-6} ($25\times$), and 2×10^{-6} ($100\times$). In this calculation and subsequent use in the Monte Carlo simulations, the size distributions of the fabricated gold nanoshells were neglected and only the average size was considered. The optical properties of water were not considered in the final optical properties of the model because the experimental setup eliminates optical attenuation due to water. The nanoshell suspension was modeled as a semi-infinite homogenous (depth (d) = 1.0×10^8 cm) layer. As the nanoshell suspensions are diluted, the optical coefficients decrease proportionately as demonstrated by Eq. (2). The MCML method

assumes that the angular scattering pattern of the turbid media follows the Henyey–Greenstein approximation (Henyey & Greenstein, 1941). It is also important that the angular scattering pattern of gold nanoshells can be approximated to the Henyey–Greenstein scattering pattern. Figure 4 shows the comparison between the actual angular scattering pattern and the scattering pattern approximated by Henyey–Greenstein. The graphs in Figure 4 show the scattering patterns of the R104/127 nanoshell at 630 nm (Figure 4(a)) and at 830 nm (Figure 4(b)). While there are small differences, gold nanoshell angular scattering is adequately estimated by the Henyey–Greenstein approximation.

Results

Figures 5 through 7 show the computational and experimental results of the R104/127, R71/84 and R154/178 nanoshells, respectively. To avoid confusion, features from the measured reflectance spectra related to photon scattering from large angles ($\sim 180^\circ$) will hereinafter be referred to as Large Angle Scattering (LAS). Graphs (a) and (b) in Figures 5–7 show the theoretical nanoshell

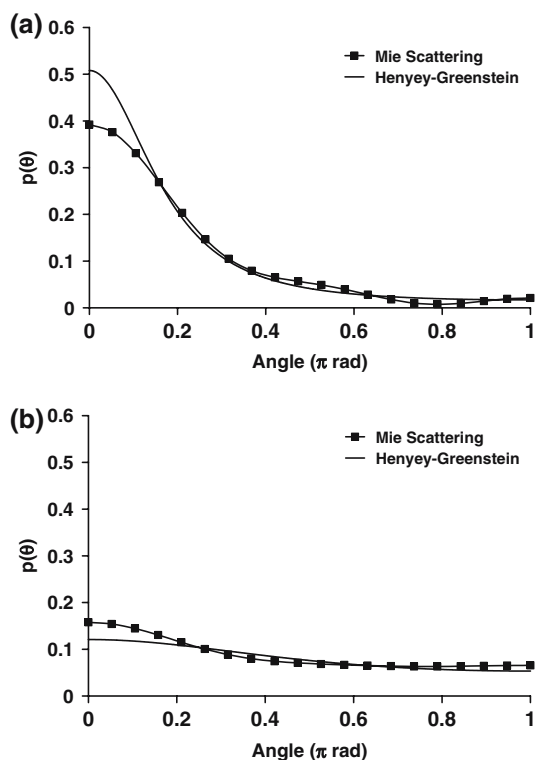


Figure 4. Graphs shows the angular scattering patterns of the R104/127 gold nanoshell at (a) 630 nm and (b) 830 nm. The graphs show that the theoretical Mie scattering patterns is adequately estimation by the Henyey–Greenstein phase scattering approximation, and thus appropriately modeled in Monte Carlo.

optical properties calculated from Mie theory. Figures 5(a), 6(a) and 7(a) show the scattering, absorption, extinction and 180-Scattering (van der Hulst, 1981 (efficiencies as a function of wavelength and Figures 5(b), 6(b) and 7(b) shows the anisotropy parameter (g value) as a function of wavelength. Spectroscopy measurements of gold nanoshell suspensions diluted from $1\times$ to $100\times$ are shown in Figures 5(c), 6(c) and 7(c). The Monte Carlo simulation results for each nanoshell are shown in Figures 5(d), 6(d) and 7(d). To further analyze the modeling results, Figure 8 shows the percent reflectance as a function of the collection radius at 700 nm over the first 500 μm radius of the R71/84 nanoshell suspension model. In the graph (Figure 8), 0 μm represents the point of photon packet introduction (POI), and the x -axis (radius) is the distance from POI at which the

reflectance is recorded. It is important to note that the total reflectance remains the same for the different dilutions modeled (Figure 6(d)). Each data point in Figure 8 represents the modeled reflectance accumulated from each 50 μm interval and is represented at the midpoint. The insert in Figure 8, shows the accumulated modeled reflectance collected over the first 500 μm radius as a percentage of the modeled total diffuse reflectance that was collected regardless of radial distribution. Figure 9 shows the accumulated diffuse reflectance collected from a radius of $> 500 \mu\text{m}$, with respect to volume fraction of the R71/84 gold nanoshell.

Discussion

Diffuse reflectance spectroscopy

Scattering and absorption

From the results shown in Figures 5–7, a marked change in diffuse reflectance was observed, particularly for longer wavelengths in all the nanoshells used in our studies. From these results, nanoshells that exhibit high scattering, with low absorption and low anisotropy, generally exhibit substantial changes in measured diffuse reflectance. In general, then, we can say that higher scattering and lower absorption efficiencies will result in higher measured reflectance. However, it should be added that this generalization is complicated by the changing anisotropy factor across the spectral range, which is explained below.

Anisotropy parameter (g)

The anisotropy parameter, g , a dimensionless number, is a measure of the photon travel direction retained after a single scattering event and is the expectation value for average $\cos(\theta)$ shown in Figures 5(b), 6(b) and 7(b). The value of g ranges from -1 to 1 , with a positive value indicating the preference for forward scattering and a negative value for backward scattering. A value of 0 indicates isotropic scattering and equal probability of scattering in all directions. The nanoshells used in our studies have anisotropy values that change with wavelength. This results in photons that are more backward scattering and, hence, the phenomenon contributes to the overall measured reflectance. As shown in Figures 5(c), 6(c) and 7(c), at $V_f = 0.0002$, the R71/84 nanoshell shows

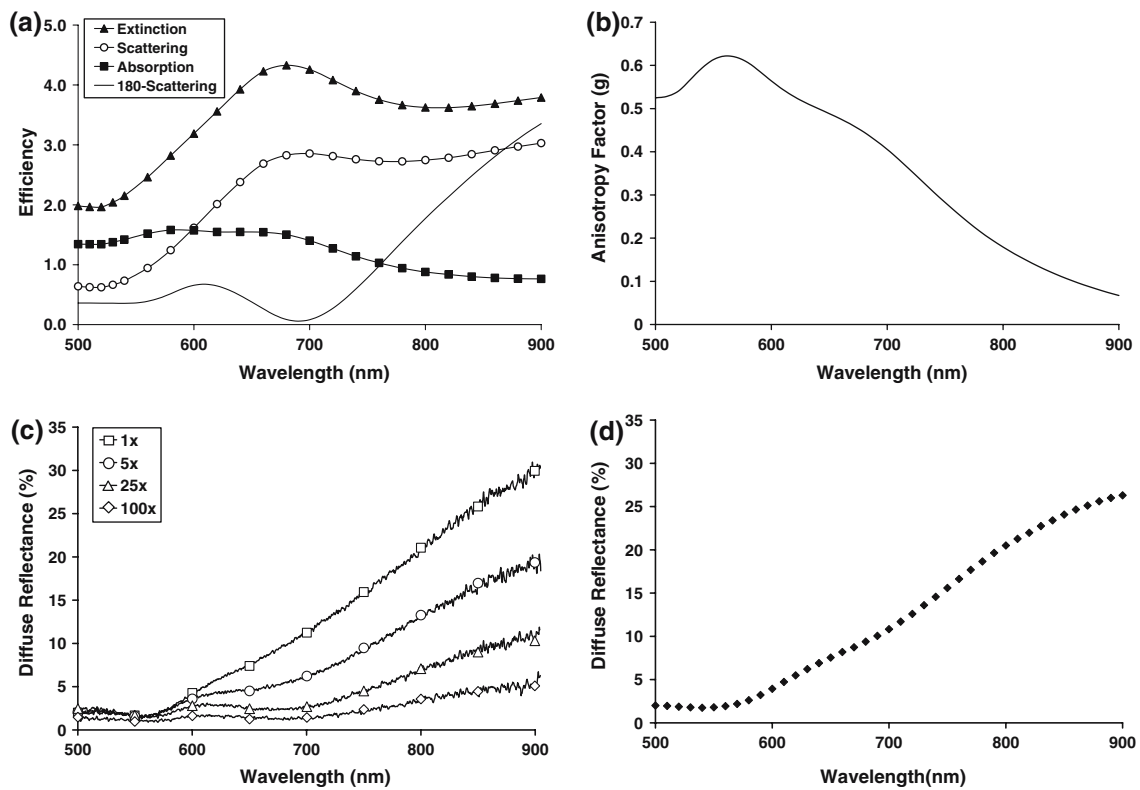


Figure 5. Graphs show computational and experimental results from the R104/127 nanoshell. Graph (a) shows the scattering, absorption, extinction, and 180-Scattering (Scattering from 180°) properties calculated from Mie Theory. From Mie calculations, we can also obtain the anisotropy parameter (g) shown in graph (b). Diffuse reflectance spectroscopy experiments of diluting gold nanoshell suspensions are shown in graph (c). Diluting the suspension by 5 \times , 25 \times and 100 \times shows decreasing detected reflectance. Using Monte Carlo computational methods, diffuse reflectance of the R104/127 nanoshell suspended in water is simulated. Results only show one representative line, while the total reflectance of diluting a suspension remains the same.

a diffuse reflectance of approximately 15% within the 800 nm to 900 nm wavelength region, while the R154/178 nanoshell also shows reflectance approximately 15% within the same wavelength region. This occurs despite that the R154/178 nanoshell shows higher scattering efficiencies and lower absorption efficiencies compared to the R71/84 nanoshell. This discrepancy is likely a result of the lower anisotropy values at 800 nm to 900 nm of the R71/84 nanoshell as compared to the R154/178 nanoshell.

Large angle scattering (LAS)

As nanoshell suspensions are diluted, the inter-particle distance between nanoshell particles increases causing the number of detectable LAS photons to increase. As the particles are farther

apart, photons scattered from large angles ($\sim 180^\circ$) are more likely to travel directly to the collection fiber without interacting with any other particle. This gives rise to spectral features that are more obvious at lower nanoshell concentrations. These features observed at lower concentrations can be related to the Q_{180} scattering efficiencies (Mie scattering solution at 180°) of nanoshells shown in Figures 5(a), 6(a) and 7(a) and which can be representative of photons scattered at approximately 180° . The R104/127 nanoshell shows a small reflectance peak at approximately 610 nm that is more noticeable at dilutions greater than 25 \times (Figure 5(c)), and this peak is seen in the 180-Scattering efficiencies shown in Figure 5(a). Similarly, the R154/178 nanoshell shows two peaks, one at ~ 590 nm and another at ~ 730 nm,

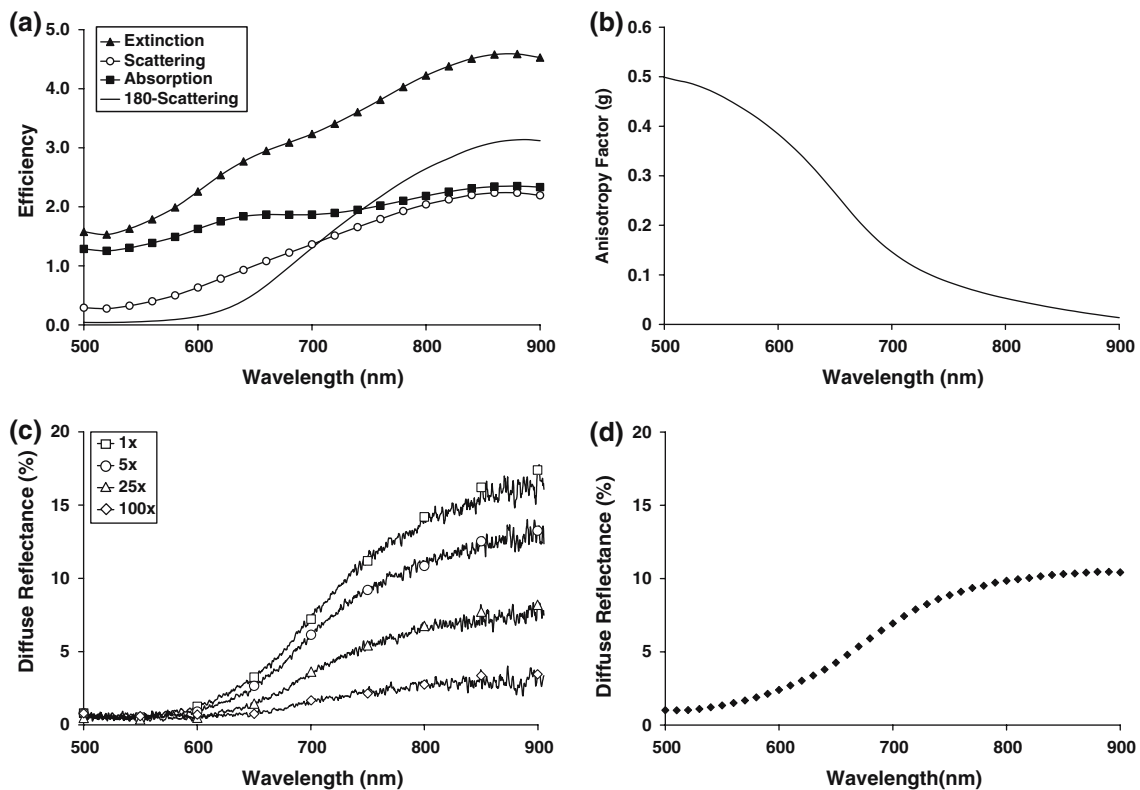


Figure 6. Graphs show computational and experimental results from the R71/84 nanoshell. See description for Figure 3.

where the peak at ~ 710 nm was only observed at dilutions greater than $5\times$ (Figure 7(c)). The peak at ~ 710 nm corresponds to the peak seen in the 180-Scattering efficiency shown in Figure 7(a).

Monte Carlo modeling

In the graphs shown in Figures 5(d), 6(d) and 7(d), the modeling results are shown for each nanoshell. The graphs show the total diffusely reflected photons collected regardless of the radial distribution; and the diffuse reflectance from different concentrations of nanoshell suspensions remains the same, and only a single line is shown in the results. Diffuse reflectance of a model generally remains the same if the μ_s -to- μ_a ratio (with other parameters constant) remains the constant. However, the experimental results show that the detected diffuse reflectance decreases as the concentration of the nanoshell suspension is lowered. In general, the modeling results correspond to the measured spectra at high concentrations, with

variations due to both the influence of LAS and the variation in nanoshell size distribution from the fabrication process. Then, as the suspension concentration is lowered, the detected reflectance signal appears to show an increase in photons that were scattered from large angles ($\sim 180^\circ$). To investigate how decreasing nanoshell concentration affects the reflectance signal collected, we first analyzed the radial distribution of the measured diffuse reflectance up to $500 \mu\text{m}$ from the POI (see Figures 3 and 8). From Figure 8, the $1\times$ suspension shows the greatest change in reflectance over the first $200 \mu\text{m}$ radius, and at lower concentrations, while the reflectance remains low and more evenly distributed through $500 \mu\text{m}$. To further analyze photon distribution, Figure 9 shows the accumulated diffuse reflectance of all reflected photons at any distance greater than $500 \mu\text{m}$ as a function of the volume fraction (R71/84). The most dilute nanoshell suspensions show the highest accumulated diffuse reflectance for distances $> 500 \mu\text{m}$. With decreasing volume fraction, a

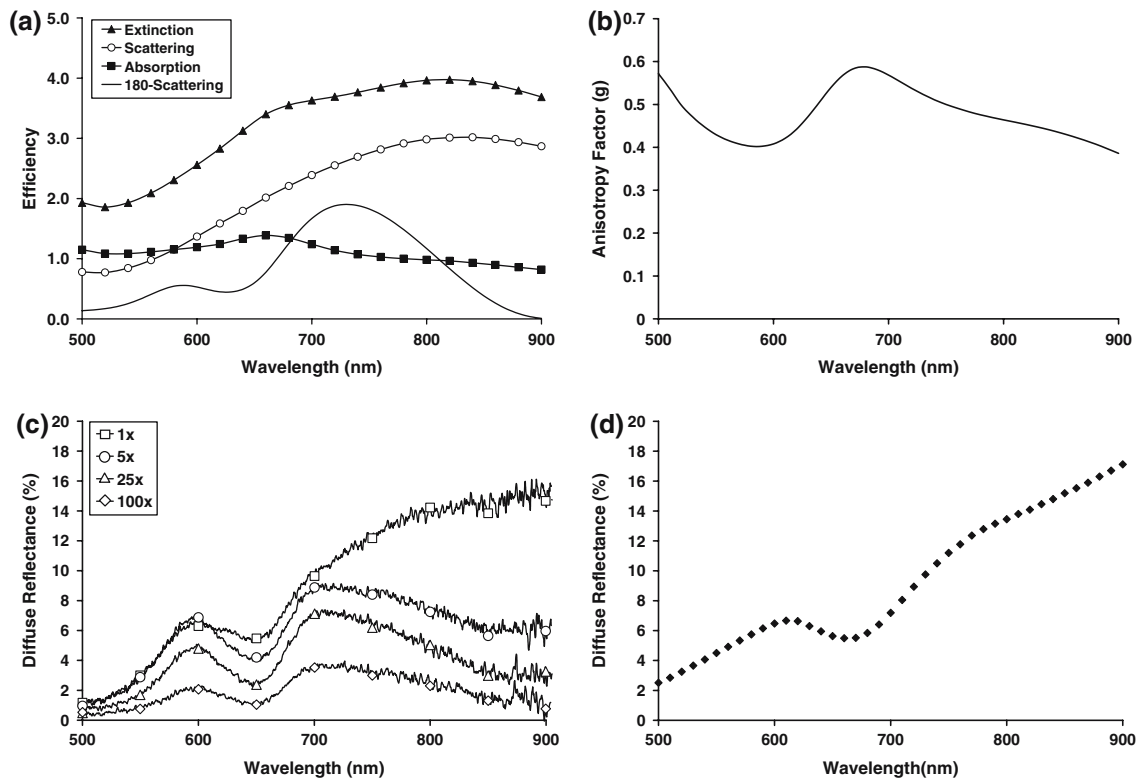


Figure 7. Graphs show computational and experimental results from the R154/178 nanoshell. See description for Figure 3.

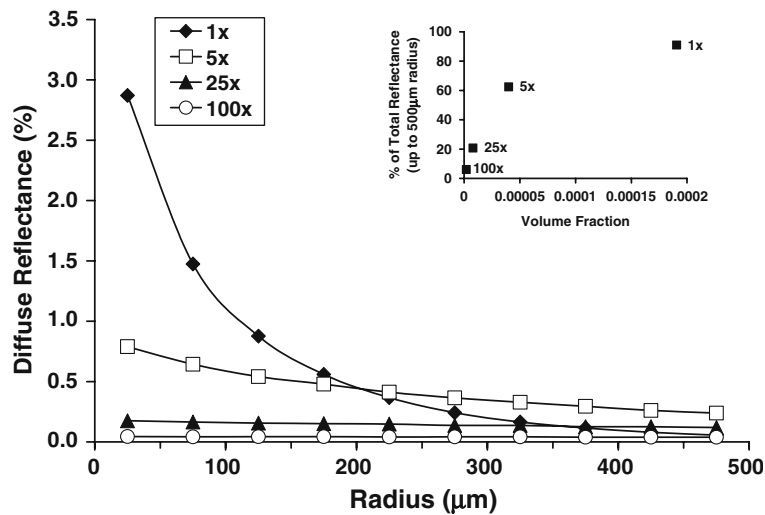


Figure 8. Using the results from the Monte Carlo computations, the distribution of photons across the collection radius is analyzed. The graph shows the accumulated reflectance, at 50 μm intervals up to 500 μm , of the R71/84 nanoshell dilutions at 700 nm excitation wavelength and where 0 μm represents the point where photon packets are introduced. It is important to remember that, regardless of distribution, the total reflectance remains the same for the dilutions of the same nanoshell suspension. The insert shows the accumulated reflectance of photons from radial distances less than 500 μm as a percentage of the total modeled reflectance. At 1 \times concentration, this is almost 100%, and therefore the modeled reflectance (Figures 5(d), 6(d) and 7(d) corresponds to experimental measurements of highly concentrated gold nanoshell suspensions.

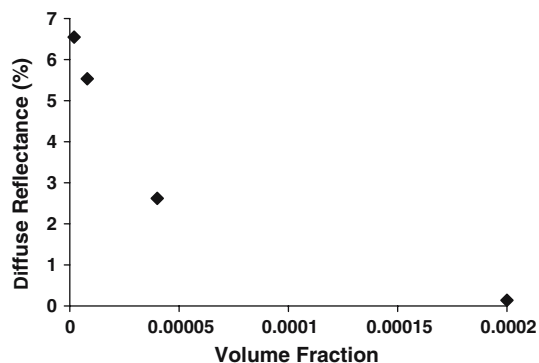


Figure 9. Graph shows that a greater proportion of photons is reflected farther away from the source when all the photons remitted at $> 500 \mu\text{m}$ for the R71/84 nanoshell are accumulated. As the volume fraction of nanoshells decreases, a greater number of photons are remitted $> 500 \mu\text{m}$.

greater proportion of photons are remitted further away from the POI ($> 500 \mu\text{m}$); at the same time, as the extinction coefficient decreases, an increasing effective photon pathlength results. In order to understand why the experimental results correspond more closely to the modeled total reflectance at higher nanoshell concentrations, we analyzed the distribution of the photon reflectance. From the insert shown in Figure 8, the modeled diffuse reflectance collected from a radial distance less than $500 \mu\text{m}$ from the POI of the $1\times$ nanoshell suspension is almost 100% of the total reflectance, whereas, the $100\times$ suspension shows only about 6% of the total modeled reflectance. From the modeling results, we can infer that, in the experimental measurements, the fiber optic probe (diameter of collection fiber = $400 \mu\text{m}$) detect most of the diffusely reflected photons from a highly concentrated suspension of gold nanoshells.

In summary, when the results from the modeling and spectroscopy studies are compared, the experimental observation demonstrates that decreasing nanoshell concentrations appear to decrease the measured diffuse reflectance. Analysis of the photon distribution of the Monte Carlo models suggests that the experimental observations of decreasing diffuse reflectance are due, in fact, to the fixed fiber-probe geometry. In the spectroscopy measurements, the source-detector separation distance (distance between the source

fiber and the collection fiber) of the probe is constant and can only collect photons up to a fixed distance. When the nanoshell volume fraction is lowered, the fiber-probe detects decreasing diffuse reflectance, where a greater proportion of reflected photons is not detected at all by the probe.

Conclusions

The unique, tunable and strong optical responses of gold nanoshells, particularly in the NIR, are most desirable for biophotonics applications. Gold nanoshell optical properties have already been widely reported and are typically shown in transmission. In this paper, we show both experimental and modeling analysis of gold nanoshell reflectance. As gold nanoshell reflectance has not yet been investigated, it is important to understand how tissue reflectance will be altered when used in conjunction with scattering-based spectroscopic methods for the detection of cancers targeted by gold nanoshells. From our studies, we show that gold nanoshells with high scattering efficiencies and low anisotropy parameter values (g) of nanoshells are ideal for producing a significant increase in diffuse reflectance. The high scattering efficiencies at 180 degrees (Q_{180}) were observed to significantly alter scattering signatures, especially at lower concentrations. This important property has already been shown to improve contrast for scattering-based imaging with OCT (Barton et al., 2004; Agrawal et al., 2006). From the Monte Carlo studies, gold nanoshell reflectance can be accurately modeled as a homogenous medium and may be useful for modeling reflectance of tissue with embedded gold nanoshells. In this paper, we have also shown that gold nanoshells are an excellent candidate as an optical contrast agent for altering scattering signatures for scattering-based diagnostic modalities. Furthermore, the modeling method can be used to obtain optimized nanoshells best suited for scattering-based optical technologies.

Acknowledgements

We would like to acknowledge the following funding agencies for their generous support: National Science Foundation (BES 022-1544 and

EEC-0118007); DOD CDRMP DAMD17-03-1-0384; the Welch Foundation, and the Beckman Foundation.

References

- Agrawal A., S. Huang, A. Lin, M.-H. Lee, J. Barton, R. Drezek & T. Pfefer, 2006. *J. Biomed. Opt.* (in press).
- Akerman M.E., W.C.W. Chan, P. Laakkonen, S.N. Bhatia & E. Ruoslahti, 2002. Nanocrystal targeting *in vivo*. *PNAS* 99, 12617–12621.
- Barton J.K., N.J. Halas, J.L. West & R.A. Drezek, 2004. Nanoshells as an optical coherence tomography contrast agent. *Proc. SPIE Int. Soc. Opt. Eng.* 5316, 99–106.
- Brigger I., C. Dubernet & P. Couvreur, 2002. Nanoparticles in cancer therapy and diagnosis. *Adv. Drug Delivery Rev.* 54, 631–651.
- Bohren C.F. & D.R. Huffman, 1983. *Absorption and Scattering of Light by Small Particles*. New York: John Wiley and Sons.
- Chang E., J.S. Miller, J. Sun, W.W. Yu, V.L. Colvin, R. Drezek & J.L. West, 2005. Protease-Activated quantum dot probes. *Biochem. Biophys. Res. Commun.* 334, 1317–1321.
- Chen J., F. Saeki, B.J. Wiley, H. Cang, M.J. Cobb, Z.-Y. Li, L. Au, H. Zhang, M.B. Kimmey, X. Li & Y. Xia, 2005. Bioconjugated gold nanocages and evaluation of their potential for optical imaging and thermal therapeutic applications. *Nano. Lett.* 5, 473–477.
- Drezek R., T. Collier, C. MacAulay, M. Follen & R. Richards-Kortum, 2003. Light scattering from cervical cells throughout neoplastic progression: influence of nuclear size, DNA content, and chromatin texture. *J. Biomed. Opt.* 8, 7–16.
- Duff D.G., A. Baker & P.P. Edwards, 1993. A new hydrosol of gold clusters. 1. Formation and particle size variation. *Langmuir* 9, 2301–2309.
- Faulk W.T. & G. Taylor, 1971. An immunocolloid method for the electron microscope. *Immunochemistry* 8(11), 1081–1083.
- Heney L. & J. Greenstein, 1941. Diffuse radiation in the galaxy. *Astrophys. J.* 93, 70–83.
- Kreibig U. & M. Vollmer, 1995. *Optical Properties of Metal Clusters*. Berlin: Springer-Verlag.
- Levy L., Y. Sahoo, K.-S. Kim, E.J. Bergey & P.N. Prasad, 2002. Nanochemistry: Synthesis and characterization of multifunctional nanoclinics for biological applications. *Chem. Mater.* 14, 3715–3721.
- Licha K., 2002. Contrast Agents for Optical Imaging. *Topics Curr. Chem.* 222, 1–29.
- Lin A.W.H., N.A. Lewinski, J.L. West, N.J. Halas & R.A. Drezek, 2005. Optically tunable nanoparticle contrast agents for early cancer detection: A model-based analysis of gold nanoshells. *J. Biomed. Opt.* 10, 064035.
- Loo C., L. Hirsch, M. Lee, E. Chang, J. West, N. Halas & R. Drezek, 2004. Gold nanoshell bioconjugates for molecular imaging in living cells. *Opt. Lett.* 30(9), 1012–1014.
- Loo C., A. Lin, L. Hirsch, M. Lee, J. Barton, N. Halas, J. West & R. Drezek, 2004. Nanoshell-enabled photonics-based imaging and therapy of cancer. *Technol. Cancer Res. Treat.* 3(1), 33–40.
- Loo C., A. Lowery, N. Halas, J. West & R. Drezek, 2005. Immunotargeted nanoshells for integrated cancer imaging and therapy. *Nano. Lett.* 5(4), 709–711.
- Matheny E.S., N.M. Hanna, W.G. Jung, Z. Chen, P. Wilder-Smith, R. Mina-Araghi & M. Brenner, 2004. Optical coherence tomography of malignancy in hamster cheek pouches. *J. Biomed. Opt.* 9(5), 978–981.
- Michalet X., F.F. Pinaud, L.A. Bentolila, J.M. Tsay, S. Doose, J.J. Li, G. Sundaresan, A.M. Wu, S.S. Gambhir & S. Weiss, 2005. Quantum dots for live cells, *in vivo* imaging, and diagnostics. *Science* 307(5709), 538–549.
- Oldenburg S.J., R.D. Averitt, S.L. Westcott & N.J. Halas, 1998. Nanoengineering of optical resonance. *Chem. Phys. Lett.* 288, 243–247.
- Oldenburg S.J., J.B. Jackson, S.L. Westcott & N.J. Halas, 1999. Infrared extinction properties of gold nanoshells. *Appl. Phys. Lett.* 75(19), 2897–2899.
- Sokolov K., M. Follen, J. Aaron, I. Pavlova, A. Malpica, R. Lotan & R. Richards-Kortum, 2003. Real-time vital optical imaging of precancer using anti-epidermal growth factor receptor antibodies conjugated to gold nanoparticles. *Cancer Res.* 63, 1999–2004.
- Sokolov K., L.T. Nieman, A. Myakov & A. Gillenwater, 2004. Polarized reflectance spectroscopy for pre-cancer detection. *Technol. Cancer Res. Treat.* 3(1), 1–14.
- Stober W., A. Fink & E. Bohn, 1968. Controlled growth of monodisperse silica spheres in the micron size range. *J. Colloid Interface Sci.* 26, 62–69.
- Wang D., J. He, N. Rosenzweig & Z. Rosenzweig, 2004. Superparamagnetic Fe₂O₃ beads-CdSe/ZnS quantum dots core-shell nanocomposite particles for cell separation. *Nano. Lett.* 4(3), 409–413.
- Wang L.H., S.L. Jacques & L.Q. Zheng, 1995. MCML- Monte Carlo modeling of photon transport in multi-layered tissues. *Comput. Meth. Programs Biomed.* 47, 131–146.
- West J.L. & N.J. Halas, 2003. Engineered Nanomaterials for Biophotonics Applications: Improving sensing, imaging, and therapeutics. *Annu. Rev. Biomed. Eng.* 5, 285–292.
- van der Hulst H.C., 1981 *Light Scattering by Small Particles*. New York: Dover Press.

Applications of nanoparticles to diagnostics and therapeutics in colorectal cancer

Paolo Fortina^{1,2}, Larry J Kricka³, David J Graves⁴, Jason Park³, Terry Hyslop^{5,6,7}, Felicia Tam⁸, Naomi Halas⁹, Saul Surrey¹⁰ and Scott A. Waldman^{6,7}

¹ Department of Cancer Biology, Kimmel Cancer Center, Thomas Jefferson University, Jefferson Medical College, Philadelphia, PA 19107, USA

² Dipartimento di Medicina Sperimentale, Università La Sapienza, 00185, Roma, Italy

³ Department of Pathology and Laboratory Medicine, University of Pennsylvania Medical Center, Philadelphia, PA 19104, USA

⁴ Department of Chemical and Biomolecular Engineering, University of Pennsylvania School of Engineering and Applied Science, Philadelphia, PA 19104, USA

⁵ Division of Biostatistics, Thomas Jefferson University, Jefferson Medical College, Philadelphia, PA 19107, USA

⁶ Division of Clinical Pharmacology, Thomas Jefferson University, Jefferson Medical College, Philadelphia, PA 19107, USA

⁷ Department of Pharmacology and Experimental Therapeutics, Thomas Jefferson University, Jefferson Medical College, Philadelphia, PA 19107, USA

⁸ Department of Physics and Astronomy, Rice University, Houston, TX 77005, USA

⁹ Department of Electrical and Computer Engineering, Rice University, Houston, TX 77005, USA

¹⁰ Cardeza Foundation for Hematologic Research, Department of Medicine, Thomas Jefferson University, Jefferson Medical College, Philadelphia, PA 19107, USA

Nanotechnology has considerable promise for the detection, staging and treatment of cancer. Here, we outline one such promising application: the use of nanostructures with surface-bound ligands for the targeted delivery and ablation of colorectal cancer (CRC), the third most common malignancy and the second most common cause of cancer-related mortality in the US. Normal colonic epithelial cells as well as primary CRC and metastatic tumors all express a unique surface-bound guanylyl cyclase C (GCC), which binds the diarrheagenic bacterial heat-stable peptide enterotoxin ST. This makes GCC a potential target for metastatic tumor ablation using ST-bound nanoparticles in combination with thermal ablation with near-infrared or radiofrequency energy absorption. Furthermore, the incorporation of iron or iron oxide into such structures would provide advantages for magnetic resonance imaging (MRI). Although the scenarios outlined in this article are hypothetical, they might stimulate ideas about how other cancers could be attacked using nanotechnology.

Introduction

Colorectal cancer is the third most common neoplasm and the second leading cause of cancer-related mortality in the US (Table 1) [1]. Surgery continues to have a major role in colorectal cancer survival in early-stage disease, by removing detectable tumor; however, residual micrometastases might cause a relapse [2]. Recurrence rates vary from 3% for disease limited to the mucosa (stage I) to >50% for tumors that have spread to regional lymph nodes (stage III). Overall, ~50% of surgically treated patients suffer

from a relapse, with 30% recurring locally or regionally and 70% recurring at distant sites – primarily the liver and lung [3]. There is an unmet clinical need for image-based detection, targeted delivery, and ablation of metastases, to affect survival in this disease. In this context, guanylyl cyclase C (GCC), the intestinal receptor for bacterial diarrheagenic heat-stable enterotoxins (STs), which is selectively expressed in the apical membranes of intestinal mucosa cells in normal adults and in colon cancer cells, might be the ‘magic bullet’ for targeted ablation of colorectal cancer micrometastases [4–6].

Here, we present GCC as a receptor target in colorectal cancer, discuss diagnostics using nanostructures, and address *in vivo* imaging using iron oxide nanoparticles and near-infrared (NIR) fluorescence imaging – approaches that could be extended to other tumor types that have unique receptor functionalities. Novel therapeutic approaches based on functionalized nanoshells and iron-oxide nanoparticles for NIR and radio frequency (RF)-mediated thermal ablation, respectively, of micrometastases as well as nanostructure-based drug delivery are also evaluated. Regulatory issues related to use of nanostructures are not addressed here and have been reviewed previously [7,8].

Nanotechnology

In the past five years, the applications of nanotechnology have been realized in clinical laboratory analysis, imaging and therapeutics [9–16]. The versatility and broad applicability of nanotechnology reflect the spectra of composite materials (e.g. metals, semiconductors or polymers), geometries (e.g. sphere, prism or rod), and structures (e.g. solid, core or shell or dendrimers) that have been generated. This rapidly increasing activity is due to several

Corresponding author: Fortina, P. (paolo.fortina@jefferson.edu). Available online 21 February 2007.

Table 1. Causes of cancer and cancer-related mortality by site

	ESTIMATED US CANCER CASES ^a		
	Men	Women	
New cancers anticipated	720 280	679 510	
Prostate	33%	31%	Breast
Lung and bronchus	13%	12%	Lung and bronchus
Colon and rectum	10%	11%	Colon and rectum
Urinary bladder	6%	6%	Uterine corpus
Melanoma of skin	5%	4%	Melanoma of skin
Non-Hodgkin's lymphoma	4%	4%	Non-Hodgkin's lymphoma
Kidney	3%	3%	Thyroid
Oral cavity	3%	3%	Ovary
Leukemia	3%	2%	Urinary bladder
Pancreas	2%	2%	Pancreas
All other sites	18%	22%	All other sites
	ESTIMATED US CANCER DEATHS		
	Men	Women	
Lung and bronchus	31%	26%	Lung and bronchus
Colon and rectum	10%	15%	Breast
Prostate	9%	10%	Colon and rectum
Pancreas	6%	6%	Pancreas
Leukemia	4%	6%	Ovary
Liver and bile duct	4%	4%	Leukemia
Esophagus	4%	3%	Non-Hodgkin's lymphoma
Non-Hodgkin's lymphoma	3%	3%	Uterine corpus
Urinary bladder	3%	2%	Multiple myeloma
Kidney	3%	2%	Brain/ONS
All other sites	23%	23%	All other sites

^aExcludes basal and squamous cell skin cancers and *in situ* carcinoma except urinary bladder. Abbreviation: ONS, other nervous system. Source: American Cancer Society, 2006 (http://www.cancer.org/docroot/PRO/content/PRO_1_1_Cancer_Statistics_2006_Presentation.asp)

factors, including: i) the discovery of new forms of matter, such as buckminsterfullerenes (buckyballs) and nanotubes made of carbon [17,18]; ii) the increasing ability of materials scientists to produce reagents on a small but controlled size scale; iii) the availability of instruments, such as the atomic force microscope and the scanning tunneling microscope, to complement traditional instrumentation for viewing and characterizing nanoparticles [19]; iv) the discovery of quantum effects, such as size-dependent fluorescent emission in small particles; and v) the stimulation provided by new funding initiatives from worldwide government agencies (<http://nano.cancer.gov/>).

Nano-sized structures range from 1–100 nm – for comparative purposes, a single turn of the DNA helix is ~3.4 nm in length, and a eukaryotic cell has dimensions in the range 10–100 μm. Nanoparticles have been used in biology and medicine for >50 years [20]. In earlier times, they were generally called colloids, emulsions or aerosols, and included many natural and man-made suspensions. Colloidal radioactive gold or gold salts were used as therapeutic agents for intra-articular injection in patients with rheumatoid arthritis – a practice that continues in the current clinical management of this disease – and for treating cancer in the 1950s [21], and colloidal gold or gold granules were used as electron-opaque labels in electron microscopy in the 1960s.

Some of the newer techniques for producing nanoparticles involve: i) cooling them from a hot gas or plasma; ii) reacting a gaseous mixture at a hot surface; iii) designing a system with defined properties so it forms a geometrically precise multi-phase structure as it solidifies; and iv) forming by self-assembly, in which components are designed so that intermolecular forces cause them to come together in a pre-

determined fashion. Multi-step procedures can be used to produce sophisticated core and shell structures that can be further engineered to have highly controlled and ‘tunable’ properties. These include paramagnetic nanoparticles, which can serve as contrast agents for the MRI of tumors [22–24], and nanoshells, which can be fabricated with defined metal shell thicknesses to absorb specific wavelengths of NIR light, resulting in their plasmon resonance and transfer of thermal energy to the surrounding environment [25,26]. In this latter example, NIR wavelengths have minimal optical absorption and, consequently, optimum penetration in tissues, resulting in minimal thermal injury to structures that lack the nanoparticles.

Furthermore, nanostructures can be conjugated to biological molecules, including hormones and antibodies, which enables their targeting to tissues expressing their cognate receptors [27–29]. For example, fluorescent quantum dots conjugated to various peptides specifically target either the vasculature of normal tissues or, alternatively, of cancer cells [30]. Tumor-specific monoclonal antibodies can be conjugated to nanostructures. Monoclonal antibodies directed against a prostate-specific membrane antigen (PSMA) were attached to the surface of triblock copolymer-modified quantum dots and used to image prostate cancer cells, both *in vitro* and *in vivo*, in tumor xenografts [31]. Indeed, anti-PSMA quantum dots injected IV and visualized fluorescently by macro-illumination accumulate in and are retained by prostate cancer xenografts in nude mice.

Nanoshells

Nanoparticles composed of metallic shells with dielectric cores have a tunable plasmon resonance based on the

relative dimensions of the dielectric core and metallic shell [23–26]. Nanoshells composed of metallic gold coating a dielectric core, such as silica, resonate at specific wavelengths of light ranging from 500 nm to 2 μm , depending on their core:shell thickness ratio. Indeed, gold shells of 10 nm encasing a 110 nm silica core resonate in the NIR spectrum (~ 800 nm); these wavelengths exhibit minimal optical absorption by, and consequently optimum penetration through, overlying tissues, with minimal attendant thermal injury (Figure 1). In the context of specifically absorbing energy in the NIR spectrum, these nanoshells are extremely efficient in converting optical energy into heat. When exposed to NIR light, nanoshells with a 10 nm gold shell and a 110 nm silica core induce thermal damage in adjacent cells [25]. Similarly, direct injection of nanoshells into subcutaneous tumors in a mouse xenograft model resulted in temperature increases of $\sim 37^\circ\text{C}$ greater than the surrounding normal tissue after ~ 6 min of exposure to 808 nm at 4 Watts/cm², associated with thermal damage to tumors [26]. Separately, nanoshells injected IV into mice with subcutaneous tumors resulted in NIR heating of tumors compared with non-tumor sites and control animals; most probably, this damage resulted from the enhanced permeability of, and retention by, the tumor neovasculature compared with the established vasculature in normal tissues [26]. Differential heating was associated with complete regression of subcutaneous tumor xenografts in animals receiving gold nanoshells compared with control animals. Nanoshells that specifically target tumor cell receptors might be expected to

perform even better, particularly on larger and more mature tumors.

Targeting nanoshells and iron-oxide nanoparticles for receptor-directed thermal ablation

The realization of the full diagnostic and therapeutic potential of nanoparticles *in vivo*, in part, reflects the ability to target their localization and uptake to specific cells and tissues. Initial studies with nanoshells for thermal ablation depended on preferential delivery to tumors by exploiting the increased permeability and retention within the tumor neovasculature [32,33]. However, the gold surface of nanoshells can be readily conjugated to biologically active molecules, including antibodies [34]. Thus, an ortho-pyridyl-disulfide-*N*-hydroxysuccinimide polyethylene glycol polymer was used to conjugate HER2-specific IgG antibodies to gold nanoshell surfaces. Under conditions of dark-field microscopy, binding of the anti-HER2 nanoshells to HER2-positive SKBr3 human mammary adenocarcinoma cells was detected by gold-specific silver enhancement staining. These observations highlight the ability of gold nanoshells that are suitable for thermal ablation to be conjugated to targeting molecules for tumor-specific delivery. Iron-oxide or iron-cored nanoshells should provide contrast agents suitable for MRI imaging, which, in addition to their non-invasive nature, would provide even more powerful and generally useful diagnostic tools [14].

Nanometer-sized particles of different shapes and compositions are emerging as important new tools for cancer

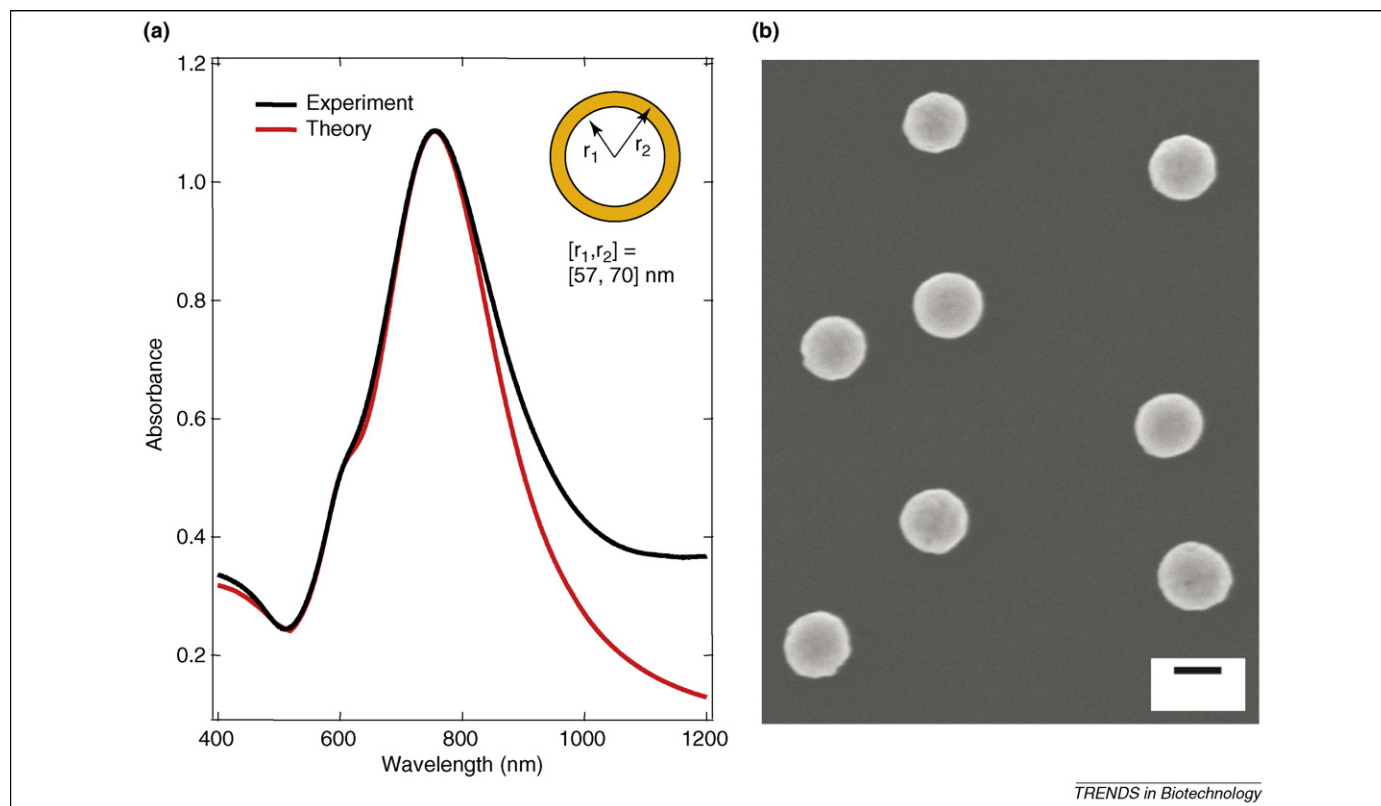


Figure 1. Gold–silica nanoshells tuned to NIR wavelengths. Gold nanoshells are synthesized using SiO₂ cores (~ 114 nm diameter) with surface seeding using 1–3 nm gold particles on cores, followed by controlled surface fill-in with gold by reductive deposition from a gold salt solution. (a) The experimental and theoretical extinction spectra of nanoshells with $[r_1, r_2] = [57, 70]$ nm (inset). The radii define the inner and outer diameters of the shell and hence its thickness, leading to the generation of gold nanoshells with an absorption maximum in the NIR (~ 780 nm). (b) Scanning electron micrograph of synthesized gold nanoshells. Bar = 100 nm.

diagnosis, staging and therapeutics. The lack of broader adoption might reflect the considerable barriers to implementation (e.g. availability of particles and suitable automated detection systems) and the absence of biosafety data [35]. Potential applications of thermal-induced tumor ablation by targeted delivery of gold nanoshells to colon cancer cells and, by analogy, to other types of tumors with unique receptors will be addressed below.

Colorectal cancer

Guanylyl cyclase C

GCC is the intestinal receptor for the high-affinity, bacterial, diarrheagenic, heat-stable enterotoxins (STs) and the lower affinity endogenous ligands guanylin and uroguanylin, which induce accumulation of cGMP [4]. In turn, cGMP activates a protein kinase that phosphorylates ion channels, mediating the efflux of salt and water and, in the case of ST, causes diarrhea (Figure 2). GCC is selectively expressed in the apical membranes of intestinal mucosa cells and colon cancer cells. Indeed, expression of GCC has been detected in all colorectal tumors, but not in extra-gastrointestinal tissues or tumors [4,36] Selective over-expression of GCC by colorectal cancer cells and its anatomical compartmentalization – it is normally confined to mucosa but is accessible to the systemic vasculature in metastatic disease – suggests its utility as a target for delivering therapeutic agents *in vivo*.

GCC as a specific receptor target in colon cancer cells

GCC might be uniquely suited for targeting novel therapeutic agents to metastatic colorectal cancer cells [36]. More specifically, if nanoshells of defined optical resonance frequencies or RF absorptivity can be conjugated to ST for specific delivery, targeted by GCC, it might prove possible to thermally ablate metastatic colorectal tumors. The use of infrared energy in a band where there is minimal absorption by normal tissues is attractive and has been explored experimentally in animals. Unfortunately, thicker tissue masses, such as those found in humans, and highly vascularized (IR absorbing) tissue, such as the liver, present potential problems. RF heating is an alternative with some experimental foundation. It could prove useful, particularly if MRI imaging is used first to locate metastases for focused energy application.

Conjugation of ST to organic and inorganic molecules preserves ligand binding

The 18 amino acid core peptide of ST is sufficient for GCC receptor binding with nanomolar affinity and full biological activity, *in vitro* and *in vivo*. Although manipulation of the ST carboxyl terminus eliminates receptor binding and biological activity, manipulation of the N-terminus preserves binding and enables delivery of large, conjugated, heterologous molecules to colorectal cancer cells. ¹²⁵I-ST conjugated to biotin, using a long-chain hydrocarbon linker arm coupled to *N*-hydroxy-succinimide, was found to bind to receptors in the GCC positive T84 cell membranes in a time- and concentration-dependent fashion. Binding was also quantitatively competed out by unlabeled ST, demonstrating specificity of the receptor interaction [36]. Analyses of equilibrium binding

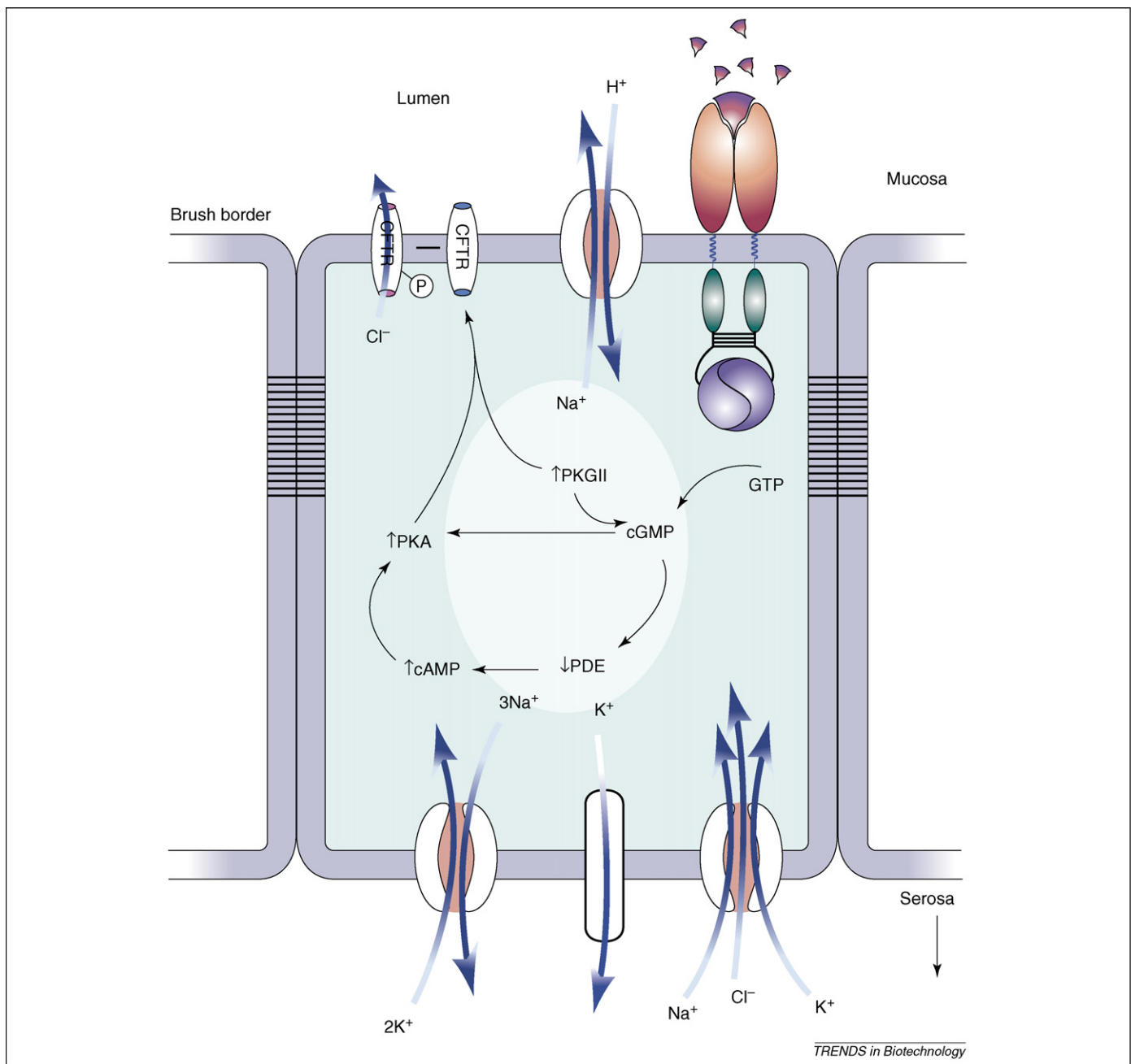
by the method of Scatchard demonstrated curvilinear isotherms, and the binding parameters derived from those analyses were comparable to those obtained with unconjugated ¹²⁵I-ST. In addition, labeled ST conjugated to biotin and avidin was specifically internalized in a time-dependent fashion by T84 cells [37,38]. Similarly, biotinylated ST was immobilized on streptavidin or anti-biotin antibody coated polyvinylchloride plates and used to capture cells expressing ST receptors, with high affinity and specificity [39]. Furthermore, biotinylated ST was coupled to streptavidin–gold and used to label cells expressing GCC, with high affinity and specificity. These data demonstrate that ST can be conjugated to molecules with dimensions and compositions comparable to gold nanoshells and retain full receptor-binding function and the ability to undergo internalization.

Hence, ST attached to gold nanoshells, when injected, should target to micrometastases and/or tumor sites. ST-binding selectively occurs through surface-bound GCC on cancer cells followed by ST-bound nanoshell internalization. NIR radiation could then be used, and the energy absorbed by the internalized gold nanoshells results in heat emission and thermal ablation of the micrometastases. Alternatively, RF-induced ablation of targeted iron-oxide particles could be used; studies are underway using cell lines and animal models of colon cancer to validate such an approach.

Colon cancer diagnostics and therapeutics using nanostructures

The application of nanotechnology to the diagnosis and treatment of colorectal cancer has the promise of enhancing conventional methods as well as fostering the development of novel approaches for detection and therapy. With respect to diagnostics, assays can be divided into *in vitro* (e.g. diagnostic tests on blood serum) and *in vivo* (e.g. imaging of administered agents) applications. Expected improvements for *in vitro* diagnostics include increases in analytical sensitivity without sacrificing specificity. The expected benefits of improved analytical performance include non-amplification assays that are faster and require smaller sample sizes and less expensive detection technologies, which can be readily miniaturized. These benefits might result in greater accessibility of diagnostic tools to clinicians and patients. With regard to *in vivo* imaging, enhancement of conventional imaging agents has resulted in higher sensitivity and finer resolution of tumors. Furthermore, the application of nanotechnology to develop novel imaging agents has resulted in new roles for non-invasive imaging in the detection, staging and overall management of patients with cancer [10–16]. With respect to therapy, targeted nanostructures offer potential solutions to the limitations of standard chemo- and radio-therapeutic modalities, particularly in the context of collateral damage to normal tissues in proximity to, and distant from, tumors and the associated dose-limiting clinical toxicities, which severely restrict the efficacy of the current therapeutic armamentarium.

Although there are many examples of the application of nanotechnology to various analyses and diseases, there are few examples that directly address the *in vitro* diagnosis of



TRENDS in Biotechnology

Figure 2. Regulation of intestinal secretion by the heat-stable enterotoxin (ST) and GCC. Bacteria, such as *E. coli*, containing plasmids that encode a member of the homologous peptide family of STs colonize the intestine following the consumption of contaminated food and/or water. Bacterial colonization leads to production of ST in the gut lumen. ST specifically recognizes and binds to the extracellular domain of GCC, which is expressed in the brush border membranes of intestinal mucosa cells from the duodenum to the rectum. The interaction of ST and the extracellular domain of GCC is translated across the plasma membrane to activate the cytoplasmic catalytic domain, resulting in the production and accumulation of cGMP. This cyclic nucleotide binds to and activates cGMP-dependent protein kinase II (PKG II), also localized in the intestinal cell brush border membrane. Furthermore, cGMP can activate cAMP-dependent protein kinase (PKA), either directly or by inhibiting a cAMP-specific phosphodiesterase (PDE), and induces the accumulation of cAMP. The cystic fibrosis transmembrane conductance regulator (CFTR), which is co-localized with GCC and PKG II in brush border membranes, is a substrate for this protein kinase and PKA. CFTR is a chloride channel, and its phosphorylation by PKA or PKG results in a persistent open state, permitting chloride to flow down its concentration gradient from the intracellular to the extracellular compartment. Other ion channels and transporters in the cell maintain the electroneutrality of ST-induced chloride efflux. Vectorial water flux from the basolateral to the apical surface is driven by these ionic conductances, resulting in the accumulation of fluid and electrolytes in the intestinal lumen and secretory diarrhea.

CRC. However, the potential of nanostructures is apparent from the results from other disease systems. Nanostructures, particularly nanoparticles, offer a diverse range of labels that provide direct visual detection and multiplexing capabilities for assaying proteins or detecting nucleic acids [40]. Some of the many types of nanostructures that have been used as components of *in vitro* diagnostic tests for protein markers or nucleic acid targets are presented in

Table 2, and a comprehensive bibliography is available from the National Cancer Institute (http://nano.cancer.gov/resource_center/scientific_bibliography.asp). These nanostructure-based analytical strategies could also be applied to the analysis of specific colon cancer-related markers or nucleic acid sequences.

Similar to *in vitro* diagnostics, the use of nanostructures for *in vivo* imaging is also a particularly promising area of

Table 2. Nanostructures for diagnostic applications

<i>In vitro</i> diagnostic		
Nanostructure	Application	Refs
Nanochannel		
Glass	DNA sequencing	^a
Nanocrystal		
CdS, CuS, PbS	Single-nucleotide polymorphism	[48]
Fluorescein diacetate	IgG	[49]
Nanoparticle		
Eulll-chelate-doped polystyrene	PSA	[50]
Au	Prion protein	[51]
2-methacryloyloxyethyl phosphorylcholine	C-reactive protein	[52]
Polystyrene	Single-base mutation	[53]
Silica	Calf thymus DNA	[54]
Ag on Au	IgG	[55]
Tris (2,2'-bipyridyl) dichloroRu (II) hexahydrate-doped silica	IgG, DNA	[56]
Nanopore		
Silicon nitride	DNA sequencing	[57]
Nanoprism		
Ag	–	[58]
Au	–	[59]
Nanorod		
Au/Ag/Ni/Pd/Pt	IgG	[60]
Nanotube		
Carbon	DNA	[61]
Nanowire		
Si	Influenza A	[62]
Au	<i>E. coli</i>	[63]
Polypyrrole	DNA	[64]
<i>In vivo</i> diagnostic		
Nanostructure	Application	Refs
Liposome		
Gadolinium	MRI imaging	[65,66]
Dual-fluorescence or iron oxide	Optical and MRI imaging	[67]
Dendrimer		
Gadolinium	MRI imaging	[41,42]
Nanoparticle		
Dextran-coated iron oxide	MRI imaging	[45]
Quantum dots	Near-infrared imaging	[46,47,68]
Gold	Optical detection	[69]
Nanoshell		
Gold	Optical detection	[70]
Nanotube		
Ultrashort Gd packed nanotubes	MRI imaging	[71]

^ahttp://www.ece.cmu.edu/~mems/pubs/show.php?pub_id=160

colon cancer diagnostics. However, there are few examples of the application of nanotechnology to the imaging of CRC. Several examples that have been applied to enhancing detection and management of various diseases are outlined in Table 2. The technology most readily applicable to colorectal cancer includes novel contrast agents for MRI.

Nanostructures that modify conventional contrast agents, such as gadolinium, or imaging agents, such as iron oxide, have the potential to enhance the diagnostic power of clinical imaging [41–45]. Not only do these nanostructures improve the features of conventional MRI imaging, they also present opportunities to change how colorectal cancer is detected and managed.

Among the technologies in development that might result in the introduction of new modalities in CRC imaging is the use of near-infrared fluorescence imaging (NIRF). NIRF can be useful for imaging gastrointestinal diseases such as CRC because the current clinical evaluation of CRC already uses fiber optic examination of luminal surfaces [46]. This standard of practice can be enhanced by endoscopic visualization of near-infrared fluorescing imaging agents such as tunable quantum dots. Indeed, a murine model of colon cancer has already been studied using a NIRF agent [47].

Beyond imaging and detection, targeted nanostructures offer opportunities to develop novel approaches to treat colorectal and other tumors [10]. Liposomal encapsulation of anthracyclins, including doxorubicin, has had success as an FDA-approved treatment for metastatic ovarian cancer refractory to paclitaxel- and platinum-based agents. Moreover, these stealth nanostructures have been investigated for the treatment of breast cancer, non-Hodgkin's lymphoma and small-cell lung cancer. Similarly, nanoparticle delivery of paclitaxel is being used for the treatment of patients with metastatic breast cancer who have failed standard adjuvant chemotherapy, including anthracycline-based regimens. In preclinical development, nanostructures that are targeted specifically to tumor-expressed molecules are being used to improve the specificity of delivery of cytotoxic chemotherapeutics and limit the collateral damage to normal tissues that is normally associated with their use. Indeed, nanostructures have been used in conjunction with antibodies, proteins and small-molecule ligands targeted to specific tumor-associated receptors to deliver chemotherapeutic agents. This results in greater pharmacological and clinical efficacy and is associated with lower adverse events in animal tumor-xenograft models. In this context, antibody-targeted liposomes effectively accumulate in colorectal cancer cells in mouse xenograft models. These next generation of nanostructured delivery systems, with demonstrated efficacy in animal models, will be translated into early-phase clinical trials in the near-term for the delivery of chemotherapy to cancer patients.

Conclusion

The broad field of cancer management has a history of quickly replacing existing methodologies with ones that offer advantages in terms of improved diagnostic capabilities, increased sensitivity for tumor staging, and better therapeutic approaches and drug delivery. Nanotechnology has several beneficial attributes that might improve the management of colon cancer patients. Indeed, there are now signs that the potential provided by nanotechnology is being evaluated, and the first steps are being taken in the development of improved colorectal cancer imaging, therapeutics and the eventual implementation of targeted

strategies for ablation. Although this Opinion has focused on CRC as a particularly tempting target for the early application of nanotechnology-based approaches, the potential for other tumors with similar highly specific target molecules should be clear.

Acknowledgements

This work was supported, in part, by grants from the PA Department of Health (SAP4100026302 to PF), NIH (HL-69256 to SS, CA75123, CA79663 and CA95026 to SAW), Targeted Diagnostic and Therapeutics, Inc., West Chester, PA (to SAW), the Cardeza Foundation for Hematological Research, Philadelphia, PA (to SS), the Kimmel Cancer Center, Philadelphia, PA (to PF) and the Robert A. Welch Foundation C-1220, the Department of Defense Breast Cancer Research Program (DAMD17-03-1-0384 to NH and FT) and the Texas Institute for Bio-Nano Materials and Structures for Aerospace Vehicles funded by NASA (NH, FT). SAW is the Samuel M.V. Hamilton Endowed Professor.

References

- Meyerhardt, J.A. and Mayer, R.J. (2005) Systemic therapy for colorectal cancer. *N. Engl. J. Med.* 352, 476–487
- Pantel, K. *et al.* (1999) Detection and clinical importance of micrometastatic disease. *J. Natl. Cancer Inst.* 91, 1113–1124
- O'Connell, J.B. *et al.* (2004) Colon cancer survival rates with the new American Joint Committee on Cancer sixth edition staging. *J. Natl. Cancer Inst.* 96, 1420–1425
- Carrithers, S.L. *et al.* (1996) Guanylyl cyclase C is a selective marker for metastatic colorectal tumors in human extraintestinal tissues. *Proc. Natl. Acad. Sci. U. S. A.* 93, 14827–14832
- Wolfe, H.R. *et al.* (2002) *In vivo* imaging of human colon cancer xenografts in immunodeficient mice using a guanylyl cyclase C-specific ligand. *J. Nucl. Med.* 43, 392–399
- Frick, G.S. *et al.* (2005) Guanylyl cyclase C: a molecular marker for staging and postoperative surveillance of patients with colorectal cancer. *Expert Rev. Mol. Diagn.* 5, 701–713
- Nel, A. *et al.* (2006) Toxic potential of materials at the nanolevel. *Science* 311, 622–627
- Service, R.F. (2006) Science policy. Priorities needed for nano-risk research and development. *Science* 314, 45
- Ferrari, M. (2005) Cancer nanotechnology: opportunities and challenges. *Nat. Rev. Cancer* 5, 161–171
- Couvreur, P. and Vauthier, C. (2006) Nanotechnology: intelligent design to treat complex disease. *Pharm. Res.* 23, 1417–1450
- Cuenca, A.G. *et al.* (2006) Emerging implications of nanotechnology on cancer diagnostics and therapeutics. *Cancer* 107, 459–466
- Farokhzad, O.C. and Langer, R. (2006) Nanomedicine: developing smarter therapeutic and diagnostic modalities. *Adv. Drug Deliv. Rev.* 58, 1456–1459
- Grodzinski, P. *et al.* (2006) Nanotechnology for cancer diagnostics: promises and challenges. *Expert Rev. Mol. Diagn.* 6, 307–318
- Qiang, Y. *et al.* (2006) Iron/iron oxide core-shell nanoclusters for biomedical applications. *J. Nanoparticle Res.* 8, 489–496
- Sinha, R. *et al.* (2006) Nanotechnology in cancer therapeutics: bioconjugated nanoparticles for drug delivery. *Mol. Cancer Ther.* 5, 1909–1917
- Yih, T.C. *et al.* (2006) Engineered nanoparticles as precise drug delivery systems. *J. Cell. Biochem.* 97, 1184–1190
- Kroto, H.W. *et al.* (1985) C₆₀: buckminsterfullerene. *Nature* 318, 162–163
- Li, J. *et al.* (2005) Carbon nanotubes and nanowires for biological sensing. *Methods Mol. Biol.* 300, 191–123
- Woolley, A.T. *et al.* (2000) Structural biology with carbon nanotube AFM probes. *Chem. Biol.* 7, R193–R204
- Moses, C. *et al.* (1955) Experimental and clinical studies with radioactive colloidal gold in the therapy of serous effusions arising from cancer. *Cancer* 8, 417–423
- Ahlberg, A. *et al.* (1969) Intra-articular injection of radioactive gold in treatment of chronic synovial effusion in the knee. *Acta Rheumatol. Scand.* 15, 81–89
- West, J.L. and Halas, N.J. (2003) Engineered nanomaterials for biophotonic applications, improving sensing, imaging and therapeutics. *Annu. Rev. Biomed. Eng.* 5, 285–292
- Loo, C. *et al.* (2005) Immunotargeted nanoshells for integrated cancer imaging and therapy. *Nano Lett.* 5, 709–711
- Thorek, D.L. *et al.* (2006) Superparamagnetic iron oxide nanoparticle probes for molecular imaging. *Ann. Biomed. Eng.* 34, 23–38
- Hirsch, L.R. *et al.* (2003) Nanoshell-mediated near-infrared thermal therapy of tumors under magnetic resonance guidance. *Proc. Natl. Acad. Sci. U. S. A.* 100, 13549–13554
- O'Neal, D.P. *et al.* (2004) Photo-thermal tumor ablation in mice using near infrared-absorbing nanoparticles. *Cancer Lett.* 209, 171–176
- Devalapally, H. *et al.* (2007) Poly(ethylene oxide)-modified poly(beta-amino ester) nanoparticles as a pH-sensitive system for tumor-targeted delivery of hydrophobic drugs. Part 3: Therapeutic efficacy and safety studies in ovarian cancer xenograft model. *Cancer Chemother. Pharmacol.* 59, 477–484
- van Vlerken, L.E. and Amiji, M.M. (2006) Multi-functional polymeric nanoparticles for tumour-targeted drug delivery. *Expert Opin. Drug Deliv.* 3, 205–216
- Farokhzad, O.C. *et al.* (2006) Targeted nanoparticle–aptamer bioconjugates for cancer chemotherapy *in vivo*. *Proc. Natl. Acad. Sci. U. S. A.* 103, 6315–6320
- Akerman, M.E. *et al.* (2002) Nanocrystal targeting *in vivo*. *Proc. Natl. Acad. Sci. U. S. A.* 99, 12617–12621
- Gao, X. *et al.* (2004) *In vivo* cancer targeting and imaging with semiconductor quantum dots. *Nat. Biotechnol.* 22, 969–976
- Matsumura, Y. and Maeda, H. (1986) A new concept for macromolecular therapeutics in cancer chemotherapy: mechanism of tumor-tropic accumulation of proteins and the antitumor agent smancs. *Cancer Res.* 46, 6387–6392
- Hainfeld, J.F. *et al.* (2004) The use of gold nanoparticles to enhance radiotherapy in mice. *Phys. Med. Biol.* 49, N309–N315
- Loo, C. *et al.* (2004) Nanoshell-enabled photonics-based imaging and therapy of cancer. *Technol. Cancer Res. Treat.* 3, 33–40
- Kommareddy, S. and Amiji, M. (2007) Biodistribution and pharmacokinetic analysis of long-circulating thiolated gelatin nanoparticles following systemic administration in breast cancer-bearing mice. *J. Pharm. Sci.* 96, 397–407
- Birbe, R. *et al.* (2005) Guanylyl cyclase C is a marker of intestinal metaplasia, dysplasia, and adenocarcinoma of the gastrointestinal tract. *Hum. Pathol.* 36, 170–179
- Urbanski, R. *et al.* (1995) Internalization of *E. coli* ST mediated by guanylyl cyclase C in T84 human colon carcinoma cells. *Biochim. Biophys. Acta* 1245, 29–36
- Hakki, S. *et al.* (1993) Solubilization and characterization of functionally coupled *Escherichia coli* heat-stable toxin receptors and particulate guanylate cyclase associated with the cytoskeleton compartment of intestinal membranes. *Int. J. Biochem.* 25, 557–566
- Hugues, M. *et al.* (1992) Affinity purification of functional receptors for *Escherichia coli* heat-stable enterotoxin from rat intestine. *Biochemistry* 31, 12–16
- Seydack, M. (2004) Nanoparticle labels in immunosensing using optical detection methods. *Biosens. Bioelectron.* 20, 2454–2469
- Kobayashi, H. *et al.* (2005) Detection of lymph node involvement in hematologic malignancies using micromagnetic resonance lymphangiography with a gadolinium-labeled dendrimer nanoparticle. *Neoplasia* 7, 984–991
- Kobayashi, H. *et al.* (2004) Lymphatic drainage imaging of breast cancer in mice by micro-magnetic resonance lymphangiography using a nano-size paramagnetic contrast agent. *J. Natl. Cancer Inst.* 96, 703–708
- Mahmood, U. and Weissleder, R. (2003) Near-infrared optical imaging of proteases in cancer. *Mol. Cancer Ther.* 2, 489–496
- Perez, J.M. *et al.* (2003) Viral-induced self-assembly of magnetic nanoparticles allows the detection of viral particles in biological media. *J. Am. Chem. Soc.* 125, 10192–10193
- Harisinghani, M.G. *et al.* (2003) Noninvasive detection of clinically occult lymph-node metastases in prostate cancer. *N. Engl. J. Med.* 348, 2491–2499
- Weissleder, R. *et al.* (2005) Cell-specific targeting of nanoparticles by multivalent attachment of small molecules. *Nat. Biotechnol.* 23, 1418–1423
- Weissleder, R. *et al.* (1999) *In vivo* imaging of tumors with protease-activated near-infrared fluorescent probes. *Nat. Biotechnol.* 17, 375–378

- 48 Liu, G. *et al.* (2005) Nanocrystal-based bioelectronic coding of single-nucleotide polymorphisms. *J. Am. Chem. Soc.* 127, 38–39
- 49 Chan, C.P. *et al.* (2004) Nanocrystal biolabels with releasable fluorophores for immunoassays. *Anal. Chem.* 76, 3638–3645
- 50 Huhtinen, P. *et al.* (2004) Immunoassay of total prostate-specific antigen using europium(III) nanoparticle labels and streptavidin-biotin technology. *J. Immunol. Methods* 294, 111–122
- 51 Henry, J. *et al.* (2004) Development of a nanoparticle-based surface-modified fluorescence assay for the detection of prion proteins. *Anal. Biochem.* 334, 1–8
- 52 Park, J. *et al.* (2004) Evaluation of 2-methacryloyloxyethyl phosphorylcholine polymeric nanoparticle for immunoassay of C-reactive protein detection. *Anal. Chem.* 76, 2649–2655
- 53 Sato, K. *et al.* (2004) Single-base mutation detection using neutravidin-modified polystyrene nanoparticle aggregation. *Anal. Sci.* 20, 893–894
- 54 Zhang, D. *et al.* (2004) Silica-nanoparticle-based interface for the enhanced immobilization and sequence-specific detection of DNA. *Anal. Bioanal. Chem.* 379, 1025–1030
- 55 Chu, X. *et al.* (2005) An electrochemical stripping metalloimmunoassay based on silver-enhanced gold nanoparticle label. *Biosens. Bioelectron.* 20, 1805–1812
- 56 Lian, W. *et al.* (2004) Ultrasensitive detection of biomolecules with fluorescent dye-doped nanoparticles. *Anal. Biochem.* 334, 135–144
- 57 Li, J. *et al.* (2003) DNA molecules and configurations in a solid-state nanopore microscope. *Nat. Mater.* 2, 611–615
- 58 Jin, R. *et al.* (2001) Photoinduced conversion of silver nanospheres to nanoprisms. *Science* 294, 1901–1903
- 59 Hao, E. *et al.* (2004) Synthesis and optical properties of anisotropic metal nanoparticles. *J. Fluoresc.* 14, 331–341
- 60 Nicewarner-Pena, S.R. *et al.* (2001) Submicrometer metallic barcodes. *Science* 294, 137–141
- 61 Wang, J. *et al.* (2004) Ultrasensitive electrical biosensing of proteins and DNA: carbon-nanotube-derived amplification of the recognition and transduction events. *J. Am. Chem. Soc.* 126, 3010–3011
- 62 Patolsky, F. *et al.* (2004) Electrical detection of single viruses. *Proc. Natl. Acad. Sci. U. S. A.* 101, 14017–14022
- 63 Basu, M. *et al.* (2004) Nano-biosensor development for bacterial detection during human kidney infection: use of glycoconjugate-specific antibody-bound gold nanowire arrays (GNWA). *Glycoconj. J.* 21, 487–496
- 64 Ramanathan, K. *et al.* (2005) Bioaffinity sensing using biologically functionalized conducting polymer nanowire. *J. Am. Chem. Soc.* 127, 496–497
- 65 Parac-Vogt, T.N. *et al.* (2005) Paramagnetic liposomes containing amphiphilic bisamide derivatives of Gd-DTPA with aromatic side chain groups as possible contrast agents for magnetic resonance imaging. *Eur. Biophys. J.* 11, 1–9
- 66 Saito, R. *et al.* (2005) Gadolinium-loaded liposomes allow for real-time magnetic resonance imaging of convection-enhanced delivery in the primate brain. *Exp. Neurol.* 196, 381–389
- 67 Mulder, W.J. *et al.* (2005) MR molecular imaging and fluorescence microscopy for identification of activated tumor endothelium using a bimodal lipidic nanoparticle. *FASEB J.* 19, 2008–2010
- 68 Parungo, C.P. *et al.* (2005) Intraoperative identification of esophageal sentinel lymph nodes with near-infrared fluorescence imaging. *J. Thorac. Cardiovasc. Surg.* 129, 844–850
- 69 Rahman, M. *et al.* (2005) Optical imaging of cervical pre-cancers with structured illumination: an integrated approach. *Gynecol. Oncol.* 99, S112–S115
- 70 Loo, C. *et al.* (2005) Gold nanoshell bioconjugates for molecular imaging in living cells. *Opt. Lett.* 1, 1012–1014
- 71 Sitharaman, B. *et al.* (2005) Superparamagnetic gadonanotubes are high-performance MRI contrast agents. *Chem. Commun.* 21, 3915–3917

Elsevier.com – linking scientists to new research and thinking

Designed for scientists' information needs, Elsevier.com is powered by the latest technology with customer-focused navigation and an intuitive architecture for an improved user experience and greater productivity.

The easy-to-use navigational tools and structure connect scientists with vital information – all from one entry point. Users can perform rapid and precise searches with our advanced search functionality, using the FAST technology of Scirus.com, the free science search engine. Users can define their searches by any number of criteria to pinpoint information and resources. Search by a specific author or editor, book publication date, subject area – life sciences, health sciences, physical sciences and social sciences – or by product type. Elsevier's portfolio includes more than 1800 Elsevier journals, 2200 new books every year and a range of innovative electronic products. In addition, tailored content for authors, editors and librarians provides timely news and updates on new products and services.

Elsevier is proud to be a partner with the scientific and medical community. Find out more about our mission and values at Elsevier.com. Discover how we support the scientific, technical and medical communities worldwide through partnerships with libraries and other publishers, and grant awards from The Elsevier Foundation.

As a world-leading publisher of scientific, technical and health information, Elsevier is dedicated to linking researchers and professionals to the best thinking in their fields. We offer the widest and deepest coverage in a range of media types to enhance cross-pollination of information, breakthroughs in research and discovery, and the sharing and preservation of knowledge.

Elsevier. Building insights. Breaking boundaries.
www.elsevier.com

Design and construction of targeted AAVP vectors for mammalian cell transduction

Amin Hajitou¹, Roberto Rangel¹, Martin Trepel², Suren Soghomonyan³, Juri G Gelovani³, Mian M Alauddin³, Renata Pasqualini¹ & Wadih Arap¹

¹Department of Genitourinary Medical Oncology, The University of Texas M. D. Anderson Cancer Center, 1515 Holcombe Boulevard, Houston, TX 77030. ²Department of Hematology and Oncology and Institute for Molecular Medicine and Cell Research, University of Freiburg Medical Center, Hugstetter Strasse 55, D-79106 Freiburg, Germany. ³Department of Experimental Diagnostic Imaging, The University of Texas M. D. Anderson Cancer Center, 1515 Holcombe Boulevard, Houston, TX 77030. Correspondence should be addressed to R.P. (rpasqual@mdanderson.org) or W.A. (warap@mdanderson.org).

Published online 15 March 2007; doi:10.1038/nprot.2007.51

Bacteriophage (phage) evolved as bacterial viruses, but can be adapted to transduce mammalian cells through ligand-directed targeting to a specific receptor. We have recently reported a new generation of hybrid prokaryotic–eukaryotic vectors, which are chimeras of genetic *cis*-elements of recombinant adeno-associated virus and phage (termed AAVP). This protocol describes the design and construction of ligand-directed AAVP vectors, production of AAVP particles and the methodology to transduce mammalian cells *in vitro* and to target tissues *in vivo* after systemic administration. Targeted AAVP particles are made in a two-step process. First, a ligand peptide of choice is displayed on the coat protein to generate a targeted backbone phage vector. Then, a recombinant AAV carrying a mammalian transgene cassette is inserted into an intergenomic region. High-titer suspensions ($\sim 10^{10}$ – 10^{11} transducing units per μl) can be produced within 3 days after vector construction. Transgene expression by targeted AAVP usually reaches maximum levels within 1 week.

INTRODUCTION

The use of new genetic systems for the study of currently intractable biological questions will require the development of ligand-directed (targeted) vectors that can be systemically delivered. Over the past decade, common approaches at targeted gene delivery have typically relied on ablation of the native tropism of mammalian viruses, redirection to alternative receptors or both^{1–8}. Incorporation of homing peptides selected from bacteriophage (phage) display library screenings into mammalian viral vectors has been attempted, but such strategy has the potential to alter the structure of the capsid, affect the targeting attributes of the ligand peptides or even prevent the display within a viable viral capsid altogether^{9–13}. In contrast, phage have no intrinsic tropism for mammalian cells^{14,15} and can mediate modest gene expression in mammalian cells after genetic manipulation^{16–19}. In theory, phage-based vectors have some potential advantages over animal viruses for mammalian cell-targeted delivery of transgenes. First, there are no known natural receptors for phage (which have evolved as prokaryotic viruses) on mammalian cells^{14,15}. However, receptor-mediated internalization by mammalian cells occurs if phage vectors are genetically modified to display specific ligands, such as fibroblast growth factor (FGF2), anti-ErbB2 scFv F5 antibody and integrin-binding peptides^{16–20}. Moreover, bacteriophage have long been administered to humans, from its antibacterial use in the environment during the preantibiotic era¹⁴ to the very recent Food and Drug Administration approval of certain phage preparations as antibacterial food additives²¹. Indeed, feasibility clinical trials have shown that the selection of phage libraries in cancer patients can yield ligand–receptor systems^{22,23} and that serial library administration can be accomplished without major untoward clinical effects²⁴. Finally, unlike mammalian viruses, phage do not require further context modification of their capsid because the targeting peptides are actually selected and isolated directly as homing to specific cell-surface receptors^{22,25–30}.

Despite these potential advantages, phage-based vectors have inherently been considered poor gene delivery vehicles. As a

working hypothesis, we proposed that the rate-limiting step might be mechanistically related to the post-targeting fate of the single-stranded DNA of the phage genome¹. In an attempt to improve phage as targeted vectors for mammalian cells, we reasoned that the genetic incorporation of compatible *cis*-elements (such as inverted terminal repeats (ITRs)) from a mammalian—yet single-stranded—DNA virus such as recombinant adeno-associated virus (AAV) would improve post-targeting transgene expression. Thus, we have developed ligand-directed vectors as a hybrid between AAV and phage (termed AAVP). In our targeted AAVP prototype vector¹, the targeted phage displays an RGD-4C peptide that binds to α_v integrins^{26,27,29,31}, with the mammalian transgene cassette flanked by full-length ITRs of AAV serotype 2. We reported¹ that the improved mammalian transduction efficiency by targeted AAVP over conventional phage-based vectors is associated with an improved fate of the delivered transgene, through maintenance of the entire mammalian transgene cassette, better persistence of episomal DNA and formation of concatamers of the transgene cassette¹. Here, we detail how to insert an AAV transgene cassette into the backbone phage vector genome to generate targeted AAVP hybrid constructs (Steps 1–18) and how to produce, purify and titrate the vector preparations (Steps 19–26). We also describe a standard protocol for AAVP-mediated mammalian cell transduction, both in tissue culture and in targeted tissues *in vivo* after systemic administration. Briefly, DNA oligonucleotide sequences encoding peptide ligands are inserted into the *Sfi*I site of the gene of the pIII minor coat protein of fUSE5-MCS (multicloning site)-based filamentous phage^{1,32,33}. Phage produced in this manner display 3–5 copies of the specific peptide³². The fUSE5-MCS-based filamentous phage display vector is then genetically modified to generate the corresponding targeted AAVP vector, by inserting a recombinant AAV (carrying the desirable promoter/transgene cassette) into an intergenomic region of the phage genome. This strategy also serves to construct

non-targeted control vectors (either displaying no peptides or displaying mutant/scrambled versions of the peptide). Targeted and control AAVP particles are amplified, isolated and purified by adapting the protocols used for phage^{30,32}. AAVP particles are then resuspended in phosphate-buffered saline (PBS; pH 7.4) and recentrifuged to remove residual bacterial debris. Next, AAVP particles in suspension are sterile-filtered through 0.45-µm pores, then titrated by infection of host bacteria for colony counting on Luria–Bertani (LB) agar plates under a double antibiotic selection and expressed as bacterial transducing units (TU). Transduction of mammalian cells in culture is performed by incubation with the targeted AAVP for 4 h in serum-free medium with a ratio of at least 10⁶ TU per cell. Transgene expression begins 48–72 h later and reaches a maximum level by 1 week. Typically, non-targeted AAVP vectors or AAVP displaying mutated and/or scrambled versions of the targeting peptide serve as negative controls for the ligand-directed (i.e., targeting) experiments; either a corresponding version of a targeted phage vector “AAV-less” or a targeted AAVP containing an “ITR-less” or mutant ITR serves as a suitable control for post-internalization (i.e., integration, concatemerization) experiments.

Under these conditions, ~10–20% of cells are transduced in culture. Specificity can be demonstrated by blocking the interaction of the targeted AAVP by preincubating the target cells with the corresponding synthetic peptide. In our prototype RGD-4C AAVP,

transduction inhibition was dose-dependent, greater than 99% inhibition was observed and incubation with nonspecific negative control peptides had no detectable effects¹. This data set showcases an example of targeted AAVP transduction of mammalian cells expressing a specific receptor and mediated by an established ligand–receptor system. Transduction of a target tissue *in vivo* will vary among ligand–receptors but one can attempt to use increasing doses of targeted AAVP, starting at 10¹⁰ TU per mouse, administered intravenously (tail vein). Transgene expression should be monitored and its detection can be expected starting from day 3 after delivery. Depending on the specific reporter used, one can determine gene expression initiation in the target and maximal expression timing. Evidently, different organs will require different ligand peptides and particular conditions should be anticipated for optimal temporal and spatial transduction. In an unpublished work, we have shown systemic targeted tissue-specific transduction of the lung tissue in wild-type mice via a homing peptide³⁴ that targets membrane dipeptidase in the lung endothelium³⁵; we have also tested a tumor-homing peptide²⁵ that targets MMP-2 and MMP-9 to transduce human tumor xenografts with phage-based vectors. In addition to the suicide gene therapy strategy previously reported¹, other targeted AAVP including applications for delivery of therapeutic genes (unpublished observations) will follow.

MATERIALS

REAGENTS

- Plasmids:
 - fUSE5^{1,32,33,36} phage plasmid, accession number AF218364
 - fd-tet^{1,32,33,36} phage plasmid, accession number AF217317
 - fMCS^{1,36} phage plasmid, accession number AF218733
 - fUSE5-MCS¹ phage plasmid
 - pAAV-GFP plasmid (Stratagene)
 - pMOD-Luc-Sh (Luciferase reporter; InvivoGen)
 - pCMVβ (β-galactosidase reporter; Clontech)
- Bacterial strains:
 - XL1-Blue MR supercompetent cells (Stratagene)
 - Escherichia coli* (MC1061 and k91Kan) (see ref. 36)
- LB–tetracycline plates, LB–tetracycline–kanamycin plates and media
- Terrific broth (TB) medium
- SOC medium (Invitrogen)
- Polyethylene glycol (PEG)/NaCl
- QIAquick Nucleotide removal kit (Qiagen)
- Essential restriction enzymes: *Bgl*I, *Bgl*II, *Hind*III, *Pst*I, *Pvu*II, *Sac*I, *Sfi*I and *Xho*I. Other restriction enzymes will be required depending on the specific sequences of the construct
- Phosphatase alkaline (Roche)
- T4 DNA ligase with ligase buffer (Invitrogen)
- Rapid DNA ligation kit (Roche)
- Agarose, electrophoresis (IscBioExpress)
- E-Gel 0.8% agarose (Invitrogen)
- QIAquick Gel extraction kit (Qiagen)
- Phosphorylated DNA linkers (NEB)
- *Taq*-DNA polymerase with supplied buffer (Promega)

- 100 mM dNTPs (Fisher)
- Oligonucleotides (Sigma-Genosys) (see **Table 1**)
- DMSO **! CAUTION** DMSO is readily absorbed through the skin. When handling DMSO, wear appropriate gloves, safety glasses and use a pipeting aid under a safety chemical hood.
- Transfection reagent: Fugene (Roche)
- Human embryonic kidney cells (HEK293; ATCC)
- HEK293 cells are maintained in Dulbecco’s modified Eagle’s medium (Gibco), supplemented with 10% fetal bovine serum (Gibco), l-glutamine and penicillin/streptomycin
- D-Luciferin potassium salt (InvivoGen)
- Immunocompetent and immunodeficient mice (Harlan–Sprague–Dawley)
- ▲ **CRITICAL** Mice must be used according to the national and institutional guidelines concerning use of animals.

EQUIPMENT

- Fluorescent microscope (Olympus or equivalent).
- Fluorescence-activated cell sorting (FACS) to analyze and sort the cells by using a BD FACS Vantage (Becton–Dickinson)
- 0.22 µm filter units (Corning)
- 0.45 µm filter units (Corning)
- 24-well tissue culture plates
- Tissue culture incubator at 5% CO₂ for HEK293 cells and other cell lines
- Shaker at 37 °C
- Centrifuge Sorvall SA-600 and SLA-3000 rotors
- Cell electroporator (Life Technologies)
- *In vivo* Bioluminescence Imaging (BLI) System 200 (IVIS200; Xenogen)
- PCR machine (Eppendorf)
- DNA electrophoresis equipment (Bio-Rad)

TABLE 1 | Primer set sequences.

Primer set	Sequence	Function
A	5’-CACTCGGCCGACG-3’ 5’-TTCGGCCCCAGCGGC-3’	Oligonucleotide conversion from single- to double-stranded DNA
B	5’-TAATACGACTCACTATAGGGCAAG CTGATAAACCGATAACAATT-3’ 5’-CCCTCATAGTTAGCGTAACGATCT-3’	Primers routinely used to amplify the oligonucleotide sequences after insertion into the construct



REAGENT SETUP

PEG/NaCl solution stock 500 g of PEG and 584.5 g of NaCl in 2,380 ml H₂O (double-distilled) and store at 4 °C for up to 1 year.

TB medium 9.6 g of tryptone, 19.2 g of yeast extract and 3.2 ml of glycerol in 1 liter of H₂O. Autoclave, add 100 ml of TB supplements and 50 mg of kanamycin

TB supplements To prepare 1 liter of TB supplements, add 23.1 g of KH₂PO₄ and 125.4 g of K₂HPO₄ in 1 liter of H₂O (double distilled). Filter through 0.22 μm filter unit and store at 4 °C.

EQUIPMENT SETUP

Whole-body BLI of luciferase Mice are first anesthetized inside a clear plexiglass box by using an anesthetic gas admixture (2% isoflurane, 98% oxygen) and are then transferred to nose cones attached to the manifold in the imaging chamber. The imaging time is 5 min per side (dorsal/ventral), depending on the experiment. Imaging parameters are as follows: image acquisition time, 1 min; binning, 2; no filter; f/stop (aperture size), 1. Regions of interest can be defined manually over the tumors or target tissues for measuring signal intensities, expressed as photons s⁻¹ cm⁻² sr⁻¹.

PROCEDURE

Insertion of the targeted peptide into the pIII coat protein of fUSE5-MCS phage

1| Generate phage clones displaying targeting peptides by cloning the corresponding oligonucleotide sequences flanked by *Bgl*I restrictions sites into the *Sfi*I site of the gene for the pIII coat protein of fUSE5-MCS. The fUSE5-MCS plasmid can also be generated by replacing the 5.4 kb *Bam*HI–*Sac*II fragment of the fUSE5 with the 4.1 kb *Bam*HI–*Sac*II fragment from the fMCS plasmid that contains an MCS.

2| Design and convert the synthetic oligonucleotide templates flanked by *Bgl*I restriction sites (500 ng) to double-stranded DNA by PCR amplification. We use the following 57 bp oligonucleotide as a template: 5′-**CACTCG GCCGACGGGGCT**XXXXXXXXXX XXXXXXXXXXXXGGG**GCCGCTGGG GCCGAA**-3′. This template is flanked by the *Bgl*I restriction sites (GCCNNNNNGGC: underlined). The bold nucleotides in the above template sequence indicate the annealing of the sense and antisense primers, respectively. The nucleotide sequence encoding the displayed peptide is marked “X”.

Finally, we use primer set A (see **Table 1**) and 2.5 U of *Taq* DNA polymerase (Promega) in 20 μl. Use the following setup: 94 °C for 2 min, followed by 35 cycles at 94 °C for 30 s, 60 °C for 30 s and 72 °C for 30 s, followed by 72 °C for 5 min, held at 4 °C and stored at –20 °C until ready for Step 3.

▲ **CRITICAL STEP** For effective PCR, it is recommended to add DMSO (2% final) to weaken hydrogen bonding and prevent formation of hairpin structures.

3| Purify and elute the double-stranded DNA sequences containing *Bgl*I restriction sites by using a QIAquick nucleotide removal kit.

4| Digest oligonucleotides with *Bgl*I restriction enzyme for 4 h at 37 °C, then inactivate *Bgl*I activity by incubation at 65 °C for 20 min. Digestion with *Bgl*I restriction enzyme generates the following sticky ends:



5| Digest the fUSE5-MCS plasmid with *Sfi*I restriction enzyme for 1–2 h at 50 °C. Run the ~9.5-kb linearized fUSE5-MCS plasmid on an agarose gel or E-Gel 0.8% agarose to confirm digestion. The fUSE 5 backbone vector contains two *Sfi*I restriction sites³⁶ (GGCCNNNN/NGGCC) in the pIII gene. After digestion, the *Sfi*I restriction enzyme will generate non-identical, non-complementary three bases 3′-overhanging ends³⁶. This will allow directional cloning after removal of the stuffer that lies between these sites in the phage vector. A schematic representation of the final vector sequences is shown below.



? TROUBLESHOOTING

6| Ligate the *Sfi*I-digested fUSE5-MCS vector plasmid with the *Bgl*I-digested oligonucleotides by using the Rapid Ligation Kit for 5–10 min at room temperature (25 °C, **Fig. 1**). It is recommended not to inactivate *Sfi*I and not to dephosphorylate the linearized fUSE5-MCS plasmid, as this markedly reduces the efficiency of ligation. Ligate immediately after digestion. Also, set up a reaction with the fUSE5-MCS plasmid alone and no insert to estimate the bacterial transformation due to autoligation of the fUSE5-MCS plasmid and/or the presence of non-digested fUSE5-MCS plasmid.

7| Use 2 μl of the ligation product to transform MC1061 or XL1-Blue MR bacteria according to the manufacturer’s instructions. Incubate transformed bacteria on LB-tetracycline plates for 24 h at 37 °C.

8| Verify the correct insertion and nucleotide sequence by PCR of the bacterial colonies generated. Pick single colonies (at least ten single colonies plus colonies from vector alone as controls) in 20 μl of medium. Use the primer set B (see **Table 1**) and 2 U of *Taq* DNA polymerase (Promega) in 20 μl. Use the following setup: 94 °C for 3 min, followed by 35 cycles at 94 °C for 10 s, 60 °C for 30 s and 72 °C for 30 s.

▲ **CRITICAL STEP** It is recommended to add 2% DMSO to weaken hydrogen bonding and prevent formation of hairpin structures.



PROTOCOL

9| Run 2 μ l of PCR product on a 2% agarose gel or E-Gel 0.8% agarose to verify the insertion. Include the product of an fUSE5-MCS without insert, which will be smaller in size on the gel.

Insertion of recombinant (r) AAV into the MCS of the fUSE5-MCS plasmid displaying the targeting peptide

10| Prepare the rAAV carrying the transgene of interest. Remove and replace GFP from the pAAV-GFP plasmid with the transgene of interest if applicable. GFP can also be replaced with a GFP variant for maximal fluorescence such as eGFP (enhanced GFP, catalog number 6084-1 from ClonTech). Thus, the transgene of interest must be flanked by restriction sites compatible with the MCS of the pAAV plasmid.

11| Remove the transgene cassette flanked by the ITRs from the pAAV plasmid created in Step 10. Use the *PvuII* restriction enzyme that digests adjacent to the ITRs and gel-purify the released transgene-ITR-segment using the gel extraction kit (Fig. 1). Note that expression cassettes of interest should not have any *PvuII* site. Otherwise, alternative strategies should be used. Then, use an rAAV plasmid with a restriction map compatible with that of the expression cassette of interest. For instance, some AAV plasmids from Stratagene (or other commercial outfits) have convenient rare cutter restriction enzyme sites such as *SbfI* or *Sse8387I* adjacent to each *PvuII* site. Sometimes, these can be used for AAV vector genome insertion into the phage vector backbone if other genetic elements permit this utilization.

12| The targeted fUSE5-MCS plasmid has a unique *PvuII* site in the MCS. Digest with *PvuII* to linearize and run on an agarose gel or on an E-Gel 0.8% agarose to confirm digestion.

13| Dephosphorylate the targeted fUSE5-MCS plasmid vector by using phosphatase alkaline according to the manufacturer's instructions.

▲ CRITICAL STEP It is recommended to dephosphorylate before ligation to reduce background as the fUSE5-MCS plasmid autoligates.

14| Ligate the ITR-flanked transgene cassette into the *PvuII*-linearized fUSE5-MCS plasmid for 4 h at 23 °C or 24 h overnight at 16 °C using T4 DNA ligase (Fig. 1).

? TROUBLESHOOTING

15| Digestion with *PvuII* generates blunt ends. Linkers containing recognition sequences of enzymes can be added to the *PvuII*-recovered ITR-flanked cassette to produce compatible cohesive ends.

Linkers to *BglII*, *HindIII*, *PstI*, *SacI* and *XhoI* can be used. After determining which restriction site is most appropriate for the construction, add the corresponding restriction enzyme to digest the linkers flanking the ITR transgene cassette. Ligate into the compatible cohesive restriction sites (*BglII*, *HindIII*, *PstI*, *SacI* and *XhoI*) of the MCS of the fUSE5-MCS plasmid.

? TROUBLESHOOTING

16| Use 2 μ l of the ligation product to transform MC1061 or XL1-Blue MR bacteria according to the manufacturer's instructions. Plate bacteria on LB-tetracycline and grow overnight at 37 °C for 24 h.

17| Pick ten colonies, grow overnight in 5 ml LB and purify the plasmid DNA by using a QIAprep miniprep kit protocol for low-copy plasmids. Identify the positive clones by enzymatic restriction digestions.

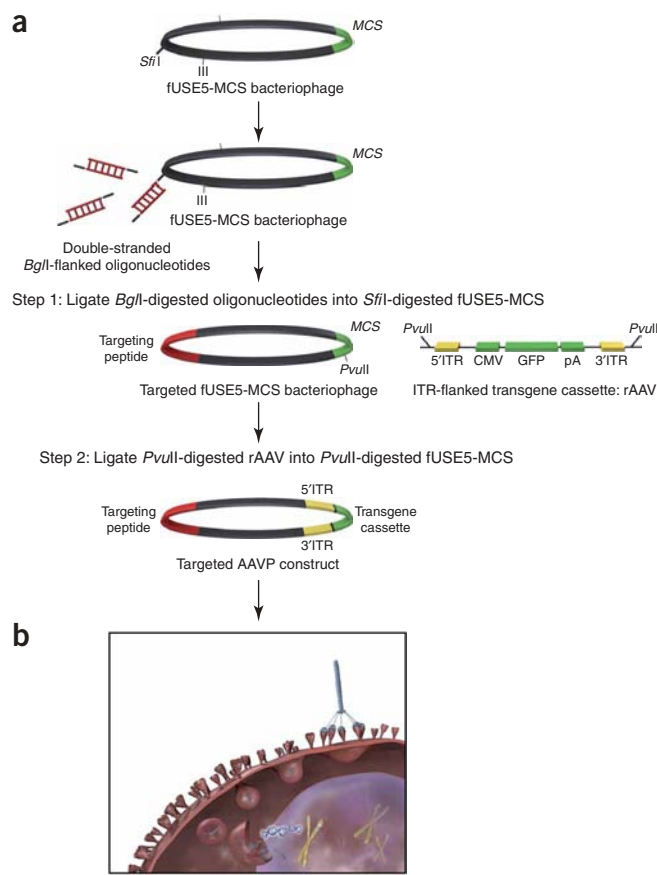


Figure 1 | Targeted AAV vectors. **(a)** Cloning scheme for generation of targeted AAVP and control vectors. The most convenient procedure is to first clone the *BglII*-digested oligonucleotide sequence corresponding to the targeting peptide within the *SfiI* site of the gene for the pIII coat protein. Next, the *PvuII*-digested ITR-flanking transgene cassette (rAAV) is cloned into the *PvuII* site in the MCS of the targeted fUSE5-MCS plasmid or in the cohesive restriction sites after addition of the corresponding linkers. **(b)** Binding of the targeted AAVP particle to a specific cell-surface receptor in the target tissue and internalization after systemic administration. Alternative cloning approaches are discussed in the text.

18| Transgene expression can be analyzed at this stage from the AAVP plasmids generated to confirm that the ITR-flanked transgene cassette is functional when inserted into the phage genome (in the context of AAVP). Therefore, transfect human embryonic kidney (HEK293) cells with the AAVP DNA plasmids by using the Fugene transfection reagent (Roche). Different experimental approaches, such as western blots or immunostainings, can be used to detect transgene expression depending on the gene of interest. For reporter *GFP*-, *β-galactosidase*- or *luciferase*-containing cassettes, expression can be analyzed as described in detail in Step 31.

Production, purification and titration of AAVP particles

19| AAVP particles can be amplified either by growing MC1061 colonies (option A) or by infecting and growing K91Kan cells (option B). Following amplification, AAVP particles are isolated and purified from the culture supernatant following a modified phage purification protocol^{30,32} by using the steps given below. It is important to note that option A is faster because *E. coli* MC1061 can be used to generate AAVP constructs. This strategy offers the advantage to directly grow positive clones to produce phage particles and to skip the infection step needed for option B. However, *E. coli* K91Kan (option B) are pilus-positive F⁺ bacteria and can therefore be infected by the newly produced phage particles during the overnight growth; this phenomenon will result in higher titers compared to MC1061 (option A), which are F⁻ bacteria.

(A) Growth of MC1061 colonies

(i) Amplify AAVP particles directly by growing the MC1061 colonies in LB plus tetracycline overnight at 37 °C.

(B) Infection and growth of K91Kan cells

(i) Incubate 1 ml of growing K91Kan *E. coli* bacteria with 10¹⁰ TU of AAVP for 1 h at room temperature in TB medium. Then, grow in 500 ml at 37 °C in the presence of tetracycline and kanamycin.

20| After overnight growth, centrifuge cultures at 6,000g for 20 min at 4 °C and collect the supernatant. Repeat centrifugation to remove residual bacterial debris.

21| Add PEG/NaCl (15% of the supernatant volume) solution to the supernatant to precipitate the AAVP phage particles. Incubate for 2 h on ice.

22| Centrifuge suspension at 10,000g for 30 min at 4 °C. A white pellet should be obtained. Discard the supernatant and centrifuge again for 10 min. Carefully decant the supernatant.

23| Resuspend the AAVP pellet in 10 ml of sterile PBS with agitation at 37°C for 30 min.

24| Repeat the precipitation with PEG/NaCl (15% of the supernatant volume) solution for 30 min on ice. Then, centrifuge at 14,000g for 30 min at 4 °C and resuspend in an adequate volume of PBS depending on the size of the pellet.

25| Transfer the solution to an Eppendorf tube, centrifuge at ~13,000g for 10 min at room temperature, transfer to a new tube and recentrifuge to remove residual bacteria and debris.

26| Filter the resulting supernatant containing the AAVP particles in suspension through a 0.45-μm filter. Then, titrate by infection of K91Kan bacteria for 20 min at room temperature and plaque assay according to the standard protocols^{30,32}. The AAVP titers are expressed as bacterial TUs per μl. Also, one must keep in mind that bacterial TU and multiplicity of infection are entirely different entities and should not be confused with one another.

▲ CRITICAL STEP *E. coli* K91Kan bacteria infection for more than 20 min might generate higher titers due to the newly produced AAVP particles. When comparing two different construct versions of AAVP for transduction efficiency, it is recommended to titrate the preparations side by side to ensure that same doses are compared. Indeed, the titers may vary from one AAVP version to another, depending on the ligand used, the size of the transgene of interest and size of the AAV mammalian cassette. These parameters can affect the coating of the virus in host bacteria during production. Viability of bacteria also plays a role, and it is recommended to infect a log-phase growing bacteria with an optical density ranging between 1.6 and 2.0 at a wavelength of 600 nm (OD₆₀₀).

■ PAUSE POINT AAVP titers are relatively stable and the preparations can be stored at 4 °C for long periods of time (several months) without any significant decrease in the titers. For longer storage times, one should check the titer of the preparation before use.

? TROUBLESHOOTING

Transduction of mammalian cells in culture by targeted AAVP vector and specific inhibition by using synthetic peptides—day 1: cell seeding

27| To transduce mammalian cells by targeted AAVP, it is recommended to incubate at least 10⁶ AAVP TUs per cell. Transduction can be performed in any tissue culture dish or flask; however, as an initial experiment to confirm transduction of mammalian cells, it is recommended to work with a 24-well plate to avoid the use of large amounts of AAVP. Therefore, seed 4 × 10⁴ cells in each well of the 24-well plate in a final volume of 0.5 ml of complete medium. Incubate overnight at 37 °C.

PROTOCOL

▲ CRITICAL STEP Factors such as concentration of cells in the edge of the well can affect the efficiency of transduction. Therefore, after seeding, observe the cells under the microscope to determine whether the cells are concentrated in the edge. Then to solve this problem, gently tilt or rock the plates to move the cells from the edge, until they are homogeneously distributed.

28| Analyze the efficiency of transduction of the cell line *in vitro* for each targeted AAVP. This can be carried out using a *GFP* reporter gene, as well as other reporter genes (e.g., *luciferase*, β -galactosidase). The *thymidine kinase* of herpes simplex virus type I (*HSV1-tk*) can also be used as a reporter gene^{37,38}. Note that transduction with AAVP particles is an approach different from transfection using a naked plasmid containing a reporter cassette. Transfection with naked plasmid DNA is a general, nonspecific strategy aimed at introducing naked DNA into cells, with transgene expression starting after a few hours. However, transduction with a targeted AAVP virus is designed to transduce a specific cell line expressing a specific receptor. It is a process that occurs via a ligand-directed mechanism by binding of the targeting ligand displayed on AAVP virus to its specific receptor on the cell surface. Escape of AAVP from endosomes, the uncoating of the virus and conversion of single- to double-stranded DNA (transcriptionally active) do take time. This causes a delayed initiation of transgene expression from AAVP, starting at day 3 and peaking 7–10 days later. Thus, plasmid transfection and transduction with AAVP are two distinct strategies with different experimental aims. The choice of the cell line will depend on the ligand used and expression of the corresponding receptor on the cell surface. Thus, efficiency of transduction will vary from one cell line to another. For example, HEK293 cells or KS1767 Kaposi sarcoma cells highly express α_v -integrin receptors^{1,27} and are suitable cell lines to use for transduction by AAVP displaying the α_v integrin-binding peptides.

Day 2: targeted AAVP infection

29| When cells are 50–60% confluent, they are ready for infection. Incubate the cells with the AAVP vectors at 10^6 TU per cell in a 0.2 ml total volume of tissue culture medium without serum at 37 °C for 4 h. Manually tilt after 30 min, then continue to gently tilt every 15 min, during incubation.

▲ CRITICAL STEP Incubation in the presence of serum markedly decreases the transduction efficiency of RGD-4C-targeted AAVP vector. Serum-mediated decrease of transduction efficiency has already been reported for other gene delivery vectors such as adenoviral vectors or liposomes and for plasmid transfection procedures such as lipofection^{39,40}. Moreover, groups that used RGD-targeted adenoviral vectors reported infection of cells *in vitro* in the absence of serum⁴¹. We have not tested AAVP displaying other ligands.

30| After 4 h of transduction, add 0.3 ml of 10% serum-supplemented medium to each well to have a final volume of 0.5 ml. Incubate the cells at 37 °C and renew the medium every 2 days.

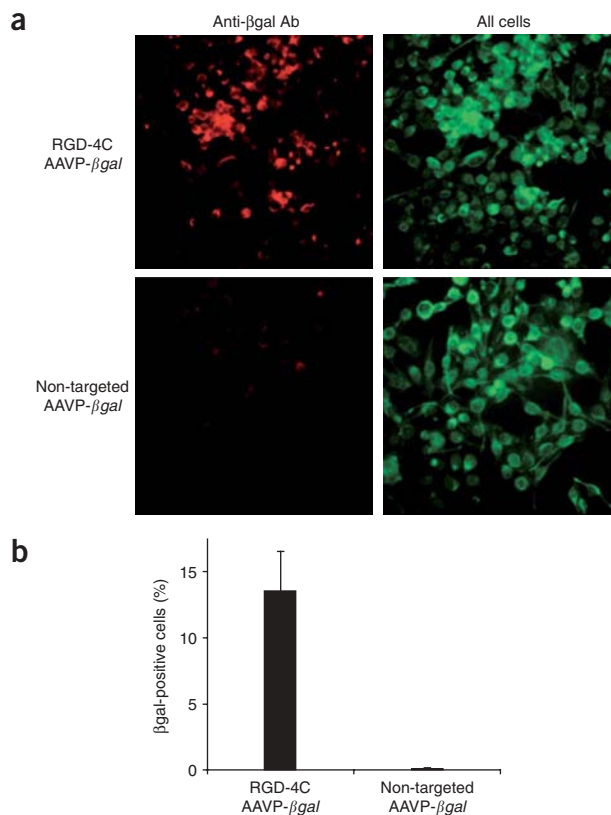


Figure 2 | *In vitro* mammalian cell transduction with targeted AAVP particles. (a) MDA-MB-435 breast tumor cells^{27,29} were incubated with either targeted RGD-4C AAVP-βgal displaying the α_v -integrin binding cyclic CDCRGDCFC peptide (termed RGD-4C)³¹ or non-targeted AAVP-βgal as a control. βgal expression was evaluated by using an anti-βgal antibody (Sigma). The left panel shows only Texas red-positive cells; the right panel shows the total number of cells in identical fields (green fluorescence). (b) Quantitative analysis of cell transduction by targeted or control AAVP. AAVP vectors were incubated with tumor cells as described above. An anti-βgal antibody was used for staining; gene expression was detected by immunofluorescence and results are expressed as percentage of βgal-positive cells. In each case, s.e.m. was calculated after counting ten fields under the microscope in three independent experiments.

BOX 1 | RESCUE OF rAAV FROM AAVP-TRANSDUCED CELLS

This step is performed to verify the integrity of AAVITRs and their functional ability to rescue a rAAV.

Four days after AAVP transduction, transduced cells are transfected with 170 ng of the rep/cap encoding plasmid pXX2⁴³ or 500 ng of pDsRed2 (Clontech) as a transfection plasmid control. The cells are then superinfected with wild-type adenovirus at an MOI of 10. Seven days after the initial AAVP transduction, the cells are harvested, freeze/thawed and the adenovirus heat-inactivated by treatment at 50 °C for 20 min. The supernatants containing the rescued rAAV are then used to infect new cells

BOX 2 | TRANSGENE EXPRESSION AND THERAPEUTIC EFFICACY OF AAVP IN MOUSE MODELS *IN VIVO* AFTER SYSTEMIC ADMINISTRATION

A series of increasing vector doses should be tested, starting at 10^{10} TU per administration until a maximum expression of the transgene in the target tissue is obtained. Transfer the AAVP dose to be administered per mouse into a new tube and adjust to ~ 0.2 ml with PBS. Use a U-100 28 G1/2 insulin syringe to inject a total of 0.2 ml into the tail vein. To perform this, one may choose to anesthetize the mice with Avertin^{27, 44} via intraperitoneal injection and warm the tail of the mouse before intravenous injection

Perform a real-time transgene expression analysis, for each AAVP dose level, at different time point after vector administration starting at day 3. When targeting tumor tissue, it is important to avoid large necrotic tumor as this will cause nonspecific AAVP particle trapping. In tumor transduction experiments, cohorts of mice with size-matched tumors are treated. To analyze the efficiency of gene expression by targeted AAVP *in vivo*, it is recommended to start with reporter genes and use more than one (e.g., GFP, β -galactosidase, luciferase, HSV1-tk) (see **Box 3**) Specificity of *in vivo* transduction can be assessed using synthetic targeting peptides that are able to block transduction. Therefore, animals are first intravenously injected with the peptides 15 min before AAVP administration. Negative control peptides can be either scrambled or mutated versions of the targeting peptide

The BLI of luciferase experiments will determine the adequate targeted AAVP dose per animal. Therefore, when assessing the therapeutic efficacy of targeted AAVP bearing a therapeutic gene in tumor-bearing mice, the dose of targeted AAVP that results in the maximum of transgene expression in the tumor tissue, without toxicity, should be administered. Monitor tumor growth daily. In the case of using HSV1-tk/ganciclovir (GCV) “suicide gene therapy,” treatment with GCV should be initiated at a time point that corresponds to a maximum level of gene expression in the target tissue *in vivo*, and should be administered intraperitoneally at $80 \text{ mg kg}^{-1} \text{ day}^{-1}$

31| Analyze the cells for transgene expression at 48–72 h after transduction. A number of options are available for this, depending on which reporter gene system is used: for example, GFP (option A), β -galactosidase (option B) or luciferase (option C). Maximum levels of gene expression are usually reached by 7–10 days (**Fig. 2**). At this stage, as we previously reported¹, the transduced cells can be used to perform rescue experiments to verify the ITR structure integrity and functional ability to rescue rAAV particles from transduced cells (see **Box 1**).

(A) GFP detection

(i) For GFP detection, analyze the cells by FACS or count cells by using a standard fluorescence microscope.

(B) Detection of β -galactosidase expression

(i) Detection of β -galactosidase expression can be performed by X-gal staining⁴². β -Gal activity in cell lysates can also be detected by the Galacto-Star chemiluminescent reporter gene system (Tropix).

(C) Detection of Luciferase expression

(i) Detect luciferase expression *in vitro* by incubating the cells with the *D*-luciferin substrate. Aspirate the medium from the cultured cells and add *D*-luciferin ($150 \mu\text{g ml}^{-1}$ final). Monitor expression with a luminometer, a scintillation counter or a BLI system.

32| After maximum gene expression is obtained, split the transduced cells.

▲ CRITICAL STEP Splitting the cells before maximum gene expression is achieved and transferring them into a larger tissue culture dish will stimulate cells to divide and cause dilution of transduced cells within a large background population of non-transduced cells. To circumvent this problem, use a specific selection genetic marker to allow selection of only transduced cells.

33| To determine whether the AAVP particle is transfecting via the correct receptor, carry out a peptide inhibition experiment. For peptide inhibition experiments, seed the cells at 4×10^4 cells per well as in Step 27 and incubate with either 1 mg ml^{-1} of

BOX 3 | DETECTION OF TRANSGENE EXPRESSION *IN VIVO* AFTER SYSTEMIC ADMINISTRATION OF AAVP

To detect transgene expression *in vivo*, a number of options are available depending on which reporter gene system is used. For example:

1. To detect β -galactosidase expression, surgically harvest the tumors or other target tissues from mice under deep anesthesia. β -galactosidase expression is detected in tissue sections by an anti- β -galactosidase antibody and a peroxidase-based immunodetection kit (Vector Labs). For *in vivo* experiments involving tissue extracts, β -galactosidase activity in the tissues is detected by a chemiluminescent assay system (Tropix)
2. To detect GFP expression, anesthetized mice are first systemically perfused with PBS containing 4% paraformaldehyde. Tissues are harvested and processed for GFP immunostaining as previously described¹ (**Fig. 3a**)
3. Luciferase expression can be monitored directly *in vivo* in living mice by BLI (**Fig. 3b**). Each mouse is injected intraperitoneally with a *D*-luciferin solution (150 mg kg^{-1} in PBS) 10 min before imaging. Luciferase expression can also be confirmed by directly imaging the excised-target tissues
4. Detection of HSV1-tk transgene expression by PET-based imaging is detailed in the companion manuscript⁴⁵

PROTOCOL

the specific targeting or control peptides for 30 min at 37 °C. After 30 min, wash the cells and add 10⁶ TU of AAVP per cell for 4 h in serum-free medium as in Step 29. After incubation, add medium supplemented with 10% FCS. Negative control peptide (scrambled and/or mutant sequence) versions of the targeting peptide can be included. Cells are analyzed for transgene expression similar to conventionally transduced mammalian cells (Step 31).

***In vivo* transduction of target tissues by AAVP vector after systemic administration**

34 | Analysis of transgene expression *in vivo* was optimized for AAVP targeting systemic gene delivery to murine and human tumors established in mice, but can be applied to target normal tissues or perhaps other pathologically affected tissues. It is important to determine the suitable targeted AAVP dose to be administered to the animal to achieve an efficient and specific transgene expression within the target tissue. Indeed, each target tissue may require a different dose to achieve transduction and transgene expression *in vivo*, depending on the level of expression of the targeted receptor, the ligand used and promoter activity in the tissue. Thus, it is recommended to test different doses and analyze transgene expression over a time course to determine initiation and maximal expression (see **Boxes 2** and **3**).

? TROUBLESHOOTING

? TROUBLESHOOTING

Troubleshooting advice can be found in **Table 2**.

TABLE 2 | Troubleshooting table.

Step	Problem	Solution
Genetic modifications		
5	<i>Sfi</i> I digestion generates strong star activity in the phage DNA	Use as few units of <i>Sfi</i> I as possible to get a complete digestion. This avoids overdigestion and reduces the final glycerol concentration in the reaction
14	Low efficiency of ligation is caused by autoligation of the vector or by non-digested plasmids	Analyze the complete digestion of the vector by agarose gel. Dephosphorylate and use as little as possible of the vector plasmid
15	Excess of linkers ligate to the vector	Excess linkers are best removed by agarose gel electrophoresis and subsequent gel extraction and purification. Avoid a spinning column
Particle production and purification		
26	Low titers of AAVP preparations	Check bacterial viability. Repeat infection of 1 ml of K91Kan <i>E. coli</i> bacteria with the new AAVP preparation for 1 h (10 µl at least). Then grow in 500 ml for up to 16 h
Targeted gene expression		
Boxes 2 and 3	Efficiency of transduction is dependent on the expression of the receptor within the target tissue and its accessibility	Whenever possible, one can increase the expression of the target cell surface receptor by biochemical or genetic methods
		Use the AAVP dose that achieves maximum level of transgene expression in the tumors
	Efficacy of therapy can be heterogeneous from one experiment to another or among different individuals	Use size-matched tumors and at least seven animals per group. When using HSV1-tk/GCV therapy, GCV efficiency is not only dependent on HSV1-tk transgene expression, but also on the rate of tumor growth

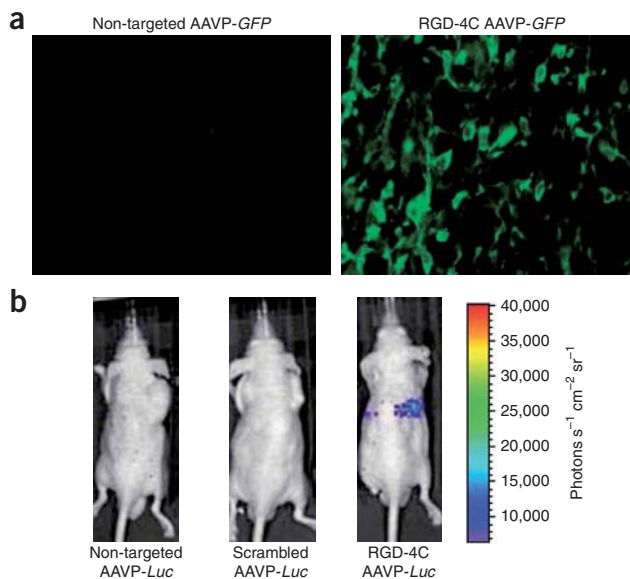


Figure 3 | *In vivo* transduction and molecular-genetic imaging of tumors in mice after systemic delivery of targeted AAVP. Targeted RGD-4C AAVP vectors or controls are intravenously administered to tumor-bearing mice. (a) Immunofluorescence analysis of GFP expression in tumors at 1 week after intravenous administration of RGD-4C AAVP-GFP or control non-targeted AAVP-GFP. (b) BLI of luciferase expression in living mice at 1 week after intravenous delivery of RGD-4C AAVP-Luc carrying the gene for firefly luciferase or AAVP control (non-targeted AAVP) or AAVP control (displaying CDCGFDCRC, a scrambled RGD-4C version).

ANTICIPATED RESULTS

The protocols described here should result in successful cloning and application of AAVP-based vectors. AAVP preparations of $1-5 \times 10^{10}$ TU μl^{-1} are routinely obtained and are consistent with the titers generated with the parental targeted phage. This shows that insertion of a mammalian transgene cassette in the bacteriophage genome does not affect vector production in bacteria. Transgene expression in cells in culture starts at 48–72 h after incubation with the targeted AAVP vector and reaches maximum levels by days 7–10 (Fig. 2). *In vivo*, transgene expression is detectable in target tissues at day 3 after intravenous delivery of targeted AAVP vectors, then it increases gradually until days 7–10 (Fig. 3). We previously followed transgene expression until day 10 post-AAVP administration¹; if required, further reporter detection may be accomplished. For long-term detection of transgene expression, real-time RT-PCR may be used. In recent work (unpublished observation), we have followed transgene expression using BLI of luciferase in a tumor model for 5–6 weeks. Transgene expression started at day 3 after vector delivery and was still detectable at adequate levels upon experiment termination due to tumor burden.

ACKNOWLEDGMENTS We thank Marco Arap, David Bier, Carlotta Cavazos, Carol M. Johnston, Erkki Koivunen, Darwin Lee, Frank C. Marini, Bradley H. Restel, Karen Schmidt, Yan Sun and Claudia Zompetta for advice and assistance. This work was funded by grants from the NIH (including the SPORE) and DOD (including the IMPACT) and by awards from the Gillson-Longenbaugh, the Keck Foundation and the Prostate Cancer Foundation (to R.P. and W.A.). A.H. received a Léon Fredericq award.

COMPETING INTERESTS STATEMENT The authors declare that they have no competing financial interests.

Published online at <http://www.natureprotocols.com>
 Reprints and permissions information is available online at <http://npg.nature.com/reprintsandpermissions>

1. Hajitou, A. *et al.* A hybrid vector for ligand-directed tumor targeting and molecular imaging. *Cell* **125**, 385–398 (2006).
2. Watkins, S.J., Mesyanzhinov, V.V., Kurochkina, L.P. & Hawkins, R.E. The ‘adenobody’ approach to viral targeting: specific and enhanced adenoviral gene delivery. *Gene Ther.* **4**, 1004–1012 (1997).
3. Wickham, T.J. *et al.* Targeted adenovirus-mediated gene delivery to T cells via CD3. *J. Virol.* **71**, 7663–7669 (1997).
4. Miller, C.R. *et al.* Differential susceptibility of primary and established human glioma cells to adenovirus infection: targeting via the epidermal growth factor receptor achieves fiber receptor-independent gene transfer. *Cancer Res.* **58**, 5738–5748 (1998).
5. Martin, F. *et al.* Retrovirus targeting by tropism restriction to melanoma cells. *J. Virol.* **73**, 6923–6929 (1999).
6. Girod, A. *et al.* Genetic capsid modifications allow efficient re-targeting of adeno-associated virus type 2. *Nat. Med.* **5**, 1052–1056 (1999).
7. Vigne, E. *et al.* RGD inclusion in the hexon monomer provides adenovirus type 5-based vectors with a fiber knob-independent pathway for infection. *J. Virol.* **73**, 5156–5161 (1999).
8. Reynolds, P.N. *et al.* A targetable injectable adenoviral vector for selective gene delivery to pulmonary endothelium *in vivo*. *Mol. Ther.* **2**, 562–578 (2000).
9. Wickham, T.J. Targeting adenovirus. *Gene Ther.* **7**, 110–114 (2000).
10. Trepel, M., Grifman, M., Weitzman, M.D. & Pasqualini, R. Molecular adaptors for vascular-targeted adenoviral gene delivery. *Hum. Gene Ther.* **11**, 1971–1981 (2000).
11. Trepel, M., Arap, W. & Pasqualini, R. Exploring vascular heterogeneity for gene therapy targeting. *Gene Ther.* **7**, 2059–2060 (2000).
12. Müller, O.J. *et al.* Random peptide libraries displayed on adeno-associated virus to select for targeted gene therapy vectors. *Nat. Biotechnol.* **21**, 1040–1046 (2003).
13. Lieber, A. AAV display-homing in on the target. *Nat. Biotechnol.* **21**, 1011–1013 (2003).
14. Barrow, P.A. & Soothill, J.S. Bacteriophage therapy and prophylaxis: rediscovery and renewed assessment of potential. *Trends Microbiol.* **5**, 268–271 (1997).
15. Barbas III, C.F., Burton, D.R., Scott, J.K. & Silverman, G.J. *Phage Display: A Laboratory Manual* (Cold Spring Harbor Press, Cold Spring Harbor, NY, 2001).
16. Ivanenkov, V.V., Felici, F. & Menon, A.G. Targeted delivery of multivalent phage display vectors into mammalian cells. *Biochim. Biophys. Acta* **1448**, 463–472 (1999).
17. Larocca, D. *et al.* Gene transfer to mammalian cells using genetically targeted filamentous bacteriophage. *FASEB J.* **13**, 727–734 (1999).
18. Poul, M.A. & Marks, J.D. Targeted gene delivery to mammalian cells by filamentous bacteriophage. *J. Mol. Biol.* **288**, 203–211 (1999).
19. Sergeeva, A., Kolonin, M.G., Mollidre, J.J., Pasqualini, R. & Arap, W. Display technologies: application for the discovery of drug and gene delivery agents. *Adv. Drug Deliv. Rev.* **58**, 1622–1654 (2006).
20. Monaci, P., Urbanelli, L. & Fontana, L. Phage as gene delivery vectors. *Curr. Opin. Mol. Ther.* **3**, 159–169 (2001).

21. <http://www.cfsan.fda.gov/~dms/opabacqa.html>.
22. Arap, W. *et al.* Steps toward mapping the human vasculature by phage display. *Nat. Med.* **8**, 121–127 (2002).
23. Pentz, R.D. *et al.* Ethics guidelines for research with the recently dead. *Nat. Med.* **11**, 1145–1149 (2005).
24. Krag, D.N. *et al.* Selection of tumor-binding ligands in cancer patients with phage display libraries. *Cancer Res.* **66**, 7724–7733 (2006).
25. Koivunen, E. *et al.* Tumor targeting with a selective gelatinase inhibitor. *Nat. Biotechnol.* **17**, 768–774 (1999).
26. Pasqualini, R., Koivunen, E. & Ruoslahti, E. αv integrins as receptors for tumor targeting by circulating ligands. *Nat. Biotechnol.* **15**, 542–546 (1997).
27. Arap, W., Pasqualini, R. & Ruoslahti, E. Cancer treatment by targeted drug delivery to tumor vasculature in a mouse model. *Science* **279**, 377–380 (1998).
28. Kolonin, M.G., Saha, P.K., Chan, L., Pasqualini, R. & Arap, W. Reversal of obesity by targeted ablation of adipose tissue. *Nat. Med.* **10**, 625–632 (2004).
29. Ellerby, H.M. *et al.* Anti-cancer activity of targeted pro-apoptotic peptides. *Nat. Med.* **5**, 1032–1038 (1999).
30. Pasqualini, R., Arap, W., Rajotte, D. & Ruoslahti, E. *In vivo* phage display. in *Phage Display: A Laboratory Manual* (eds. Barbas III, C.F., Burton, D.R., Scott, J.K. & Silverman, G.J.) Ch. 22, 1–24 (Cold Spring Harbor Laboratory Press, Cold Spring Harbor, NY, 2000).
31. Koivunen, E., Wang, B. & Ruoslahti, E. Phage libraries displaying cyclic peptides with different ring sizes: ligand specificities of the RGD-directed integrins. *BioTechnology* **3**, 265–270 (1995).
32. Smith, G.P. & Scott, J.K. Libraries of peptides and proteins displayed on filamentous phage. *Meth. Enzymol.* **217**, 228–257 (1993).
33. Parmely, S.F. & Smith, G.P. Antibody-selectable filamentous fd phage vectors: affinity purification of target genes. *Gene* **73**, 305–318 (1988).
34. Rajotte, D. *et al.* Molecular heterogeneity of the vascular endothelium revealed by *in vivo* phage display. *J. Clin. Invest.* **102**, 430–437 (1998).
35. Rajotte, D. & Ruoslahti, E. Membrane dipeptidase is the receptor for a lung-targeting peptide identified by *in vivo* phage display. *J. Biol. Chem.* **274**, 11593–11598 (1999).
36. <http://www.biosci.missouri.edu/smithGP/PhageDisplayWebsite/PhageDisplayWebsiteIndex.html>.
37. Tjuvajev, J.G. *et al.* Imaging herpes virus thymidine kinase gene transfer and expression by positron emission tomography. *Cancer Res.* **58**, 4333–4341 (1998).
38. Tjuvajev, J.G. *et al.* Imaging adenoviral-mediated herpes virus thymidine kinase gene transfer and expression *in vivo*. *Cancer Res.* **59**, 5186–5193 (1999).
39. Serikawa, T., Kikuchi, A., Sugaya, S., Suzuki, N., Kikuchi, H. & Tanaka, K. *In vitro* and *in vivo* evaluation of novel cationic liposomes utilized for cancer gene therapy. *J. Control Rel.* **113**, 255–260 (2006).
40. Abe, A., Miyano, A. & Friedmann, T. Polybrene increases the efficiency of gene transfer by lipofection. *Gene Ther.* **5**, 708–711 (1998).
41. Okada, Y., Okada, N., Mizuguchi, H., Hayakawa, T., Nakagawa, S. & Mayumi, T. Transcriptional targeting of RGD fiber-mutant adenovirus vectors can improve the safety of suicide gene therapy for murine melanoma. *Cancer Gene Ther.* **12**, 72–83 (2005).
42. Arap, M. *et al.* Model of unidirectional transluminal gene transfer. *Mol. Ther.* **9**, 305–310 (2004).
43. Xiao, X., Li, J. & Samulski, R.J. Production of high-titer recombinant adeno-associated virus vectors in the absence of helper adenovirus. *J. Virol.* **72**, 2224–2232 (1998).
44. Papaioannou, V.E. & Fox, J.G. Efficacy of tribromoethanol anesthesia in mice. *Lab. Anim. Sci.* **43**, 189–192 (1993).
45. Soghomonyan, S. *et al.* Molecular PET imaging of HSV1-tk reporter gene expression by using ¹⁸F-FAU. *Nat. Protoc.* doi: 10.1038/nprot.2007.49 (2007).



Impaired angiogenesis in aminopeptidase N-null mice

Roberto Rangel, Yan Sun, Liliana Guzman-Rojas, Michael G. Ozawa, Jessica Sun, Ricardo J. Giordano, Carolyn S. Van Pelt, Peggy T. Tinkey, Richard R. Behringer, Richard L. Sidman, Wadih Arap, and Renata Pasqualini

PNAS 2007;104;4588-4593; originally published online Mar 7, 2007;
doi:10.1073/pnas.0611653104

This information is current as of March 2007.

Online Information & Services	High-resolution figures, a citation map, links to PubMed and Google Scholar, etc., can be found at: www.pnas.org/cgi/content/full/104/11/4588
Supplementary Material	Supplementary material can be found at: www.pnas.org/cgi/content/full/0611653104/DC1
References	This article cites 38 articles, 15 of which you can access for free at: www.pnas.org/cgi/content/full/104/11/4588#BIBL This article has been cited by other articles: www.pnas.org/cgi/content/full/104/11/4588#otherarticles
E-mail Alerts	Receive free email alerts when new articles cite this article - sign up in the box at the top right corner of the article or click here .
Rights & Permissions	To reproduce this article in part (figures, tables) or in entirety, see: www.pnas.org/misc/rightperm.shtml
Reprints	To order reprints, see: www.pnas.org/misc/reprints.shtml

Notes:

Impaired angiogenesis in aminopeptidase N-null mice

Roberto Rangel*, Yan Sun*, Liliana Guzman-Rojas*, Michael G. Ozawa*, Jessica Sun*, Ricardo J. Giordano*, Carolyn S. Van Pelt†, Peggy T. Tinkey†, Richard R. Behringer‡, Richard L. Sidman§¶, Wadih Arap*¶||, and Renata Pasqualini*¶||

Departments of *Genitourinary Medical Oncology, †Cancer Biology, ‡Molecular Genetics, and †Veterinary Medicine and Surgery, University of Texas M.D. Anderson Cancer Center, 1515 Holcombe Boulevard, Houston, TX 77030; and §Harvard Medical School and Department of Neurology, Beth Israel Deaconess Medical Center, Harvard Institutes of Medicine, 77 Avenue Louis Pasteur, Boston, MA 02115

Contributed by Richard L. Sidman, December 29, 2006 (sent for review December 21, 2006)

Aminopeptidase N (APN, CD13; EC 3.4.11.2) is a transmembrane metalloprotease with several functions, depending on the cell type and tissue environment. In tumor vasculature, APN is overexpressed in the endothelium and promotes angiogenesis. However, there have been no reports of *in vivo* inactivation of the APN gene to validate these findings. Here we evaluated, by targeted disruption of the APN gene, whether APN participates in blood vessel formation and function under normal conditions. Surprisingly, APN-null mice developed with no gross or histological abnormalities. Standard neurological, cardiovascular, metabolic, locomotor, and hematological studies revealed no alterations. Nonetheless, in oxygen-induced retinopathy experiments, APN-deficient mice had a marked and dose-dependent deficiency of the expected retinal neovascularization. Moreover, gelfoams embedded with growth factors failed to induce functional blood vessel formation in APN-null mice. These findings establish that APN-null mice develop normally without physiological alterations and can undergo physiological angiogenesis but show a severely impaired angiogenic response under pathological conditions. Finally, in addition to vascular biology research, APN-null mice may be useful reagents in other medical fields such as malignant, cardiovascular, immunological, or infectious diseases.

CD13 | knockout mice | retinopathy | vasculogenesis

The aminopeptidases are a large family of proteolytic enzymes that affect protein maturation, degradation, and regulation (1, 2). Aminopeptidase N (APN) is a membrane-bound zinc-dependent metalloprotease originally identified as a surface marker in myeloid cells (3, 4). APN is widely distributed in many cell types, and its role in hydrolyzing unsubstituted N-terminal residues with neutral side chains varies in different locations. In the epithelium of the renal proximal tubule, APN cleaves its only known natural substrate, angiotensin (ang) III, to ang IV; in synaptic membranes, APN metabolizes enkephalins and endorphins; in the heart, it is an integral component of cardiac remodeling postmyocardial infarction (5–10); and in the respiratory system, APN is the cell surface receptor for certain human coronaviruses and potentially for the severe acute respiratory syndrome (SARS) virus (11–13). Additionally, APN functions in signal transduction, cell cycle control, and differentiation (14, 15).

We have developed an *in vivo* system by using ligand peptides displayed on the surface of phage to study organ- and tumor-specific vascular homing; this methodology enables the identification of vascular markers (16, 17). We have isolated phage displaying an asparagine-glycine-arginine (NGR)-containing peptide in a tumor-homing selection and have shown that these phage bind selectively to angiogenic blood vessels. When coupled to a cytotoxic drug (18) or fused to a proapoptotic peptide (19) or to tumor necrosis factor (20), NGR-targeted compounds were more effective and less toxic than the respective controls. The cell surface receptor for NGR-containing ligands was then shown to be APN (21). Of note, although a single gene encodes APN, specific phenotypic forms of APN (CD13) in angiogenic

vasculature relative to normal tissues further enhance the targeting attributes of the NGR motif (22).

To evaluate the effects of the APN gene on development and organ function, we produced a knockout mouse lacking APN. This has been technically challenging because of the incomplete genomic characterization and complex APN gene structure. Here we report the generation of an APN-null mouse by homologous recombination and a description of its phenotype. Despite its broad expression, the APN gene is not essential for development, because the null was not embryonically lethal and developed normally. Standard phenotype characterization revealed no differences between WT and APN-null mice. However, in a model of retinal neovascularization, APN-null mice had a significant decrease in blood vessel growth compared with WT. Moreover, gelfoam plug assays demonstrated a reduction in hemoglobin content within the plugs, indicating lack of a functional vasculature. Thus, although APN activity is not essential for embryonic and fetal development including *de novo* blood vessel formation (i.e., vasculogenesis) and normal adult function, it is critical for the pathological development of new blood vessels from existing blood vessels (i.e., angiogenesis) in disease.

Results

APN-Null Mouse Generation. Early attempts to isolate the APN gene have been problematic because of the absence of genomic clones in the 5' region of the gene. To overcome this limitation, a combined screening of 129S6/SvEv Tac BAC libraries and BLAST analysis served to obtain the complete sequence of the mouse APN gene in a C57BL/6 background. Indeed, previous reports on gene characterization revealed variation in restriction enzyme maps between different genetic backgrounds. Integrated Southern blot and bioinformatics revealed that the APN gene in C57BL/6 and 129Sv/Ev backgrounds possessed the same restriction enzyme map (data not shown). APN exon-intron boundary analysis showed that exon 5 contained the nucleotide sequence that encodes the zinc-binding domain. Thus, our strategy (Fig. 1) was to eliminate expression and enzymatic activity by replacing APN exons 1–6 (Fig. 1*a*). After mouse embryonic stem (ES) cell screening, we detected 3 of 600 ES cell clones that contained the APN mutant allele; mutant ES clones were injected into C57BL/6 blastocysts and produced a single

Author contributions: R.R., L.G.-R., M.G.O., R.J.G., R.R.B., R.L.S., W.A., and R.P. designed research; R.R., Y.S., L.G.-R., M.G.O., and R.J.G. performed research; R.R., L.G.-R., M.G.O., J.S., C.S.V.P., P.T.T., R.R.B., and R.L.S. contributed new reagents/analytic tools; R.R., Y.S., L.G.-R., M.G.O., J.S., R.J.G., C.S.V.P., P.T.T., R.R.B., R.L.S., W.A., and R.P. analyzed data; and R.R., M.G.O., R.L.S., W.A., and R.P. wrote the paper.

The authors declare no conflict of interest.

Freely available online through the PNAS open access option.

Abbreviations: APN, aminopeptidase N; ang, angiotensin; SARS, severe acute respiratory syndrome; ES, embryonic stem; APA, aminopeptidase A; Pn, postnatal day *n*.

¶To whom correspondence may be addressed. E-mail: richard.sidman@hms.harvard.edu, warap@mdanderson.org, or rpsqual@mdanderson.org.

This article contains supporting information online at www.pnas.org/cgi/content/full/0611653104/DC1.

© 2007 by The National Academy of Sciences of the USA

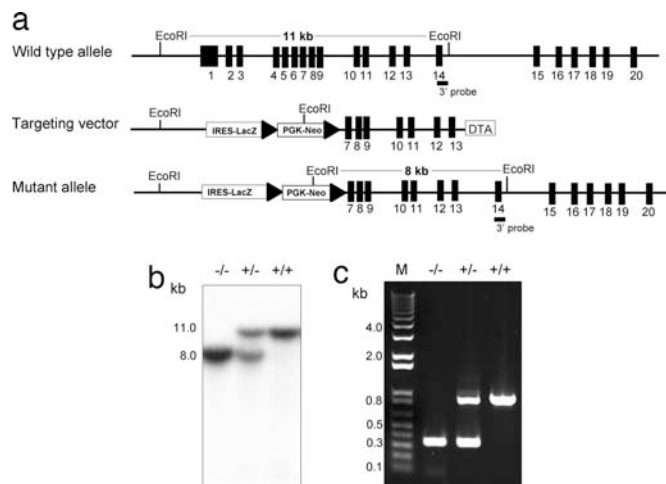


Fig. 1. Generation and characterization of the APN-null mouse. (a) Schema of the APN gene-targeting strategy. The APN gene contains 20 exons (black boxes); the 3' external probe is located in exon 14. The targeting vector contains a β -galactosidase transgene and a floxed neomycin resistant gene. (b) Southern blot of genomic DNA from WT (+/+), APN-heterozygous (+/-), and APN-null (-/-); the mutant allele (8 kb) and the WT allele (11 kb) are noted. The APN heterozygous contains both alleles. (c) PCR genotyping reveals unique products for WT (879-bp) and APN-null (320-bp) mice. The APN heterozygous contains both PCR products.

chimeric mouse, which was used for mating with C57BL/6 mice. After 5 mo, we detected the first germ-line transmission in a 129Sv/Ev-C57BL/6 genetic background. The first three generations of progeny were genotyped by either Southern blot (Fig. 1*b*) or PCR (Fig. 1*c*). Despite strong RNA expression during embryogenesis, Mendelian inheritance of the APN-null allele occurred [supporting information (SI) Fig. 8].

Inactivation of APN in the Null Mouse. APN expression was examined at the RNA and protein level, focusing initially on the nervous and renal systems, because APN is highly expressed in the pericytes associated with the brain endothelium and in the proximal tubules of the kidney. RT-PCR and immunohistochemical analysis showed a total absence of mRNA and protein in the brain and kidney of APN-null mice (Fig. 2). In contrast, WT mice displayed a strong expression of mRNA and protein in those organs. Similar results were observed in the spleen, liver, pancreas, intestine, and ovary (Fig. 3). Notably, a gene dosage

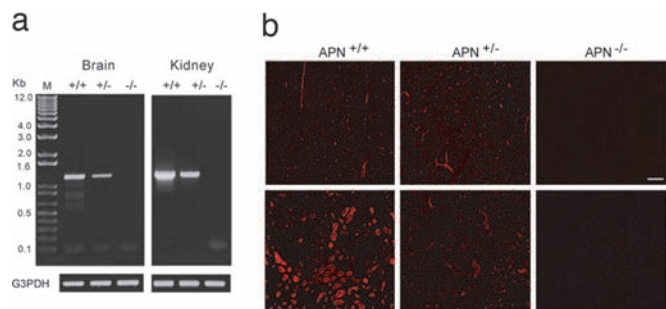


Fig. 2. Expression analysis of the APN-null mouse. (a) RT-PCR analysis of total RNA. The WT (+/+) and heterozygous (+/-) mice contain the 1.2-kb PCR product representing the APN mRNA transcript that is undetectable in the APN-null mouse (-/-). The G3PDH transcript served as a loading control. (b) Immunohistochemical analysis of the APN protein in brain (Upper) and kidney (Lower). APN immunoreactivity (red fluorescence) is detected in renal tubules and in pericytes within brain vasculature of WT and heterozygous mice but not in the APN-null mice (Right). (Scale bar, 100 μ m.)

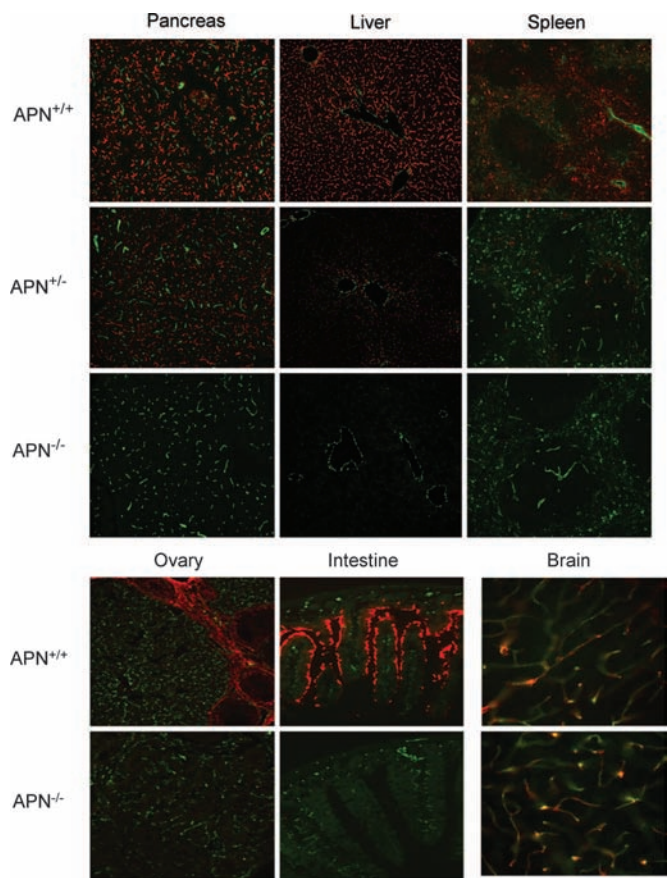


Fig. 3. Immunohistochemical analysis of APN and CD31. Colocalization studies in pancreas, liver, and spleen for APN (red fluorescence) and CD31 (green fluorescence) were performed in frozen tissue sections (Upper). The WT and APN-heterozygote mice contain dual fluorescence signals; in APN-null mice, only CD31 immunoreactivity is detected. Ovary and intestine were also evaluated (Lower Left). Brain was stained with anti-CD31 and -APA antibodies. The yellow fluorescence reflects the localization of both proteins in pericytes in brain vasculature (Lower Right).

effect was observed for the heterozygous animal (Figs. 2 and 3). Because aminopeptidase A (APA) is another member of the aminopeptidase family with similar expression patterns to that of APN (23), APA expression was examined as a surrogate to ensure that loss of APN did not affect normal tissue organization. Colocalization analysis between WT and the APN-null revealed no change in the expression profile of APA in brain pericytes despite the loss of APN (Fig. 3). These data support the genetic generation of a viable APN-null mouse.

Histopathological Studies in the APN-Null Mouse. A comprehensive panel of organs of 12-wk-old male and female mice was examined in H&E-stained sections. No structural differences were found between WT and APN-null mice (SI Fig. 9 *a-d*). Blood counts showed no differences in all parameters (SI Table 1), and serum chemistries indicated there were no significant electrolyte imbalances between WT and APN-null mice (SI Table 2). These results are consistent with full APN-null mouse viability.

Noninvasive Phenotypic Studies in the APN-Null Mouse. The function of APN appears to depend on its tissue localization. Thus, system functions (i.e., neurological, cardiovascular, metabolic, and locomotor) were compared to explore whether the deficiency of APN altered physiology (Fig. 4). First, activity tests were performed in an open field to determine any behavioral alterations

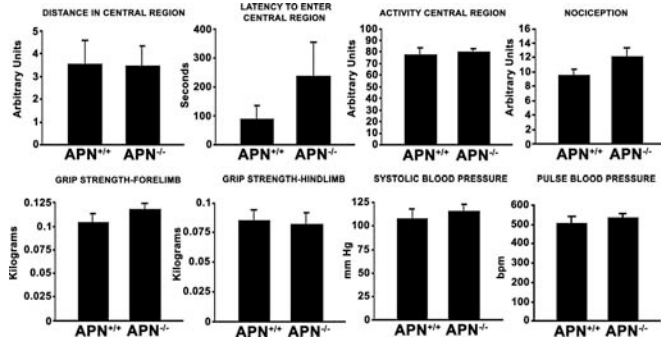


Fig. 4. Noninvasive phenotypic studies. Spontaneous locomotor activity in WT mice and APN-null littermates are represented as distance in central region, latency central region, and activity central region. Nociception was measured by using a hot-plate analgesia meter. Neuromuscular function was determined by grip strength of the forelimb and hindlimb. Pulse and blood pressure were measured by the tail-cuff method. Error bars indicate SEM of WT and APN-null mice ($n = 6$ per group).

in the APN-null mouse. Data were plotted for the time required for the mice to reach the central region, latency to enter it, and activity within that area of the field. No statistically significant differences in behavior were found. Next, neuromuscular function was assessed by muscle grip strength and showed no differences between the two groups. Finally, thermal and pain reflexes were assessed when the APN-null mouse footpad was placed against a heated surface; we noted a small increase in pain resistance when compared with the WT mouse (Fig. 4).

Noninvasive tail cuff measurements were used for blood pressure and pulse measurements. APN-null mice had normal baseline pulse and blood pressure (Fig. 4). Cardiovascular analysis by noninvasive unrestrained measurements revealed no statistical differences in baseline electrocardiogram heart rate and its variability or waveform intervals (SI Figs. 10 *a* and *b*). These data indicate that APN is not critical in regulation of cardiovascular function under normal conditions.

Body composition and whole-body metabolism served as surrogates for endocrine and renal function. Bone mineral density, content, and body fat content were measured by dual energy x-ray absorptiometry. No statistically significant differences between the two groups of mice were found (SI Fig. 11). Moreover, comprehensive in-cage monitoring was performed for O_2 uptake, CO_2 production, food and water intake, locomotor activity, and circadian patterns to assess total body metabolism and energy balance. Results revealed a trend toward reduction in food and water intake for the APN-null mouse, but the results did not reach statistical significance; all other measures were similar between the two groups (Fig. 5). Thus, under normal conditions, WT and APN-null mice have similar behavioral phenotypes and physiological regulation. Null female mice were fertile and carried normal numbers of progeny through full pregnancy and nursing phases.

Reduced Angiogenesis in the APN-Null Mouse. We next evaluated whether the APN-null mouse had a normal angiogenic response to hypoxic conditions. Neonatal mice were exposed to 75% oxygen between postnatal days (P)7–P12 and then returned to room air. By P18, retinal neovascularization is observed in WT mice; in contrast, histological examination of similarly treated APN-null mice revealed a marked reduction in the formation of new blood vessels at the retinal inner surface compared with the response in WT mice (Fig. 6). Consistently, an intermediate dose response was observed in the APN heterozygotes. Thus, the APN-null mouse has a severely reduced angiogenic response to hypoxic conditions.

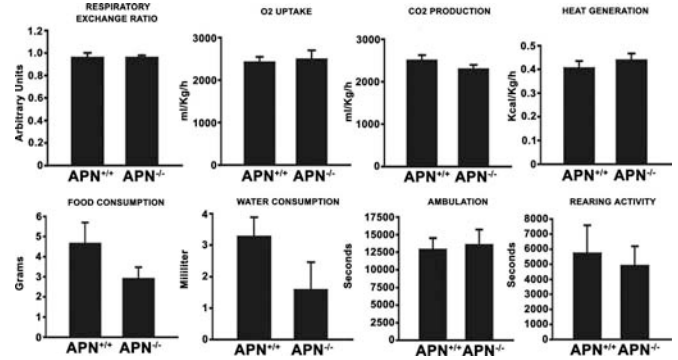


Fig. 5. Comprehensive in-cage monitoring system. The WT and APN-null mice littermates were examined for respiratory exchange ratio, oxygen uptake, and carbon dioxide production. Caloric intake and energy metabolism were measured for heat production, food, and water consumption. Ambulation and rearing activity were determined by using the comprehensive laboratory animal-monitoring system. Error bars indicate SEM of WT and APN-null mice ($n = 6$ per group).

Next, angiogenic responses to growth factors *in vivo* were tested by s.c. implanting gelfoam sponges saturated with VEGF, basis FGF, and TGF- α . To quantify vascularization, hemoglobin concentrations were compared (Fig. 7). Plugs from WT mice contained ≈ 5 -fold more hemoglobin than those from APN-null mice. These results show that APN deficiency reduces the angiogenic response and supports a role in pathological angiogenesis.

Discussion

This study reports the generation of an APN-null mouse and an evaluation of its phenotype. APN-null mice exhibit no developmental, fertility, or behavioral or physiological abnormalities. Interestingly, inactivation of APN gene expression impaired the formation of new blood vessels under pathological conditions.

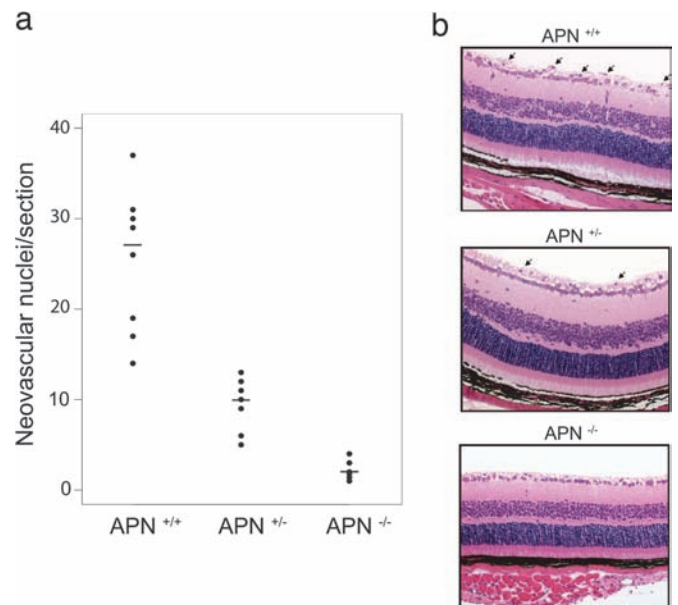


Fig. 6. Failed retinal neovascularization in APN-null mice under hypoxic conditions. (*a*) Quantification of endothelial cells nuclei extended across the inner surface of the retina into the vitreous space. Data from WT, APN-heterozygous, and APN-null mice were compared ($P < 0.001$). (*b*) APN-null mice lack the nuclei protruding into the vitreous space of the eye, as observed in the WT and heterozygote representative examples (arrows). Five independent experiments were performed with similar results.

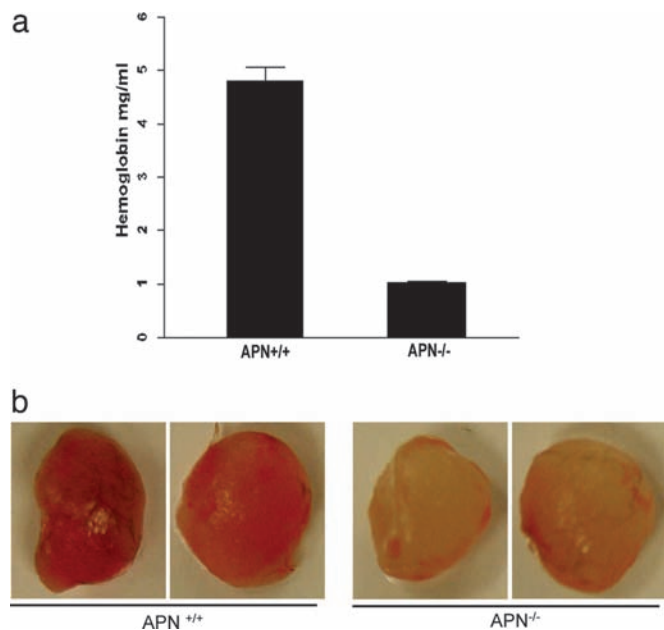


Fig. 7. APN-null mice have severely impaired angiogenesis upon growth factor stimulation. (a) Hemoglobin content of the gelfoam from WT and APN-null mice were analyzed. (b) Gelfoam plugs implanted in the s.c. tissue were removed after 14 days and analyzed. Plugs in WT mice contained significantly more hemoglobin (4.8 ± 0.3 mg/ml) than those in APN^{-/-} mice (1.0 ± 0.1 mg/ml; $P < 0.0001$). Five independent experiments were performed with similar results.

The genetic results presented here not only expand the knowledge of APN in angiogenesis but also provide a tool to study APN function in other fields.

Angiogenesis is critical to pathological conditions, including cancer, inflammation, and retinopathies (21, 24, 25). The present study shows that APN-null mice display a severely impaired angiogenic response to oxygen-induced retinopathy and respond far less strongly to angiogenic growth factors *in vivo* than do WT animals. These data are consistent with our original biochemical observation regarding a functional role for APN in angiogenesis, where the administration of blocking antibodies or chemical inhibitors of APN suppressed new blood vessel formation in several mouse models (21). Shapiro and colleagues later showed that APN is transcriptionally activated by angiogenic signals, mediated by the renin-ang system /MAPK/Ets-2 signaling pathway, and essential for endothelial morphogenesis and capillary tube formation (26–28). Recently, by using RNA interference, Fukasawa *et al.* (29) confirmed that APN is selectively expressed in vascular endothelial cells, and that the enzyme plays multiple roles in angiogenesis. These results (21, 26–29) are in agreement with our findings in the APN-null mouse. However, future experiments are required to determine the precise downstream mechanism(s) through which APN regulates neovascularization. Indeed, APN-null mice develop normally despite strong gene expression during embryogenesis. These contrasting observations indicate that APN is not an essential enzyme for vasculogenesis during development and suggest genetic redundancy or compensation. Of note, similar angiogenic defects were observed in the APA-null mouse, suggesting that both aminopeptidases are required for new blood vessel formation (30). Furthermore, APA and APN serially cleave molecules of the renin-ang system: APA cleaves ang II into ang III, and APN cleaves ang III into ang IV (31). It is tempting to speculate that ang IV is an angiogenic molecule; thus, an enzymatic deficiency (in APN or APA) could ultimately limit the generation of ang

IV and be one possible mechanism leading to reduced angiogenesis in APN-null mice. It is also plausible that other substrate(s) might exist. Interestingly, in pilot experiments, wound-healing assays showed no significant differences between WT and APN-null mice (unpublished results); these results, along with the observed normal fertility and litter sizes suggest that physiological angiogenesis is not affected in APN-null mice. The phenotype in the double (APN/APA)-null mouse remains to be determined; these experiments are ongoing.

Remarkably, APN-null mice have no apparent alterations in blood pressure or electrolytes. These findings are somewhat unexpected, because increased levels of ang III alter water balance and blood pressure (31–33). One possible reason why hemodynamics and electrolyte homeostasis remain normal with no APN activity may be that a mouse homologue of the human adipocyte-derived leucine aminopeptidase (A-LAP) can directly cleaves ang II to produce ang IV (34). The expression of mouse A-LAP is yet to be measured, but it could conceivably compensate for decreased production of ang IV in APN-null mice.

Several reports have demonstrated that enkephalins are neuropeptides cleaved by APN (35–37). Enkephalins are predominantly detected in the thalamus and spinal cord and regulate pain perception, memory, and satiety (38, 39). Experimental manipulation of the brain renin-ang system has shown that exogenous administration of high doses of ang III can modify thirst and sodium appetite, and that doses of ang IV can alter learning and memory (40, 41). Recently, proteomic analysis revealed that APN hydrolyzed leucine and methionine enkephalins in exosomes of microglial cells (42). In line with these studies, a subtle trend toward reduction of water and food consumption was noted in APN-null mice. Although modest, these data suggest that the catabolism of enkephalins might be slightly altered in the APN-null mouse, but that redundancy or compensatory mechanisms are present. Moreover, the APN-null mouse has a small but significantly increased tolerance to heat and pain stimuli. These data again support the enzymatic role of APN in inactivation of enkephalin, leading to pain resistance. However, more refined neurological experiments are needed to better define these minor phenotypes.

Additional insights into APN function may be gained by considering its role as a cell surface receptor for human coronaviruses (11, 12). The SARS virus is a coronavirus that produces severe respiratory infection in patients (43). The mechanism of SARS virus internalization is through binding to the host receptors ACE-2 and L-SIGN (CLEC4M/CD209) in lung epithelial cells (44, 45); we (13) and other investigators (44, 45) have speculated that APN may be a coreceptor for the SARS virus. Because APN is expressed in the lung epithelium, it is worthwhile to evaluate the APN-null mouse as an experimental model for SARS or other coronavirus-induced human diseases.

In summary, we generate and describe the phenotype of an APN-null mouse. Despite the broad range of APN functions, APN-null mice develop and function normally. However, our results provide a clear role for APN in angiogenesis under pathological conditions and provide a genetic model to explore further the role of this enzyme in other biological processes.

Materials and Methods

Generation of Knockout Mice. Commercially available BAC mouse 129S6/SvEv Tac genomic libraries (Research Genetics, Huntsville, AL) were screened by using a ³²P-labeled APN cDNA probe. Filters were hybridized at 60°C, washed, and exposed for 4 h at –80°C on x-ray films. Bioinformatics and Southern blot analysis were used to characterize the *Anpep* gene and generate a restriction map for the gene targeting strategy. The 5' and 3' arms of homology of the targeting vector (4.5- and 5.5-kb, respectively) were obtained by PCR (Expand Long PCR template kit; Roche, Indianapolis, IN) and confirmed by DNA

sequencing. A diphtheria toxin gene driven by the pMC1 promoter was cloned at the 3' end of the construct for negative selection. The targeting vector was linearized by NotI and electroporated into mouse ES cells. DNA from neomycin-resistant ES cell colonies was digested by EcoRI (Roche), separated by agarose gel electrophoresis, blotted onto nylon membranes, and hybridized with a 250-bp external probe. Homologous recombination events were identified by Southern blot (11-kb, WT allele; 8-kb, mutant allele). Targeted ES cell clones were injected into the blastocyst of C57BL/6 mice, and a single chimeric mouse was intercrossed with C57BL/6 mice to establish a germ-line transmission. This study adhered to the ARVO Statement for the Use of Animals in Ophthalmology and Vision Research. The Institutional Animal Care and Use Committee of the University of Texas M. D. Anderson Cancer Center Animal approved all experimentation.

Genotyping. Genotyping was performed by Southern blot and PCR with three primer combinations: forward, 5'-CAC-CCCCATCCCCATCCCTTAC-3'; reverse, 5'-GTGC-CCACGCCCTTGAACCTTACTT-3'; and IRES-rev, 5'-ACAAACGCACACCGCCTTATTCC-3'. PCR with the forward/reverse and forward/IRES-rev primer pairs generated an 879-bp WT product and a 320-bp mutant product. For PCR-based genotyping, a hot-start (Qiagen, Valencia, CA) initial step of denaturation (95°C for 15 min) was then followed by 35 cycles (denaturation, 94°C for 30 s; annealing, 65°C for 1 min; extension at 68°C for 1 min).

RT-PCR. Mice were killed by cervical dislocation and tissues removed and incubated in TRIzol reagent (Invitrogen, Carlsbad CA) for total RNA isolation. cDNA was obtained with the reverse transcriptase (RT) SuperScript III kit (Invitrogen). To detect the expression of the APN transcript, we used the PCR primers: forward 5'-CCCCGGGGCTGCTGTTCTTT-3' and reverse 5'-ACCACCCGCTCCTTGTTGCTAATG-3'. PCR amplification consisted of an initial step (94°C for 3 min) followed by 35 cycles (94°C for 30 s, 65°C for 1 min, 72°C for 1 min). The housekeeping gene glycerol-3-phosphate dehydrogenase (G3PDH) served as an internal loading control.

Histopathology. Three- and 6-mo-old WT and APN-null male and female mice (at least three mice on each group) were used for histopathological analysis. Blood samples were collected for hematology and serum chemistry studies from each mouse.

Tissue Processing and Immunohistochemistry. WT (APN^{+/+}), heterozygous (APN^{+/-}), and null (APN^{-/-}) mice were anesthetized with Avertin and perfused with 4% paraformaldehyde in PBS (pH 7.4). Organs were removed, incubated in the same fixative solution for 1 h, and then infiltrated with 30% sucrose in PBS containing 0.002% sodium azide overnight at 4°C. The next day, the organs were frozen in OCT and stored at -80°C. Frozen

tissue sections were cut, air-dried on slides, rinsed twice for 5 min with PBS and once with PBS containing 1% Triton X-100 (PBST), and then blocked with 5% normal goat serum (Jackson ImmunoResearch, West Grove, PA) in PBST for 30 min. Tissue sections were incubated for 1 h in primary antibody solution containing monoclonal Armenian hamster anti-CD31 (1:500 dilution, clone 2H8; Chemicon, Temecula, CA), monoclonal rat anti-CD13 (1:500 dilution, clone R3-63; Serotec, Raleigh, NC), and 1% normal goat serum in PBST. Slides were then rinsed three times with PBST for 5 min each and incubated for 30 min with a 0.45- μ m-filtered secondary antibody solution containing FITC-conjugated goat anti-hamster IgG (1:200; Jackson ImmunoResearch) and Cy3-conjugated goat anti-rat IgG (1:400; Jackson ImmunoResearch) in PBST. Finally, slides were rinsed three times for 5 min each with PBST, fixed with 4% PFA in PBS for 1 min, rinsed three times with PBS for 5 min each, and mounted (Vectashield; Vector Laboratories, Burlingame, CA).

Noninvasive Phenotypic Analysis. Age- and sex-matched WT, heterozygous, and null ($n = 6$ /group) were evaluated for fertility, litter size, locomotor activity, nociception, grip strength, blood pressure, in-cage comprehensive monitoring system, dual energy x-ray absorptiometry, and electrocardiogram.

Retinal Neovascularization Assay. Mice were exposed to 75% oxygen (P7-P12) and killed (P19). Eyes were enucleated and fixed in Bouin's solution. Tail snips were taken to determine the genotype. Fixed and alcohol-dehydrated eyes were embedded in paraffin, serially sectioned and H&E-stained. Endothelial cell nuclei on the vitreous side of the internal limiting membrane were counted.

In Vivo Angiogenesis Assay. To induce the formation of new blood vessels *in vivo*, gelfoam sponges (Johnson & Johnson, Somerville, NJ) were saturated with growth factors (200 ng/ml each; R&D Systems, Minneapolis, MN) including VEGF, basic FGF, and TGF- α . Sponges were implanted s.c. After 14 days, mice were killed, and gelfoams were homogenized and incubated with Drabkin's reagent (Sigma, St. Louis, MO). Hemoglobin content was reported as mean \pm SEM. WT, heterozygous, and null mice were compared.

Statistical Analysis. An ANOVA test of variance served to determine significant differences among multiple groups. Paired *t* test comparisons were used for applied posthoc analysis and adjusted by Bonferroni correction.

We thank Drs. Jan Parker-Thornburg, Amin Hajitou, Siew-Sim Cheah, and Glauco R. Souza for discussions and technical assistance. R.R. is a Scholar from the Odyssey Program at the University of Texas M.D. Anderson Cancer Center. This work was supported by grants from the National Institutes of Health and the Department of Defense and by an award from the Gillson-Longenbaugh Foundation (to W.A. and R.P.).

- Hooper NM, Lendeckel U, eds (2004) *Aminopeptidases in Biology and Disease* (Kluwer Academic/Plenum, New York).
- Barrett AJ, Rawlings ND, Woessner JF, eds (2004) *Handbook of Proteolytic Enzymes* (Elsevier, London).
- Amoscato AA, Alexander JW, Babcock GF (1989) *J Immunol* 142:1245-1252.
- Favaloro EJ, Bradstock KF, Kabral A, Grimsley P, Zowtyj H, Zola H (1988) *Br J Haematol* 69:163-171.
- Meckersheimer G, Moller P (1990) *Am J Pathol* 137:1215-1222.
- Menrad A, Speicher D, Wacker J, Herlyn M (1993) *Cancer Res* 53:1450-1455.
- Riemann D, Kehlen A, Langner J (1999) *Immunol Today* 20:83-88.
- Lalu K, Lampelo S, Vanha-Perttula T (1986) *Biochim Biophys Acta* 873:190-197.
- Chansel D, Czekalski S, Vandermeersch S, Ruffet E, Fournie-Zaluski MC, Ardaillou R (1998) *Am J Physiol* 275:535-542.
- Matsas R, Turner AJ, Kenny AJ (1984) *FEBS Lett* 175:124-128.
- Delmas B, Gelfi J, L'Haridon R, Sjöström H, Norén O, Laude H (1992) *Nature* 357:417-420.
- Yeager CL, Ashmun RA, Williams RK, Cardellichio CB, Shapiro LH, Look AT, Holmes KV (1992) *Nature* 357:420-422.
- Kontoyiannis DP, Pasqualini R, Arap W (2003) *The Lancet* 361:1558.
- Santos AN, Langner J, Herrmann M, Riedmann D (2000) *Cell Immunol* 201:22-32.
- Mina-Osorio P, Ortega E (2005) *J Leukocyte Biol* 77:1008-1017.
- Hajitou A, Pasqualini R, Arap W (2006) *Trends Cardiovasc Med* 16:80-88.
- Sergeeva A, Kolonin MG, Mollndrem JJ, Pasqualini R, Arap W (2006) *Adv Drug Deliv Rev* 58:1622-1654.
- Arap W, Pasqualini R, Ruoslahti E (1998) *Science* 279:377-380.
- Ellerby HM, Arap W, Ellerby LM, Kain R, Andrusiak R, Rio GD, Krajewski S, Lombardo CR, Rao R, Ruoslahti E, et al. (1999) *Nat Med* 5:1032-1038.

20. Curnis F, Sacchi A, Borgna L, Magni F, Gasparri A, Corti A (2000) *Nat Biotechnol* 18:1185–1190.
21. Pasqualini R, Koivunen E, Kain R, Lahdenranta J, Sakamoto M, Stryhn A, Ashmun RA, Shapiro LH, Arap W, Ruoslahti E (2000) *Cancer Res* 60:722–727.
22. Curnis F, Arrigoni G, Sacchi A, Fischetti L, Arap W, Pasqualini R, Corti A (2002) *Cancer Res* 62:867–874.
23. Mentzel S, Dijkman HBPM, Van Son JPHF, Koene RAP, Assmann KJM (1996) *J Histochem Cytochem* 44:445–461.
24. Folkman J (2006) *Annu Rev Med* 57:1–18.
25. Lahdenranta J, Pasqualini R, Schlingemann RO, Hagedorn M, Stallcup WB, Bucana CD, Sidman RL, Arap W (2001) *Proc Natl Acad Sci USA* 98:10368–10373.
26. Bhagwat SV, Petrovic N, Okamoto Y, Shapiro LH (2003) *Blood* 101:1818–1826.
27. Petrovic N, Bhagwat SV, Ratzan WJ, Ostrowski MC, Shapiro LH (2003) *J Biol Chem* 278:49358–49368.
28. Bhagwat SV, Lahdenranta J, Giordano R, Arap W, Pasqualini R, Shapiro LH (2001) *Blood* 97:652–659.
29. Fukasawa K, Fujii H, Saitoh Y, Koizumi K, Aozuka Y, Sekine K, Yamada M, Saiki I, Nishikawa K (2006) *Cancer Lett* 243:135–143.
30. Marchiò S, Lahdenranta J, Schlingemann RO, Valdembri D, Wesseling P, Arap MA, Hajitou A, Ozawa MG, Trepel M, Giordano RJ, et al. (2004) *Cancer Cell* 5:151–162.
31. Reaux A, Fournie-Zaluski MC, Llorens-Cortes C (2001) *Trends Endocrinol Metab* 12:157–162.
32. Faber F, Gembardt F, Sun X, Mizutani S, Siems W-E, Walter T (2006) *Regul Pept* 136:130–137.
33. Wright JW, Tamura-Myers E, Wilson WL, Roques BP, Llorens-Cortes C, Speth RC, Harding JW (2002) *Am J Physiol* 284:725–733.
34. Goto Y, Hattori A, Ishii Y, Tsujimoto M (2006) *FEBS Lett* 580:1833–1838.
35. Gros C, Giros B, Schwartz JC (1985) *Biochemistry* 24:2179–2185.
36. Churchill L, Bausback HH, Gerritsen ME, Ward PE (1987) *Biochim Biophys Acta* 923:35–41.
37. Giros B, Gros C, Solhonne B, Schwartz JC (1986) *Mol Pharmacol* 29:281–287.
38. Holden JE, Jeong Y, Forrest JM (2005) *AACN Clin Issues* 16:291–301.
39. Lullmann H, Mohr K, Ziegler A, Bieger D (1993) *Color Atlas of Pharmacology* (Thieme, Stuttgart, Germany).
40. Wilson WL, Roques BP, Llorens-Cortes C, Speth RC, Harding JW, Wright JW (2005) *Brain Res* 1060:108–117.
41. Albiston AL, McDowall SG, Matsacos D, Sim P, Clune E, Mustafa T, Lee J, Mendelsohn FAO, Simpson RJ, Connolly LM, Chai SY (2001) *J Biol Chem* 276:48623–48626.
42. Potoicchio I, Carven GJ, Xu X, Stipp C, Riese RJ, Stern LJ, Santambrogio L (2005) *J Immunol* 175:2237–2243.
43. Yeung KS, Yamanaka GA, Meanwell NA (2006) *Med Res Rev* 26:414–433.
44. Li W, Moore MJ, Vasilieva N, Sui J, Wong SK, Berne MA, Somasundaran M, Sullivan JL, Luzuriaga K, Greenough TC, et al. (2003) *Nature* 426:450–454.
45. Chan VSF, Chan KYK, Chen Y, Poon LLM, Cheung ANY, Zheng B, Chan K-H, Mak W, Ngan HYS, Xu X, et al. (2006) *Nat Gen* 38:38–46.